Czech Technical University
in Prague

Faculty of Nuclear Sciences and Physical
Engineering

DISSERTATION

Connection between Arrival Directions and
Mass of Ultra-high-energy Cosmic Rays

Prague 2024

Ing. Alena Bakalová

Bibliografický záznam

Autor:	Ing. Alena Bakalová, České vysoké učení technické v Praze, Fakulta jaderná a fyzikálně inženýrská, Katedra fyziky
Název práce:	Souvislosti mezi příchozími směry a hmotnostním složením kosmického záření ultra-vysokých energií
Studijní program:	Aplikace přírodních věd
Studijní obor:	Jaderné inženýrství
Školitel:	Ing. Jakub Vícha, Ph.D., Fyzikální ústav Akademie věd České republiky
Školitel specialista:	RNDr. Petr Trávníček, Ph.D., Fyzikální ústav Akademie věd České republiky
Akademický rok:	2023/2024
Počet stran:	149
Klíčová slova:	Kosmické záření ultra-vysokých energií, Galaktické magnetické pole, příchozí směry, hmotnostní složení

Bibliographic Entry

Author:	Ing. Alena Bakalová, Czech Technical University in Prague, Faculty of Nuclear Sciences and Physical Engineering, Department of Physics
Title of Dissertation:	Connection between Arrival Directions and Mass of Ultra-high-energy Cosmic Rays
Degree Programme:	Applications of Natural Sciences
Field of Study:	Nuclear Engineering
Supervisor:	Ing. Jakub Vícha, Ph.D., Institute of Physics of the Czech Academy of Sciences
Supervisor Specialist:	RNDr. Petr Trávníček, Ph.D., Institute of Physics of the Czech Academy of Sciences
Academic Year:	2023/2024
Number of Pages:	149
Keywords:	Ultra-high-energy cosmic rays, Galactic magnetic field, arrival directions, mass composition

Abstrakt

Kosmické záření ultra-vysokých energií (UHECR) jsou nabité částice přicházející z vesmíru s energiemi nad 10^{18} eV. Tyto částice během interakcí s atmosférickými jádry vytvářejí rozsáhlé spršky sekundárních částic, jež mohou být detekovány pomocí pozemních experimentů a jejichž zkoumáním můžeme lépe porozumět vlastnostem těchto extrémně energetických částic. Nejnovější měření prokazují extragalaktický původ nejenergetičtějších částic UHECR, avšak typ astrofyzikálních objektů a procesů, které je mohou vytvářet, zůstává neznámý. Trajektorie UHECR jsou ovlivňovány galaktickými i extragalaktickými magnetickými poli a jejich energie a hmotnostní složení se může během šíření ve vesmíru měnit díky interakcím s okolním prostředím. Abychom tedy skutečně porozuměli původu těchto částic, je třeba vzít tyto efekty šíření v úvahu. Tato práce prezentuje čtyři témata, na kterých jsem pracovala během svého doktorského studia.

První téma prezentované v této práci navazuje na pozorování dipólové anizotropie v příchozích směrech kosmického záření nad 8 EeV Observatoří Pierra Augera. Ve své práci zkoumám vliv galaktického magnetického pole na tuto dipólovou anizotropii, přičemž jsou brány v úvahu různé scénáře hmotnostního složení. S použitím dvou modelů galaktického magnetického pole jsou identifikovány možné extragalaktické směry dipólové anizotropie na okraji naší galaxie. Výsledky ukazují, že v rámci porovnání na úrovni 1σ pro případ lehkého složení (protony a jádra helia) může být extragalaktický směr dipólu vzdálený do $\sim 45^\circ$ od směru dipólu pozorovaného na Zemi, zatímco v případě těžšího složení může být extragalaktický směr dipólu vzdálený až $\sim 105^\circ$ od jeho směru na Zemi.

Energetické spektrum kosmického záření nad $10^{19,5}$ eV měřené Observatoří Pierra Augera na jižní polokouli a Telescope Array na severní polokouli vykazuje nesrovnalosti. Druhé téma této práce se zabývá možností, že částice detekované Observatoří Pierra Augera nad $10^{19,5}$ eV pochází dominantně z jediného zdroje. Možné vlastnosti takového zdroje jsou prezentovány rovněž s dodatečnými omezeními na hmotnostní složení kosmického záření nad $10^{19,5}$ eV na Zemi. Analýza ukazuje, že pro přesný popis tvaru energetického spektra a hmotnostního složení pozorovaného na Zemi se musí navrhovaný zdroj nacházet ve vzdálenosti do ~ 20 Mpc od Země, mít spektrální index $\gamma \sim 3$ a hodnotu rigidity, energie produkovaných částic podělené jejich nábojem, nižší nebo rovnou $10^{19,2}$ V.

Další téma se zabývá Monte Carlo simulacemi odezvy vodních Čerenkovových detektorů pro plánovanou gama observatoř Southern Wide-field Gamma-ray Observatory (SWGO). Předložená práce ukazuje srovnání dvou simulačních softwarů a potvrzuje vhodnost simulačního programu používaného v rámci SWGO kolaborace pro její účely. Současně je zde představena studie zabývající se simulacemi odezvy navrhované malé stanice vodního Čerenkovova detektoru. Poslední představené téma se věnuje mému příspěvku k analytickému aproximativnímu popisu zesílení fotonové intezity zdrojů v okolí kompaktních objektů.

Abstract

Ultra-high-energy cosmic rays (UHECRs), charged particles coming from space with energies above 10^{18} eV, generate extensive air showers of secondary particles when they interact with the atmospheric nuclei. These showers, detectable by ground-based experiments, provide insights into the properties of these extremely energetic particles. Recent measurements prove an extragalactic origin of the most energetic UHECRs. However, the type of astrophysical objects and processes that can produce them remain unknown. The trajectories of UHECRs are influenced by both Galactic and extragalactic magnetic fields and their energy and mass composition can be modified during propagation due to interactions with the environment in the universe. Therefore, to fully understand the origin of these particles, these propagation effects must be taken into account. This thesis presents four topics that I have been working on during my doctoral studies.

The first topic presented in this thesis is following up on an observation of a large-scale dipole anisotropy in arrival directions of cosmic rays above 8 EeV by the Pierre Auger Observatory. My work explores the effects of the Galactic magnetic field on this dipole anisotropy, taking into account various mass-composition scenarios. The allowed extragalactic directions of the dipole anisotropy before the cosmic rays enter our Galaxy are presented for two models of the Galactic magnetic field. The results indicate that, at the 1σ level comparison, for light mass composition (proton and helium nuclei), the extragalactic direction of the dipole should be located within $\sim 45^\circ$ from the measured direction of the dipole on Earth, while for heavier composition the extragalactic direction of the dipole might be located as far as $\sim 105^\circ$ from the measured direction on Earth.

The energy spectra of cosmic rays above $10^{19.5}$ eV measured by the Pierre Auger Observatory (Southern hemisphere) and by the Telescope Array (Northern hemisphere) exhibit discrepancies. The second topic of this thesis delves into the possibility of a single source of UHECRs contributing to the energy spectrum above $10^{19.5}$ eV seen by the Pierre Auger Observatory and explores the possible properties of such a source. The limitations on the properties of this source are presented also with additional constraints on the mass composition of cosmic rays above $10^{19.5}$ eV on Earth. The analysis reveals that for an accurate description of the shape of the energy spectrum and the mass composition on Earth, a possible single source must be within ~ 20 Mpc from Earth, have a spectral index $\gamma \sim 3$, and a rigidity (energy of particles divided by their charge) lower or equal to $10^{19.2}$ V.

Another topic addresses the simulations of the responses of water Cherenkov detectors for the planned Southern Wide-field Gamma-ray Observatory (SWGO). The presented work shows the comparison of two simulation softwares and confirms the suitability of the simulation framework used within the SWGO collaboration for its purposes. Moreover, a study of the performance of a proposed small water Cherenkov detector station is presented. Additionally, research concerning the analytical approximate description of the amplification of the photon intensity of sources around compact objects is introduced.

Acknowledgements

I would like to express my deepest gratitude to my supervisor, Jakub Vícha, for his kind mentorship, insightful ideas, patience and support. Without his invaluable guidance the realisation of this thesis would not be possible. I would also like to thank my supervisor specialist, Petr Trávníček, whose contributions have been instrumental in shaping the content of this work.

I am also grateful to all the colleagues from the Department of Astroparticle Physics at the Institute of Physics of the Czech Academy of Sciences. The pleasant and enriching working environment and professional discussions made tackling physics tasks and challenges more accessible with their collaborative support.

Lastly, but certainly not least, I would like to express thanks to my father, Pavel Bakala, who introduced me to the field of physics and helped to ignite the passion to study the unknown. His influence has been a source of inspiration and motivation, shaping my academic pursuit from the very beginnings.

Declaration

I hereby declare that this thesis is the result of my own work and all the sources I used (literature, projects, software, etc.) are in the list of references. I have no objection against the use of this work in compliance with the act §60 Law No. 121/2000 Coll. (Copyright Act), and with the rights connected with the copyright act including the changes in the act.

In Prague, 15. 2. 2024 Ing. Alena Bakalová

Contents

Introduction

Studying the celestial objects and the universe is inherent to human nature. Historically, the observations were limited to the visible light spectrum. However, with the advancement of knowledge and technology, scientists have developed new observational methods, expanding beyond the visible spectrum and even beyond the electromagnetic spectrum. At the lowest photon energies, the cosmic microwave background shows us the early stages of the evolution of the universe, while photons at the highest energies, gamma rays, are messengers from powerful astrophysical objects together with astrophysical neutrinos that also aid in deciphering nuclear processes in stars. Gravitational waves provide insights into the dynamics of massive astrophysical systems. Last but not least, cosmic rays, charged particles bombarding Earth at wide range of energies, are another messengers from the universe carrying essential information about the physics happening in distant astrophysical sources. Despite the discovery of ultra-high-energy cosmic rays (UHECRs, above 10^{18} eV) more than 60 years ago, the origin and mechanisms of their acceleration still remain a mystery. However, their enormous energies make them intriguing subjects of study, potentially unveiling the physics behind the most violent processes in the universe.

During the doctoral studies, I mostly focused on studying the UHECRs and their propagation in the universe. Two research topics concerning UHECRs are presented in this thesis. The first topic deals with the modifications of the dipole anisotropy in arrival direction of cosmic rays above 8 EeV due to the Galactic magnetic field. Simulations of cosmic-ray propagation in two models of the Galactic magnetic field were performed for multiple particle species to identify the allowed extragalactic directions of the dipole before entering the Milky Way. The second topic that has been studied is the possibility of describing the energy spectrum of cosmic rays above $10^{19.5}$ eV as measured by the Pierre Auger Observatory by a single source. The properties of such a source allowing a good description of the energy spectrum and mass composition of cosmic rays above $10^{19.5}$ eV were searched for.

Part of my research during the doctoral studies was also devoted to high-energy gamma rays. In this thesis, the analysis work for the planned Southern Wide-field Gamma-ray Observatory (SWGO) experiment is presented, focusing on the simulations of the responses of water Cherenkov detector stations to the secondary particles originating from the gamma-ray induced extensive air showers. This, rather technical work, is supplementing the other two phenomenological topics concerning UHECRs. Additionally, I also participated in a research concerning the amplification of the photon intensity of sources in binary systems

with a compact object, suggesting new analytical approximate formulae that can describe the amplification in the extreme regime of the lensing and the time delay between the first two images.

The thesis is divided into eight chapters. Chapter 1 presents a historical overview of cosmic-ray discoveries and the description of extensive air showers. The Pierre Auger Observatory, the largest currently operating experiment detecting cosmic rays of ultra-high energies, is introduced in Chapter 2 together with the reconstruction techniques of cosmic-ray showers. The propagation of cosmic rays in the universe is described in Chapter 3. The chapter describes the energy losses of particles, including interactions with ambient photon backgrounds, and the deflections of cosmic rays in magnetic fields in the universe. Chapter 4 summarises the up-to-day knowledge about the energy spectrum, mass composition and arrival directions of UHECRs. The remaining chapters contain results of my research. In Chapter 5, the study of the modifications of the dipole anisotropy in arrival direction of cosmic rays due to the Galactic magnetic field is described. A possible single-source scenario and the features of such a source describing the energy spectrum ans mass composition of cosmic rays at the highest energies are presented in Chapter 6. Chapter 7 is devoted to high-energy gamma rays. A future SWGO experiment is introduced together with simulations of responses of water Cherenkov detector stations needed during the R&D phase of SWGO. The amplification of photon intensity of sources in binary systems with compact objects is also described in this chapter. Finally, Chapter 8 encapsulates the key findings and conclusions of the presented results.

Chapter 1

Cosmic rays

Cosmic rays are high-energy charged particles coming to the Earth's atmosphere from outer space that are arriving from all directions almost isotropically. Physicists have been studying cosmic rays since the beginning of the 20^{th} century. From the start, cosmic rays were known to be of energies up to 10 GeV [1]. However, over half a century, the most energetic particles known were of energies up to 10^{20} eV and beyond. Such high energies are still very far from energies we are able to achieve in man-made accelerators on Earth and, consequently, these particles are of great scientific interest.

At lower energies, the cosmic rays originate in the Sun. At higher energies, the origin and rate of cosmic rays can be explained by supernovae remnants and other Galactic sources. However, it is believed that cosmic rays of ultra-high energies (above 10^{18} eV) are of extragalactic origin, which is supported by measurements of the dipole anisotropy in arrival directions of cosmic rays above 8 EeV [2]. Yet, after more than 60 years after their discovery, their sources and the mechanisms of their acceleration are still unknown.

This chapter provides a brief introduction to the topic of cosmic rays. A short historical overview of the early cosmic-ray discoveries is introduced in Section 1.1. A description of the extensive air showers is presented in Section 1.2 together with the modeling of the shower development with emphasis on the important parameters of the shower that are used for reconstruction of the energy and mass of the primary particle.

1.1 Brief historical overview

By the end of the 19^{th} century, scientists had been noticing a spontaneous discharging of electroscopes[1]. At that time, this phenomenon was difficult to explain other than by conduction of air via dust particles [3]. However, with the discovery of radioactivity in 1896, it was soon realised that some form of natural radiation is causing ionisation of air

[1] An electroscope is a scientific instrument, now rather historical, that is capable of detecting the presence of an electric charge. The electroscope can consist, for example, of thin gold leaves suspended from an electrical conductor into an isolated volume. When a charge is brought to the conductor, the leaves are repelled by an electrostatic force.

which can subsequently lead to the discharges. Originally, the scientific consensus was that this radiation is of a terrestrial origin.

In order to prove this hypothesis, multiple experiments were performed in the early 20^{th} century. In 1910, one of such experiments was led by Theodor Wulf who measured the ionisation of air on the top of the Eiffel tower, approximately 300 m above the ground [4]. However, his measurements were inconclusive. Although he observed a decrease of the radiation, the decrease was not as strong as expected. Based on his calculations, the ionisation caused by gamma rays from Earth should decrease to only a few percent with respect to the ionisation measured on the ground [3].

The terrestrial origin of the ionisation of air was questioned by an Italian scientist, Domenico Pacini, who performed a series of experiments between 1907 and 1912. He was measuring air conductivity on the ground, on the ocean (and on the lake), and deep under the ocean [3]. His measurements showed that the air ionisation on the ocean, 800 m from the coast, was at the similar level as on the mainland. He continued by measurements of radiation intensity under the water and proved that the radiation was absorbed by the water. Based on these observations, Pacini concluded that the ionisation of air can not be explained only by known sources of radiation in the Earth's crust and, therefore, other sources of radiation must exist. He also speculated about radiation of an extraterrestrial origin [5].

The discovery of cosmic rays is acknowledged to Austrian physicist Victor Franz Hess, who performed multiple hydrogen balloon ascents between 1911 and 1912. He measured the ionisation of air at different altitudes above the ground, going as high as 5000 m a.s.l. His findings suggested that after an initial drop, the ionisation of air strongly increases above $\sim$ 1400 m a.s.l. [4]. At altitude $\sim$ 2000 m, the measured ionisation was at the same level as at the ground [3]. Hess deduced that radiation of great penetrating power is entering the atmosphere from above [6]. Furthermore, one of Hess's ascents took place during an almost total solar eclipse. No significant decrease of the radiation was found in his measurements during the eclipse. Based on these findings he concluded that the Sun is not the source of this radiation and that its origin is farther out in space. Hess was awarded the Nobel prize in physics in 1936 for his discovery of cosmic radiation.

With the development of new detection techniques in the first half of the 20^{th} century, the nature of cosmic rays was becoming more and more clear. In 1928, Bothe and Kolhörster applied the coincidence technique to cosmic-ray detection. Their observations suggested that cosmic rays are charged particles, disproving the common belief of that time that cosmic rays are gamma rays. To further support this hypothesis, they placed 4 cm thick gold block between two coincidence detectors and observed that the coincidence rate decreased by only 24% [3]. In 1933, observations of Rossi showed that 50% of cosmic rays can penetrate one meter of lead, which gives an energy of the particle of $\sim 1.4 \cdot 10^{10}$ eV [1]. Such observation supported the previous conclusions of Bothe and Kolhörster about the corpuscular nature of cosmic rays. Rossi also observed a steep increase of triple coincidences in a triangular arrangement of Geiger counters when lead shielding was placed on top. From such observations, Rossi concluded that soft secondary particles were produced by cosmic particles within the material [1].

It was soon realised by many scientists, including Rossi, Bothe, Kolhörster and Schmeiser, that a similar process of particle cascades in the material must be taking place in the atmosphere as well and that the primary cosmic ray hitting the Earth's atmosphere is also creating a shower of secondary particles. The discovery of extensive air showers is attributed to French physicist Pierre Victor Auger. In 1937, Auger with his colleagues performed experiments in Swiss Alps, where they confirmed the existence of extensive air showers [1]. Furthermore, Auger's findings led to the conclusion that the energy of the primary particle initiating these observed showers must be at least 10^{15} eV [7].

The discovery of extensive air showers triggered a new era of cosmic-ray experiments. Soon, large-area observatories were built to explore the properties of cosmic rays between energies $10^{15} - 10^{17}$ eV. The first experiment covering an area of $1\,\mathrm{km}^2$ that was able to measure the energy spectrum of cosmic rays above 10^{18} eV was built in Volcano Ranch, New Mexico, led by John Linsley [3]. In 1962, they detected a cosmic-ray shower that had to be initiated by a cosmic ray with an energy about 10^{20} eV [8]. Currently, the two largest observatories detecting cosmic rays of ultra-high energies are located in the Southern hemisphere, the Pierre Auger Observatory covering an area of $3000\,\mathrm{km}^2$ [9], and in the Northern hemisphere, Telescope Array covering an area of $700\,\mathrm{km}^2$, undergoing an extension to an area of $2800\,\mathrm{km}^2$ [10].

1.2 Extensive air showers

Ultra-high-energy cosmic rays entering the Earth's atmosphere interact with atoms in the air and create a shower of secondary particles, an extensive air shower (EAS). The shower develops along the direction of the primary-particle momentum, shower axis, and the shower can contain billions of secondary particles on the ground level. During the shower evolution, the number of particles increases at first, until a maximum is reached. Afterwards the particles are attenuated as more and more particles have energy below the threshold for further multiplicative interactions.

The point of the first interaction depends on the inelastic cross-section of the primary particle with the target nucleus in the air and is, therefore, a fluctuating variable. Most of the secondary particles created in the first interaction are pions, although other particles such as kaons, hyperons, and so forth, can be created as well. These secondary particles either interact or decay.

The shower can be divided into multiple components. **The electromagnetic component** is composed of electrons, positrons and photons. At the developing stage of the shower, the photons are mostly created in decays of neutral pions, that can be produced in the interactions or in kaon decays. Neutral pions have a very short life time ($\sim 10^{-16}$ s) and therefore they almost immediately decay into two photons

$$\pi^0 \to \gamma + \gamma. \tag{1.1}$$

If the photons have sufficient energy, an electron-positron pair can be created in the presence of electromagnetic field, mainly around a nucleus with an atomic number Z

$$(Z+)\gamma \rightarrow (Z+)e^+ + e^-. \tag{1.2}$$

These electrons and positrons can create further photons via bremsstrahlung

$$(Z+)e^\pm \rightarrow (Z+)e^\pm + \gamma. \tag{1.3}$$

In this way, the electromagnetic component of the shower is produced. The electromagnetic component contains $\sim 90\%$ of all particles of the shower at the ground level.

The muonic component of the shower is created in the decays of pions and other mesons. Charged pions decay into a muon and muon neutrino as

$$\pi^- \rightarrow \mu^- + \overline{\nu_\mu}, \tag{1.4}$$

$$\pi^+ \rightarrow \mu^+ + \nu_\mu. \tag{1.5}$$

Muons can penetrate deep into the atmosphere, even down to the ground level. The muonic component constitutes approximately 10% of the overall particles of the EAS on the ground. Muons that decay before reaching the ground contribute to the electromagnetic part of the shower

$$\mu^\pm \rightarrow e^\pm + \overset{(-)}{\nu}_e + \overset{(-)}{\nu}_\mu \,. \tag{1.6}$$

The hadronic component of the shower consists of hadronic products of hadronic interactions during the shower development including protons, kaons, pions and other hadrons. It gives rise to the other components of the shower via particle interactions. At the ground level, the hadronic component is the smallest part of the shower. Portion of the energy of the primary particle is also carried away by neutrinos as a part of the so called invisible energy. The other part includes muons that did not deposit all their energy in the atmosphere.

To reconstruct the properties of the primary particle from the information provided by the detected secondary particles, the physics of the shower development needs to be studied in more detail. The main properties of the air showers can be obtained by simplified models of the shower development [11, 12]. However, to describe the shower more realistically and introduce shower-to-shower fluctuations, a complex models of the cosmic-ray shower development and Monte Carlo simulations need to be used. Interestingly, even though there is a diverse range of primary particles and their initial conditions, the evolution of the extensive air showers of cosmic rays above $\sim 10^{19}$ eV, is very universal [13]. This behaviour of the showers, called the *shower universality*, is a powerful tool that helps to describe the symmetry of extensive air showers including the energy spectra of secondary particles and their lateral and longitudinal distributions. For more details about the shower universality see [13–16].

1.2.1 Simplified models of air shower development

To describe the evolution of an air shower, it is convenient to use an *atmospheric depth* X instead of the height in the atmosphere h. The atmospheric depth is expressed in units of $\mathrm{g\,cm^{-2}}$ and is defined as

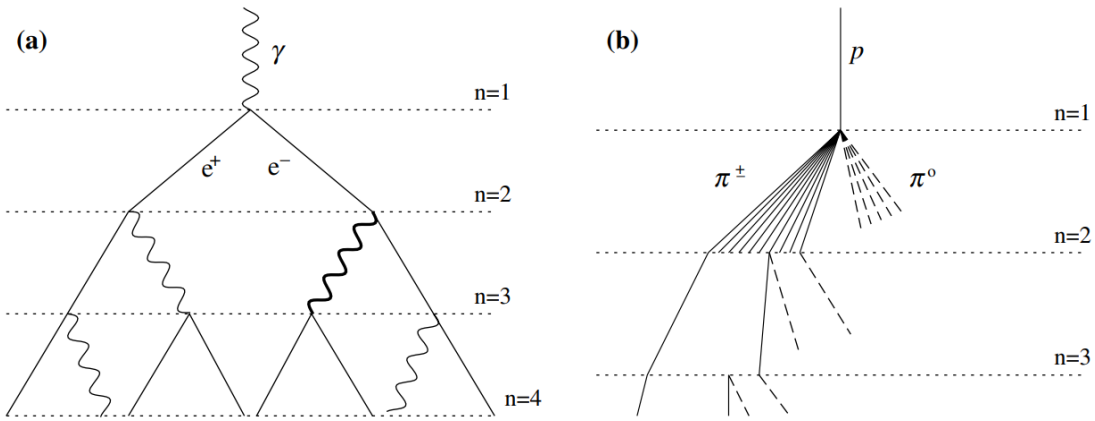

Figure 1.1: Illustration of the evolution of an electromagnetic shower under the Heitler model (left) and the evolution of a hadronic shower based on the Heitler–Matthews model (right). Taken from [12].

$$X = \int_h^\infty \rho_{\text{air}}(h)\, dh, \tag{1.7}$$

where $\rho_{\text{air}}(h)$ is the density of air at height h.

The Heitler model [11] is a simplified description of the evolution of an electromagnetic cascade. The electromagnetic cascade is initiated by a primary photon and the cascade contains only photons, electrons e^-, and positrons e^+, see the schematic of an electromagnetic cascade in the left panel of Figure 1.1. The primary and secondary photons create electron-positron pairs as in Equation (1.2). The electrons/positrons create secondary photons via bremsstrahlung as in Equation (1.3). These interactions are happening after a constant splitting length $d = \lambda_r \ln 2$, where λ_r is the radiation length in a given medium ($\sim$ 37 g cm^2 in air). After each interaction, the energy is divided equally between the two particles. The splitting process continues until the particles reach the critical energy ϵ_c, where they no longer have enough energy to undergo further interactions. Therefore, for a shower initiated by a photon with energy E_0 the maximum amount of particles in the shower is $N_{\text{max}} = E_0/\epsilon_c$. This amount of particles is reached after $n_c = \ln[E_0/\epsilon_c]/\ln 2$ splitting lengths, penetrating into a depth of

$$X^\gamma_{\text{max}} = n_c \lambda_r \ln 2 = \lambda_r \ln\left(\frac{E_0}{\epsilon_c}\right). \tag{1.8}$$

The X^γ_{max} is the depth of the shower maximum of an electromagnetic shower and it grows logarithmically with the energy of the primary particle.

The Heitler–Matthews model [12] is a simplified semi-empirical model of a hadronic shower. The evolution of a hadronic shower under Heitler–Matthews model is illustrated in the right panel of Figure 1.1. The atmosphere is divided into layers of constant thickness $d_{\text{HM}} = \lambda_I \ln 2$, where λ_I is the interaction length of strongly interacting particles. In the

first interaction, N_{ch} charged pions and $\frac{1}{2}N_{\mathrm{ch}}$ neutral pions are produced. The charged pions are carrying 2/3 of the energy of the primary particle E_0 and 1/3 of the energy is carried by the neutral pions. Neutral pions immediately decay into two photons which are triggering an evolution of an electromagnetic cascade that can be described with the Heitler model. The charged pions are travelling distance d_{HM} after which they again interact and another N_{ch} charged pions and $1/2N_{\mathrm{ch}}$ neutral pions are created. After n interactions, the energy carried in the hadronic part of the shower is equal to $E_{\mathrm{had}} = (2/3)^n E_0$ with the total number $N_\pi = (N_{\mathrm{ch}})^n$ of charged pions. The pions interact until they reach the critical energy ϵ_c^π. The critical energy is defined as the energy at which the decay length becomes less than the distance to the next interaction. The critical energy of pions in the air is $\epsilon_c^\pi \sim 20$ GeV [12]. Pions with energy equal or lower than ϵ_c^π immediately decay into muons. Therefore, the total number of muons in a proton-induced shower can be expressed as

$$N_\mu^p = N_\pi = \left(\frac{E_0}{\epsilon_c^\pi}\right)^\beta, \tag{1.9}$$

where β is a parameter than is described in the simplified model as

$$\beta = \frac{\ln N_{\mathrm{ch}}}{\ln(\frac{3}{2})N_{\mathrm{ch}}}. \tag{1.10}$$

Taking $N_{\mathrm{ch}} = 10$ then the value of β is 0.85. If the number of charged particles created in a single interaction is an order of magnitude higher, i.e. $N_{ch} = 100$, then $\beta = 0.92$.

In a similar manner as in the Heitler model, the shower maximum for the proton shower X_{max}^p can be derived as

$$X_{\mathrm{max}}^p = X_0 + \lambda_r \ln\left[\frac{E_0}{3N_{\mathrm{ch}}\epsilon_c}\right], \tag{1.11}$$

where $X_0 = \lambda_I \ln 2$ is the point of the first interaction of the proton [12]. Note that the shower maximum derived here only takes into account the electromagnetic component of the first generation.

The superposition model [12] can be used for the estimation of properties of hadronic showers initiated by nuclei heavier than proton. A nucleus with A nucleons and energy E_0 is treated as A independent protons with energies E_0/A. Each of the nucleons then creates one shower that can be described using the Heitler–Matthews model. The number of muons in a shower initiated by a nucleus with atomic number A scales as

$$N_\mu^A = N_\mu^p A^{0.15}, \tag{1.12}$$

where N_μ^p is the number of muons in a proton shower with energy of proton E_0. The shower maximum is then reached in a depth of

$$X_{\mathrm{max}}^A = X_{\mathrm{max}}^p - \lambda_r \ln A. \tag{1.13}$$

We can see, that the shower maximum for a hadronic shower initiated by nucleus with $A > 1$ is lower than the shower maximum of a shower initiated by proton of the same

energy. This shows that the depth of shower maximum $X_{\max}$ is a parameter sensitive to the mass of the primary particle. Truly, this parameter is widely used for mass-composition studies in cosmic-ray experiments.

1.2.2 Modeling of cosmic ray showers

In reality, the evolution of an air shower is a much more complex problem than the approximation approach of the Heitler or Heitler–Matthews models. These models also do not include the shower-to-shower fluctuations but instead describe the average shower development.

For more detailed studies, Monte Carlo simulation codes are used to simulate the shower development, such as CONEX [17], CORSIKA [18], or AIRES [19]. While CONEX simulations are performed in 1D and are rather fast because of employing cascade equations [20], the CORSIKA simulation software simulates the full 3D distribution of the shower and is taking quite an extensive computational time. In order to reduce the computational time and not follow every particle separately, a thinning procedure is used [21]. The simulations utilize models of high-energy hadronic interactions. Currently, the most up-to-date models are EPOS-LHC [22, 23], QGSJETII-04 [24, 25], and SIBYLL 2.3d [26, 27]. The low-energy hadronic interactions are simulated using FLUKA [28], GHEISHA [29], or UrQMD [30]. Since the properties of hadronic interactions at the centre-of-mass energy above 13 TeV and

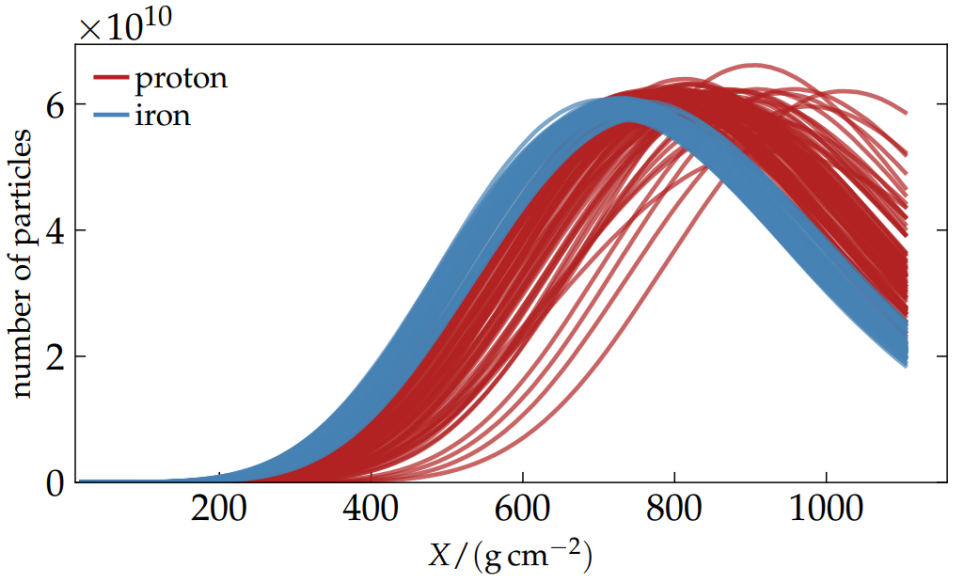

Figure 1.2: Longitudinal profiles of proton and iron nucleus air showers with primary energy 10^{19} eV and zenith angle 38° simulated in CORSIKA with EPOS-LHC model. Taken from [16].

in the forward pseudorapidity region are not available from measurements in accelerators[2], the physical parameters describing the interaction properties, such as cross-section, multiplicity or elasticity, are largely extrapolated. Although all the aforementioned high-energy hadronic models are tuned to the LHC data, they use different approaches for the theoretical description of the hadronic interactions, see [31] for a summary of the differences. Therefore, the model predictions are burdened with uncertainties and also the individual model predictions vary from model to model.

Longitudinal profiles of showers induced by protons and iron nuclei with primary energy 10^{19} eV simulated in CORSIKA are shown in Figure 1.2. It can be seen, that the shower-to-shower fluctuations are more sizable for proton-induced showers. Figure 1.2 also nicely displays that the mean shower maximum of a proton shower is deeper in the atmosphere compared to an iron-induced shower, demonstrating that the X_{max} is a mass-sensitive parameter as was already shown in the superposition model approximation in Equation (1.13).

Current cosmic-ray experiments show discrepancies between their measurements and model predictions. One of the most intriguing problems is the muon deficit in the model predictions compared to the measurements [32–34] based on the mass estimation from X_{max} measurements. Studies have shown that the muon deficit in simulations starts at energies $\sim 10^{16}$ eV and the discrepancy increases with energy [34]. At EeV energies, the increase in the muon density predicted by EPOS-LHC model is found to be $\sim 35\%$ weaker than the measured one and for QGSJet II-04 the discrepancy is more than 50% [32].

[2]Such energy approximately corresponds to a cosmic-ray proton of energy $10^{16.9}$ eV in the laboratory frame colliding with a proton at rest in the atmosphere.

Chapter 2

Pierre Auger Observatory

The largest currently operating experiment detecting ultra-high-energy cosmic rays is the Pierre Auger Observatory [9]. The Observatory is located in the Southern hemisphere in Argentinian pampa in the province Mendoza at the mean altitude of 1400 m. The experiment was originally designed to study cosmic rays with energies above 10^{18} eV. However, over the time of the existence of the observatory new detection and reconstruction techniques were added to the Observatory that allow measurement of cosmic rays with energies down to $\sim 10^{15.5}$ eV [35].

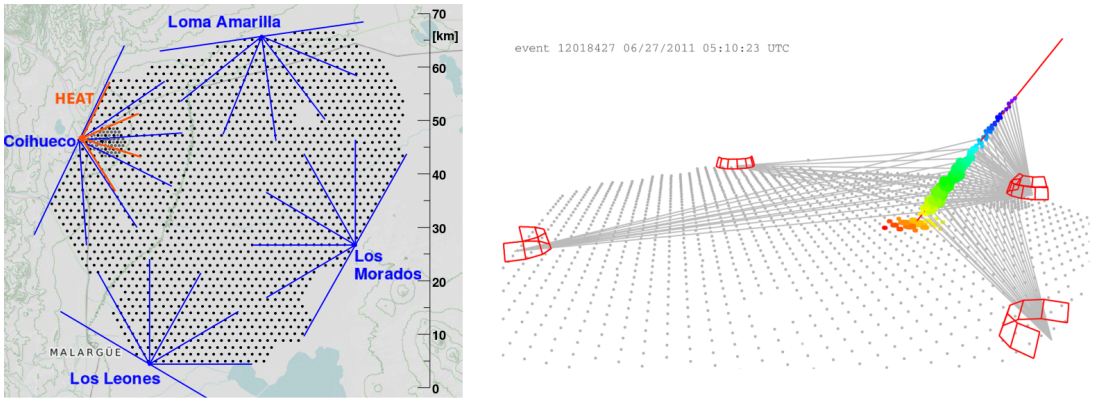

Figure 2.1: *Left:* Schematic view of the Pierre Auger Observatory. Each black dot corresponds to a water Cherenkov surface detector. The field of view of the fluorescence telescopes is shown in blue lines. Taken from [36]. *Right:* Example of an extensive air shower detected by surface and fluorescence detectors of the Pierre Auger Observatory. The colour represents the timing of the signal. Taken from [37].

The proposal to build such an observatory was initially introduced by Alan Watson and Jim Cronin on the International Cosmic Ray Conference in 1992 [38]. The construction of the Observatory began in 2000 and it was finished in 2008. However, scientific data have been collected since 2004. The Pierre Auger Observatory is a so-called hybrid observatory, which means that it utilizes two independent techniques for measuring extensive air show-

ers. Firstly, there is an array of more than 1600 surface detectors (SDs) that are placed in the pampa on a total area of $\sim 3000\,\mathrm{km}^2$. This array is overseen by fluorescence detectors (FDs) that are placed on four locations at the edges of the surface array. The fluorescence detectors measure the longitudinal profile of air showers, while the SDs detect the lateral profile of air showers at the ground level. An illustration of the Pierre Auger Observatory with its surface detectors and the stations of fluorescence detectors is shown in Figure 2.1 together with a visualisation of a UHECR event detected jointly by SDs and FDs.

In addition to the surface array and fluorescence-detector sites, the Observatory also incorporates various other instruments essential for the calibration of the detectors and for a precise measurement of the atmospheric conditions. As the atmosphere serves as a giant calorimeter, comprehensive knowledge of the atmospheric conditions, such as the cloud coverage, aerosol content, and other related properties, is crucial for an accurate reconstruction of cosmic-ray showers from the measured data. More information about the atmospheric monitoring can be found in [39]. The Observatory also incorporates other detection techniques such as an array of radio stations AERA or underground muon detectors AMIGA.

The array of surface detectors of the Pierre Auger Observatory is introduced in Section 2.1, while Section 2.2 provides an overview of the fluorescence telescopes of the experiment. The reconstruction techniques of the detected cosmic-ray showers are described in Section 2.3. Selected results of the Pierre Auger Observatory are presented in the following chapter.

2.1 Array of surface detectors

The surface array of the Pierre Auger Observatory is composed of more than 1600 surface detectors that are placed on a regular triangular grid with spacing 1.5 km between individual tanks on an area of $\sim 3000\,\mathrm{km}^2$. The regular surface array exhibits $\sim 100\%$ efficiency in detecting cosmic rays with energies above $\sim 2.5 \cdot 10^{18}$ eV [40]. Additionally, a sub-array of ~ 60 surface detectors called the *infill* with a spacing of 750 m is placed near the Coihueco FD station, enabling the detection of cosmic rays down to $\sim 10^{17}$ eV. The surface array ensures a uniform exposure up to zenith of $\sim 60^\circ$.

The individual detectors are self-powered water Cherenkov detectors (WCDs) with diameter of 3.6 m and height of 1.2 m filled with 12,000 litres of purified water. The power to each station is provided by a solar photovoltaic system. Moreover, each station is equipped with a GPS receiver that is crucial for precise timing of the signal and communication between the individual WCDs. The inner surface of the detectors is covered by a sealed liner with reflective surface. There are three 9" photomuliplier tubes (PMTs) placed on the upper side of the WCD looking downward into the water volume. The PMTs collect the Cherenkov light produced by charged relativistic particles travelling through the WCD. The height of the tank also allows for detection of high energy photons that give rise to energetic electron-positron pairs inside the water volume.

The signal registered in WCDs is quantified in units of VEM (vertical equivalent muon)

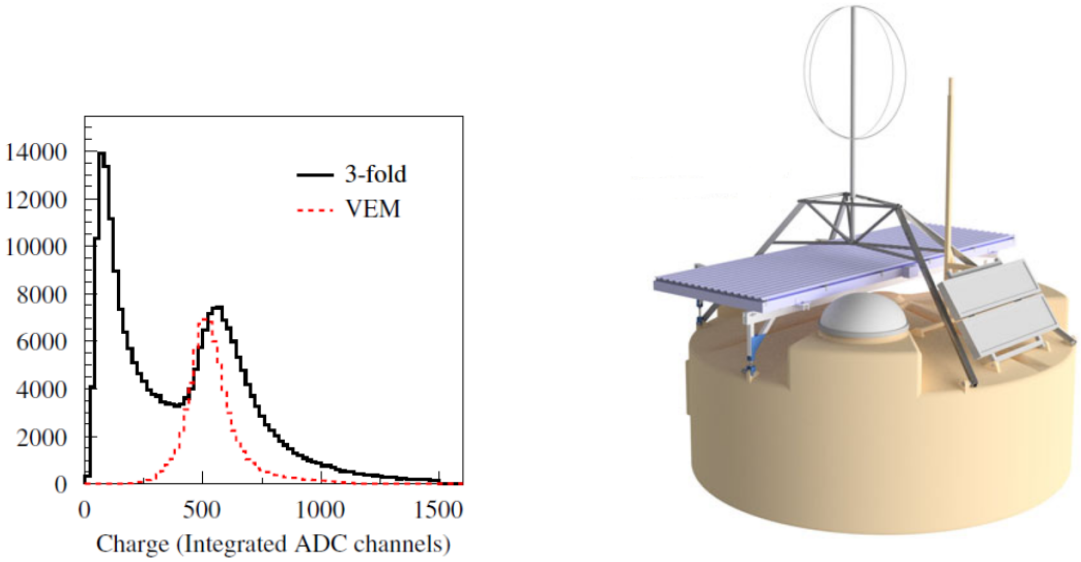

Figure 2.2: *Left:* The charge distribution obtained from the three PMTs in the surface detector (black solid line). The dashed red line corresponds to the signal from vertical and central muons. Taken from [41]. *Right:* Visualisation of the upgraded surface detector of the Pierre Auger Observatory with the plastic scintillator and the radio antenna. Taken from [42].

that corresponds to the signal induced by a passage of a vertical and central through-going muon. Atmospheric muons are used for the calibration of WDCs in real time. However, as not all the atmospheric muons are vertical and central through-going, the VEM measurement is derived from the charge distribution $Q_{\mathrm{VEM}}^{\mathrm{peak}}$ in the PMT response. Within the charge distribution of the sum from all three PMTs, the peak $Q_{\mathrm{VEM}}^{\mathrm{peak}}$ corresponds to approximately 1.09 VEM [41]. The charge distribution for the sum of the three PMTs and the VEM signal is shown in the left panel of Figure 2.2.

To ensure selection of high-quality data, a hierarchical system of triggers is applied to data measured by the SD stations before the reconstruction of signals is performed. The geometry of the shower and the energy of the primary particle are then reconstructed based on the lateral distribution of the ground signal, see Section 2.3.

The WCD stations described in the paragraphs above can not easily distinguish between the muonic and the electromagnetic components of the shower. However, such discrimination is of great interest as it allows for better mass-composition discrimination from the measurements by SDs. For that reason, the Pierre Auger Observatory recently underwent an upgrade called *AugerPrime* [43]. Within the upgrade, the surface detectors were substantially upgraded. On top of $\sim$ 1500 WCDs, a surface scintillation detectors (SSDs) are installed. The SSDs are composed of two 2 m^2 plastic scintillators and the signal is read out via wavelength shifting fibers that are placed inside the scintillator and pass the signal into a single PMT. Apart from the SSDs, each WCD is equipped with an enhanced

electronics that will increase the frequency of recorded signals (from 40 MHz to 120 MHz) and a radio antenna for detection of inclined showers (with zenith angle $> 60°$) as more stations with sufficient radio signal are triggered. Visualisation of the surface detector after the *AugerPrime* upgrade is shown in the right panel of Figure 2.2.

2.2 Fluorescence detectors

There are four stations of fluorescence detectors that are placed on small hills on the edges of the SD array of the Pierre Auger Observatory; Coiuheco, Loma Amarilla, Los Morados and Los Leones. One FD station contains six fluorescence telescopes, each with a field of view $30° \times 30°$ in azimuth and elevation. The minimal elevation of each telescope is $\sim 1.5°$. The field of view of individual telescopes is illustrated with blue lines in the left panel of Figure 2.1. The telescopes face towards the interior of the SD array and with six telescopes on each FD site, a total of 180° field of view in azimuth is achieved. Such placement of the telescopes grants $\sim 100\%$ FD trigger probability of events above 10^{19} eV falling inside the SD array [44] during clear moonless night.

The FDs detect fluorescence light that is emitted isotropically by nitrogen molecules that are excited and ionized during the evolution of the air shower. The emitted photons fall within the wavelength range of $\sim (300 - 430)$ nm. The fluorescence light emitted in the atmosphere is proportional to the energy deposited due to the electromagnetic energy losses by the charged particles in the air shower. The atmosphere thus serves as a large calorimeter and by measurement of the fluorescence light as a function of the slant depth X, the FDs measure the longitudinal profile of the shower $\propto \mathrm{d}E/\mathrm{d}X$. Integral of this profile corresponds to approximately 90% of the energy of the primary particle, the remaining *invisible energy* is carried away mainly by neutrinos and high-energy muons. The Cherenkov light from secondary particles can contribute significantly to the signal in FDs as well is some shower geometries pointing close to the telescope aperture.

Since the FDs measure the longitudinal profile of the shower development, they can directly see the shower maximum X_{max}, which makes them perfect for mass composition analysis. However, it is important to note that the fluorescence light emitted during the shower development is relatively faint. Therefore, it can be only measured during nights without a strong light pollution by the moon (less than $\sim 60\%$). Consequently, the duty cycle of FDs is only about 15% of the total time [9].

The fluorescence telescopes are situated inside a clean climate-controlled building with stable conditions. The layout of the six telescopes in the building is shown in the left panel of Figure 2.3. The fluorescence light enters through a UV filter, that is designed to transmit light in the range of wavelengths $(290 - 410)$ nm that corresponds to almost the full range of the nitrogen fluorescence light [44]. The light is focused by a segmented mirror with area ~ 13 m^2 into a photo-multiplier camera with 440 pixels located on the focal surface of the telescope [9]. Each pixel corresponds to a resolution of $1.5° \times 1.5°$ on the sky. The signal from the camera is digitized in the front-end electronics with timing of 100 ns. The schematic of the fluorescence telescope is depicted in the right panel of

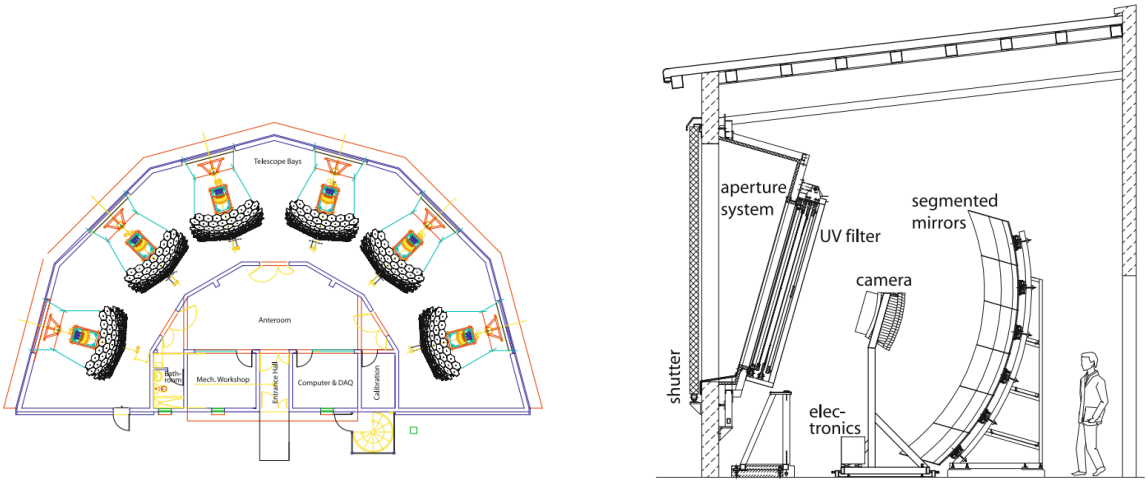

Figure 2.3: *Left:* Illustration of the FD building with six fluorescence telescopes. *Right:* Visualisation of the fluorescence telescope of the Pierre Auger Observatory. Figures taken from [44].

Figure 2.3. A shutter is installed in front of each telescope that closes during the day time and protects the camera from high illumination. The shutters are also closed during rain or high-wind conditions.

Apart from the 24 fluorescence telescopes, there exist three additional telescopes denoted as HEAT (High Elevation Auger Telescopes) placed at the Coihueco site. These telescopes can be elevated to an extra angle of 30° enabling the observation of lower-energy showers that develop at higher altitudes within the atmosphere.

2.3 Reconstruction of cosmic-ray showers

There are multiple reconstruction techniques used at the Pierre Auger Observatory that depend on the type of the detectors that measured the signals of cosmic-ray showers. Largest amount of showers is detected by the SD array as it has almost 100% duty cycle. Hybrid reconstruction is applied on showers that were measured simultaneously by FDs and SDs. Showers that were detected only by FD can be reconstructed as well, by mono or stereo FD reconstruction, see e.g. [35]. Furthermore, lower energy events detected by FD stations dominated by the Cherenkov light can be reconstructed using the Profile Constrained Geometry Fit, see [35]. In the following paragraphs, the general approach of the hybrid and SD reconstruction is briefly introduced.

2.3.1 Hybrid reconstruction

The hybrid reconstruction is based on the signal measured by fluorescence detectors and the timing information from at least one triggered SD station. The signal from fluorescence

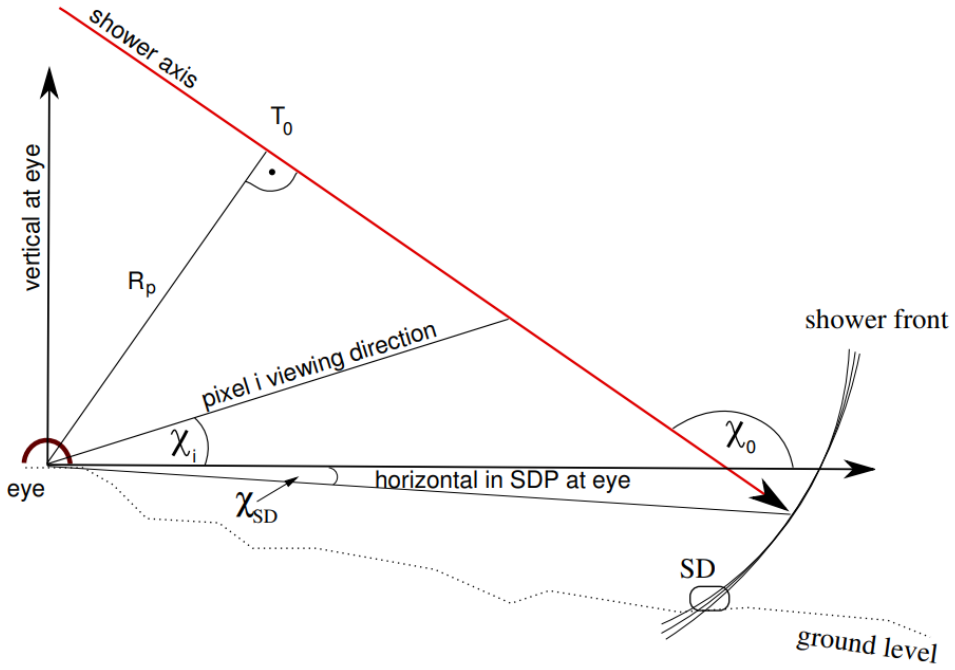

Figure 2.4: The geometry of the shower in the shower detector plane. Taken from [9].

detectors is cleaned from noise and then the shower detector plane (SDP) is obtained by minimization of the function

$$S = \frac{1}{\sum_i q_i} \sum_i q_i \left(\frac{\frac{\pi}{2} - \arccos(\vec{p}_i \cdot \vec{n}_\perp^{SDP})}{\sigma_{SDP}} \right)^2 , \tag{2.1}$$

where the sums run over all pulses i, q_i is the signal in the i^{th} pixel, $\vec{n}_\perp^{SDP}$ is a vector normal to the SDP in spherical coordinates, $\vec{p}_i$ is the pointing direction of the i^{th} pixel and $\sigma_{SDP} = 0.35°$ is the uncertainty of the SDP fit. The SDP is the plane that contains the shower axis and the triggered pixels of fluorescence telescopes.

The shower projection detected by the camera of the fluorescence telescope evolves along the SDP. The time of each pulse is used to fit geometrical parameters of the shower T_0, R_p and χ_0. The shower geometry in the SDP plane is illustrated in Figure 2.4. The angular movement of the shower can be described as

$$t(\chi_i) = T_0 + \frac{R_p}{c} \tan\left(\frac{\chi_0 - \chi_i}{2} \right), \tag{2.2}$$

where χ_i is the viewing angle of the i^{th} pixel with respect to the horizontal axis at the telescope and c stands for the speed of light. Parameter T_0 corresponds to the time of the closest approach of the shower to the telescope, R_p is the perpendicular distance between the telescope and the shower axis and χ_0 describes the angular orientation of the shower axis (see Figure 2.4).

After the geometry of the shower is reconstructed, the signal measured by the FD as a function of time is converted to the energy deposited by the shower as a function of the slant depth X. For the correct estimation of the energy profile of the air shower, individual components of the collected light have to be identified and disentangled. The dominant component of the detected FD signal from EASs above 10^{17} eV comes from the light of fluorescence emission. However, other components, like the Cherenkov radiation or Mie and Rayleigh scattered light, can be present in the detected signal as well. The energy deposit profile is obtained from the fluorescence yield that describes the proportionality between the fluorescence intensity and the energy deposit. The fluorescence yield used in the Pierre Auger Observatory comes from the precise measurements by the Airfly collaboration [45, 46].

The energy deposit profile can be parameterized by the Gaisser-Hillas function (or its modifications)

$$f_{GH}(X) = \left(\frac{\mathrm{d}E}{\mathrm{d}X}\right)_{\max} \left(\frac{X - X_0}{X_{\max} - X_0}\right)^{(X_{\max}-X_0)/\lambda} e^{(X_{\max}-X)/\lambda}, \tag{2.3}$$

where $\left(\frac{\mathrm{d}E}{\mathrm{d}X}\right)_{\max}$ is the maximum of the energy deposit at depth $X = X_{\max}$ and X_0 and λ are shape parameters without a specific physical interpretation [47]. The energy of the primary particle is obtained by integrating Equation (2.3) and correcting for the invisible energy [48]. Shower maximum is obtained as one of the fitted parameters. The footprint of the detected signal in the FD and the fitted longitudinal profile of a shower detected by the Pierre Auger Observatory is shown in Figure 2.5 for a particular event example. The energy resolution obtained from fluorescence detectors is $\sim 7\%$ and it is rather constant with energy as it provides an almost calorimetric measurement of the shower. The systematic uncertainty on the energy estimation is about 14% [40].

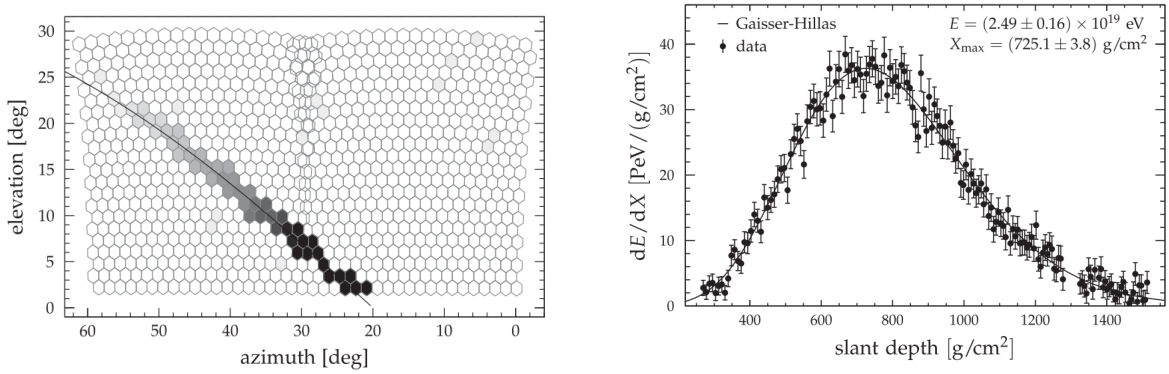

Figure 2.5: *Left:* An example of a footprint of a cosmic-ray shower detected by the fluorescence detector of the Pierre Auger Observatory. The colour denotes the timing of the signal, with darker colour corresponding to the later signal. The line represents the shower detector plane. *Right:* Longitudinal profile of a cosmic-ray shower reconstructed from signals in the left panel that is fitted with Gaisser-Hillas function. Taken from [49].

2.3.2 Surface-detector reconstruction

The cosmic-ray shower can be reconstructed purely based on the signal detected by the SD array. The detected showers are divided into two categories based on their zenith angle θ; *vertical showers* ($\theta < 60°$) and *inclined showers* (above $\sim 60°$). The inclined showers travel larger atmospheric depths and the shower maximum occurs higher in the atmosphere with respect to the vertical showers. This leads to a depletion of the electromagnetic component of the shower and the shower is dominated by muons from pion decays at the ground level. The muons are deflected by the Earth's magnetic field which needs to be taken into account during the reconstruction of inclined showers. The details of reconstruction of the inclined showers can be found in [50]. In the following paragraphs, only the classical reconstruction of the vertical events is described.

Showers initiated by cosmic rays with energy $\sim 10^{19}$ eV are typically of size of more than $20\,\mathrm{km}^2$ on the ground and therefore trigger multiple SD stations within the array. The signal and timing of the signals in individual triggered SD stations is used for the reconstruction of the shower. The first estimation of the arrival direction of the shower is obtained from timing of the signals in triggered stations. This geometry is used to determine the radius of curvature of the inflating sphere. The lateral distribution of the signal is fitted by a lateral distribution function (LDF). The lateral distribution can be described by a modified Nishimura-Kamata-Greisen function

$$S(r) = S(r_{\mathrm{opt}}) \left(\frac{r}{r_{\mathrm{opt}}}\right)^{\beta} \left(\frac{r + r_1}{r_{\mathrm{opt}} + r_1}\right)^{\beta+\gamma}, \tag{2.4}$$

where S is the signal at the distance r from the shower axis, r_{opt} is the optimum distance, $r_1 = 700$ m and β and γ are fitted parameters, where β is zenith dependent. The optimal distance for the regular array was chosen for the main Auger SD array as 1000 m [51]. The signal at optimum distance $S(1000)$ is used as an energy estimator. An example of the size of the signal with respect to the distance to the shower axis is depicted in the left panel of Figure 2.6.

Because of the attenuation of the shower in the atmosphere, the $S(1000)$ decreases with zenith angle for a given primary energy. For that reason, the $S(1000)$ is corrected by the Constant Intensity Cut function $f_{\mathrm{CIC}}(\theta)$ [53] to the median zenith angle 38°. The signal $S(1000)$ is converted into the $S_{38} = S(1000)/f_{\mathrm{CIC}}(\theta)$ corresponding to a signal at 1000 m from the shower core generated by the same shower if it would impact with zenith $\theta = 38°$ [1]. The S_{38} is used to estimate the energy of the primary particle. High-quality hybrid events are used to cross-calibrate the relation between the reconstructed energy from the fluorescence detectors E_{FD} and the S_{38} signal. Their relation is described as

$$E_{\mathrm{FD}} = A S_{38}^{B}, \tag{2.5}$$

[1] These parameters of the optimum distance and the median zenith angle are only valid for the regular array with spacing 1500 m. For the infill array, the $r_{\mathrm{opt}} = 450$ m and the median angle is 35°.

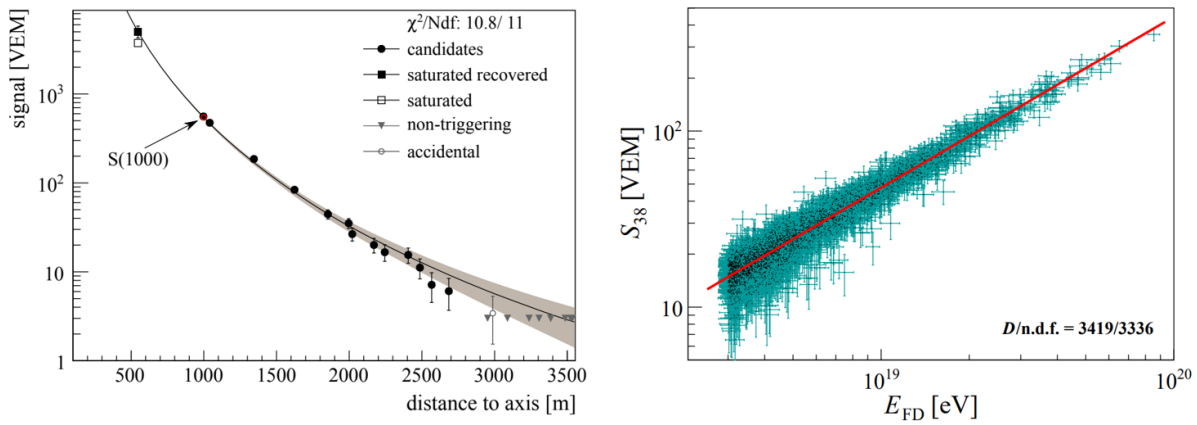

Figure 2.6: *Left:* Lateral distribution of the signal detected by the SD stations of the Pierre Auger Observatory fitted by a lateral distribution function. Taken from [9]. *Right:* The correlation between the S_{38} signal and the FD energy at the Pierre Auger Observatory fitted with the calibration function in Equation (2.5). Taken from [52].

where parameters A and B are obtained from the golden-hybrid events[2]. The correlation of the S_{38} and the FD energy is shown in the right panel of Figure 2.6 together with the fit assuming the relation in Equation (2.5). The energy resolution of the SD reconstruction improves with energy, decreasing from $\sim$ 16% in the low energy part to $\sim$ 12% at the highest energies [9].

The axis of the shower $\hat{a}$ is reconstructed from the shower impact point on the ground $\vec{x_{gr}}$ and the shower origin $\vec{x_{sh}}$ obtained from the geometrical reconstruction. It is defined as

$$\hat{a} = \frac{\vec{x_{sh}} - \vec{x_{gr}}}{|\vec{x_{sh}} - \vec{x_{gr}}|}. \tag{2.6}$$

The SD reconstruction has relatively precise angular resolution of showers with an energy above $\sim 3 \cdot 10^{18}$ eV where the SD array has almost 100% trigger efficiency. This resolution is improving with increasing zenith angle as more stations are triggered with the increasing shower footprint. For events that triggered three stations the angular resolution is better than 1.6° and events triggering more than six stations have resolution better than 0.9° [9].

[2]Golden hybrid events are high quality events that independently trigger both FD and SD and can be fully reconstructed in both detection modes.

Chapter 3

Propagation of cosmic rays in the universe

Ultra-high-energy cosmic rays are believed to be of an extragalactic origin. The distances that these cosmic rays need to traverse before they are detected on Earth are ranging from a few megaparsecs (Mpc) to tens or even hundreds of megaparsecs. The horizon of UHECRs is, however, limited. This limitation arises from the interactions of cosmic rays with the ambient photon backgrounds in the universe. The most prominent photon background in the universe is the cosmic microwave background (CMB). Apart from CMB, cosmic rays can also interact with the extragalactic background light (EBL), that encompasses other photon energies than CMB. Moreover, cosmic rays also interact with electron plasma or hydrogen gas clouds that are present in the Universe. Such interactions are causing energy losses of cosmic rays, thus limiting the horizon of their possible origin. On cosmological scales, another energy loss mechanism arises due to the cosmological redshift.

Cosmic rays also encounter magnetic fields that are present on both small and large scales in the universe. When a charged particle propagates through a magnetic field its trajectory is deflected due to the Lorenz force and its direction thus does not need to point back to its source. The extent of these deflections depends on the strength and characteristics of the encountered magnetic fields. Cosmic rays might experience small deflections of the order of a few degrees. However, under certain conditions, the propagation may transform into a diffusive regime, leading to a loss of all information about the particle's origin.

This chapter is devoted to the cosmic-ray propagation effects in the universe. The major energy loss processes of cosmic rays caused by interactions with photon backgrounds and by the expansion of the universe are presented in Section 3.1. Section 3.2 provides an overview of the properties and influence of magnetic fields on the cosmic-ray propagation, encompassing both Galactic and extragalactic magnetic fields. This section also introduces two models of the Galactic magnetic field relevant to the research presented in Chapter 5.

3.1 Energy losses of protons and nuclei

Cosmic rays propagate mainly in the interstellar/intergalactic medium where the matter density is negligible. Consequently, the energy losses of cosmic rays primarily result from interactions with the surrounding photon fields. Since the energy losses of UHECRs with matter are negligible, they will not be described here.

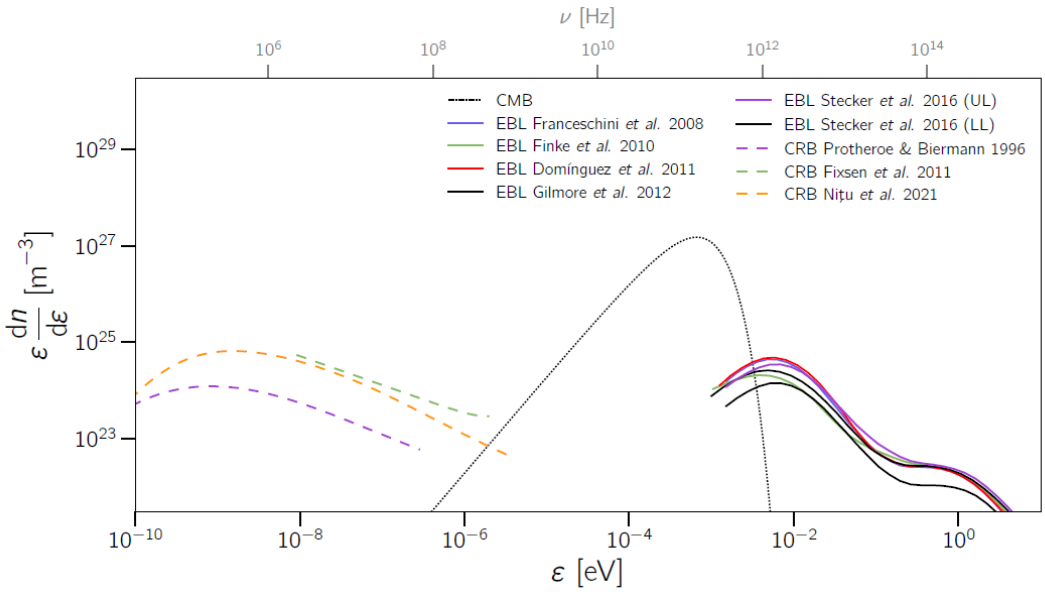

Figure 3.1: Photon densities of cosmic background photon fields at redshift $z = 0$. The dashed lines correspond to the models of cosmic radio background (CRB). The photon density of cosmic microwave background (CMB) is shown with dotted line and the full lines represent different models of the extragalactic background light (EBL). Taken from [54].

The principal intergalactic medium that is responsible for energy losses of cosmic rays is the cosmic microwave background radiation. This radiation is a remnant from a pivotal phase of the universe, called the recombination ($\sim 300,000$ years after the Big Bang), when the universe became transparent to photons. The CMB exhibits a black-body radiation spectrum with the mean temperature of ~ 2.725 K corresponding to the mean energy of approximately 10^{-3} eV with very low fluctuations of the temperature (of the order $\sim 10^{-5}$) [55]. Cosmic rays can also interact with the extragalactic background light composing of ultra-violet, optical and infra-red light originating in various astrophysical sources in the universe. While the CMB is very uniform in its nature and can be well described, the EBL displays considerable variability and its description is model dependent. Numerous models of the EBL have been proposed and adopted within the astroparticle community, see for example references [56–61]. The photon densities as a function of energy are shown in Figure 3.1 for CMB, different models of EBL and the radio backgrounds. It is worth noting that while radio background is relevant for the gamma-ray propagation, it does not significantly affect UHECRs.

There are different dominant interactions causing the energy losses depending on the energy and mass of the cosmic-ray particle. The mean free path λ of a cosmic ray with Lorentz factor Γ at a redshift z interacting with a diffuse photon background can be expressed as

$$\lambda^{-1}(\Gamma, z) = \frac{1}{2\Gamma^2} \int_0^\infty \int_0^{2\Gamma\epsilon} n(\epsilon, z) \frac{1}{\epsilon^2} \epsilon' \sigma(\epsilon') \mathrm{d}\epsilon' \mathrm{d}\epsilon, \tag{3.1}$$

where $\epsilon' = (1 - \cos\vartheta)\Gamma\epsilon$ is energy of the photon in the nucleus' rest frame, ϵ is the energy of the photon in laboratory frame, ϑ is the angle between the momentum of the photon and the cosmic-ray particle, $n(\epsilon, z)$ is the spectral number density of photons, and $\sigma(\epsilon')$ is the cross-section of the interaction of the cosmic ray with the photon [55].

The main interactions of UHECRs with ambient photon fields are the production of electron-positron pair, photopion production and the photodisintegration (in case of heavier nuclei). In instances where an unstable nucleus is generated either at the source or as a consequence of photodisintegration, the nuclear decay might also account for an energy loss. Furthermore, since the particles travel large distances, the energy losses caused by the expansion of the universe must be taken into account as well. The evolution of the energy loss lengths corresponding to the individual energy loss processes with energy is shown in Figures 3.2 and 3.3 for nitrogen and iron nuclei, respectively. Individual energy loss processes are described in more detail below.

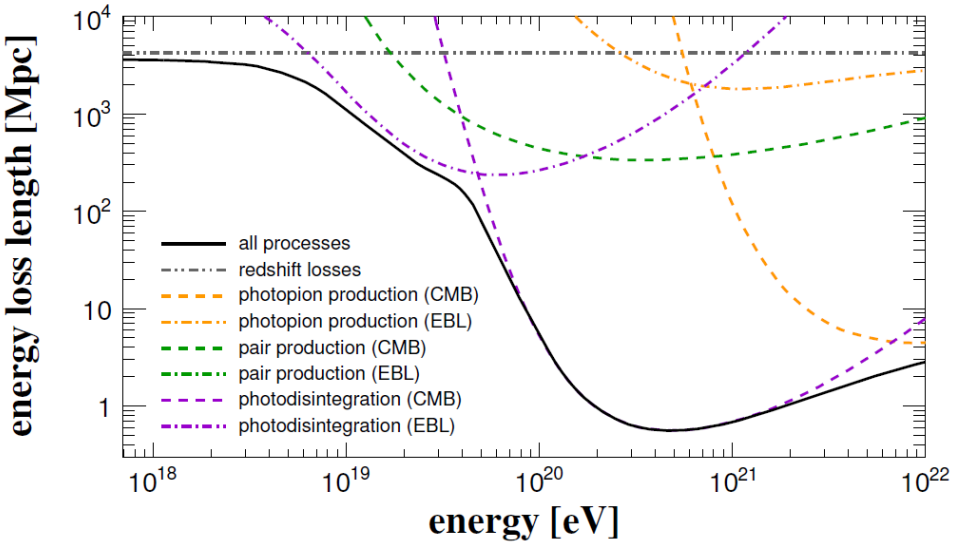

Figure 3.2: Evolution of the energy loss length of ^{14}N with energy for different processes; photopion production in orange, pair production in green and photodisintegration in purple. The interactions on CMB are shown in dashed lines and the interactions on EBL are depicted in dash-dotted lines. The grey line represents the energy losses due to the expansion of the universe. The total energy loss length taking all the processes together is shown in full black line. Taken from [55].

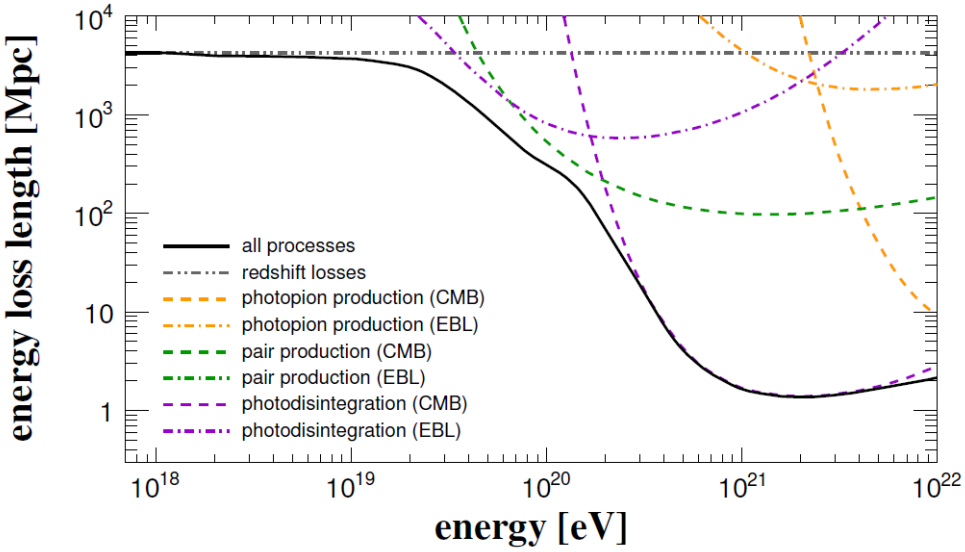

Figure 3.3: Same as Figure 3.2 but or an iron nuclei ^{56}Fe. Taken from [55].

Pair production

Cosmic rays with Lorentz factor $\Gamma \geq 10^9$ can lose energy via the creation of an electron-positron pair. The process can be written as

$$ {}^{A}_{Z}X + \gamma \rightarrow {}^{A}_{Z}X + e^{+} + e^{-}, \tag{3.2} $$

where A is the nucleon number and Z is the proton (charge) number. The threshold energy for pair production is

$$ E^{\pm}_{thres} = \frac{m_e(m_X + m_e)}{\epsilon} \simeq 4.8 \cdot 10^{17} A \left(\frac{\epsilon}{10^{-3}\,\mathrm{eV}} \right)^{-1} \mathrm{eV}, \tag{3.3} $$

where m_e and m_X are the masses of electron/positron and of the nucleus X, respectively, and ϵ represents the energy of the background photon [62]. For an interaction with CMB, the typical threshold energy is $E^{\pm}_{thres} \sim 10^{18}$ eV. The interaction length of pair productions is relatively low ($\sim$ 450 kpc) compared to the the other energy loss processes [63]. Nevertheless, the energy of the cosmic ray is only slightly altered by one pair production and the interaction length does not correspond to the horizon of UHECRs. Therefore, this process is usually treated as a continuous energy loss.

Photopion production

The photopion production is one of the most significant energy losses of UHECRs at the highest energies. A nucleon N interacts with a background photon and a pion is created that carries away part of the nucleon's energy. The photopion production can be expressed as

$$N + \gamma \to N' + \pi. \tag{3.4}$$

Protons with Lorentz factor $\Gamma > 10^{10}$ can interact with a CMB photon and create a pion that gains part of the energy of the nucleon. At lower energies, this process can also occur on the EBL with lower probability [63]. The proton interacts with the photon and it is excited into a Δ^+ resonance before it decays. In this process, both neutral or charged pion can be created with different branching ratio as

$$p + \gamma \to \Delta^+ \to \begin{cases} n + \pi^+ & \text{with branching ratio } 1/3 \\ p + \pi^0 & \text{with branching ratio } 2/3 \end{cases}. \tag{3.5}$$

A significant part of the cosmic-ray energy ($\sim 20\%$) is taken away by the newly created pion. In fact, this process taking into account interactions of protons with CMB was used for establishing the famous GZK limit [64, 65] that predicts a suppression of the flux of cosmic rays with energies above $\sim 3 \cdot 10^{19}$ eV. The threshold energy for this process is

$$E^{N,\pi}_{thres} = \frac{m_\pi (m_N + \frac{1}{2} m_\pi)}{2\epsilon} \simeq 6.8 \cdot 10^{19} \left(\frac{\epsilon}{10^{-3}\,\mathrm{eV}} \right)^{-1} \mathrm{eV}, \tag{3.6}$$

where m_π and m_N are the masses of the pion and the nucleon, respectively, and ϵ represents the energy of the background photon [62]. The mean free path of this process for protons with energy $E > E^{N,\pi}_{thres}$ is approximately 6 Mpc. Because of the high energy loss in each such interaction, this process strictly limits the horizon of the UHECRs.

In case of heavier nuclei, the photopion production can be approximated by the superposition model. The nucleus is treated as a superposition of A free co-moving nucleons. Therefore, the threshold energy is proportional to the atomic number as $E^{A,\pi}_{thres} = E^{N,\pi}_{thres} \cdot A$.

Photodisintegration

The most prominent process of energy loss of ultra-high-energy nuclei is the photodisintegration. In this process, a CMB or EBL photon is absorbed into the nuclei, which becomes excited. As a consequence the nuclei can be stripped of one or multiple nucleons. Therefore, this process not only changes the energy of the particle, but it also changes its mass composition.

At photon energies $\epsilon' < 30$ MeV (in the nucleus' rest frame) the process is dominated by a giant dipole resonance that is a collective excitation of the nucleus. This process usually ends with an emission of one nucleon. Nevertheless, more nucleons or an alpha particle can be emitted with lower probability as well [66]. At intermediate energies $3\,\mathrm{MeV} < \epsilon' < 150\,\mathrm{MeV}$, the quasi-deuteron process occurs. This process leads to an emission of multiple nucleons [55]. Above $\epsilon' > 150\,\mathrm{MeV}$ the cross-section of the photodisintegration vanishes and the photo-pion production becomes the dominant energy loss process.

The effective energy loss rate of the photodisintegration of nucleus can be described as

$$\left.\frac{1}{E}\frac{\mathrm{d}E}{\mathrm{d}t}\right|_{eff} = \frac{1}{A}\frac{\mathrm{d}A}{\mathrm{d}t} = \sum_i \frac{i}{A} R_{A,i}(E), \tag{3.7}$$

where $R_{A,i}$ is the rate for emission of i nucleons from a nucleus with the mass number A [62].

Cosmological redshift

Besides the energy losses caused by interactions of UHECRs with photons, cosmic rays are also affected by the expansion of the universe resulting in an energy loss. This process is dominant at lower energies, below the energy threshold of pair production (see Figures 3.2 and 3.3).

Adiabatic energy loss rate caused by the cosmological redshift can be described as

$$-\frac{1}{E}\frac{\mathrm{d}E}{\mathrm{d}x} = H(z) = H_0\sqrt{\Omega_m + (1+z)^3\Omega_\Lambda}, \tag{3.8}$$

where z is the redshift at time t, $H_0 \sim 70$ km/s/Mpc is the Hubble constant at current time, the Ω_m is the density of matter, and Ω_Λ is the density of dark energy [55]. The energy loss length of cosmic rays via the cosmological redshift is ~ 4 Gpc, which is far more than the energy loss lengths of the energy loss processes caused by interactions with photons. The energy losses of protons are dominated by the expansion of the universe up to the energy of $\sim 2 \cdot 10^{18}$ eV, where the pair production becomes relevant [67].

3.2 Propagation of cosmic rays in magnetic fields of the universe

Ultra-high-energy cosmic rays encounter various types of magnetic fields with different strengths during their journey from the source to the observer on Earth. Firstly, there are very strong localized magnetic fields around the particle's original source that confine them for long enough time so they can be accelerated to high energies[1]. Secondly, cosmic rays travel through extragalactic magnetic fields (EGMF), which are measured to possess strengths of few μG [68] in galaxy clusters. Finally, the cosmic-ray particle enters the Milky Way and propagates in the Galactic magnetic field (GMF).

Since cosmic rays are charged particles, their trajectories are deflected in the magnetic fields they traverse. The level of the deflection depends on the particle's energy and charge and the attributes of the magnetic field it is passing. In a uniform magnetic field, charged particle is traveling on circular trajectories, with the radius of such trajectory called Larmor radius (gyroradius) r_L. The Larmor radius in parsec units can be calculated as

[1]This statement is only valid if we assume an electromagnetic acceleration of the cosmic-ray particles.

$$\frac{r_L}{\mathrm{pc}} = \frac{E}{ZeB} \simeq 1.1 \left(\frac{E}{\mathrm{PeV}}\right) \left(\frac{\mu\mathrm{G}}{B}\right) \frac{1}{Z}, \tag{3.9}$$

where E is the energy of the particle in units of PeV, B is the strength of the magnetic field expressed in units of μG, and Z is the charge of the particle [69]. The magnetic field of a typical galaxy ($B \sim (5-15)\,\mu$G) is so strong that particles with energies $\lesssim 10^{17}$ eV are confined within the galaxy as the Larmor radius is smaller than the radius of the galaxy. Larmor radius of particles with energies above $\sim 10^{17}$ eV becomes so large that they can escape the galaxy [70]. It can be seen in Equation (3.9) that the Larmor radius of the cosmic ray depends on the particle's energy and its charge. Therefore, it is more convenient to use the units of rigidity[2] when talking about the deflections of cosmic rays in magnetic fields.

The regime of cosmic-ray propagation in a turbulent magnetic field can be divided into multiple categories based on the energy of the particles. Let us define a critical energy E_c in such a way that

$$r_L(E_c) = l_c, \tag{3.10}$$

where l_c is the coherence length of the turbulent magnetic field [69]. From Equation (3.9), the critical energy is

$$E_c = ZeBl_c. \tag{3.11}$$

For very high energies $E >> E_c$, the magnetic field has little to negligible influence on the particles trajectory. For energies $E > E_c$, the particle propagates in a *non-resonant diffusion regime* where the deflections are small, on the scale of $\delta = l_c/r_L$. Once the energy of the particle is smaller than the critical energy, i.e. $E < E_c$, the particle is in the *resonant diffusion regime* and it is experiencing large deflections [69].

3.2.1 Galactic magnetic field

In general, the magnetic fields in the galaxies are mainly confined in the interstellar and intracluster medium, but they extend beyond the galactic disk to the galactic halo as well. The precise understanding of the galactic magnetic field is important not only for the studies of UHECRs, but it is also important for many other astrophysical phenomena as it is contributing to the total pressure of the galaxy and it is also an important ingredient for an early star formations [71, 72].

The structure and strength of the magnetic field depends on the type of the galaxy. In spiral galaxies, such as Milky Way, the strength of the magnetic field is $\sim 10\,\mu$G. In our

[2]Rigidity R of a particle is defined as

$$R = \frac{p}{Z} \to \frac{E}{Z},$$

where p is the particle momentum, Z is the particle charge, and E is the energy of the particle. The arrow represents a relativistic limit, where the speed of light is taken to be $c = 1$.

neighboring galaxy in Andromeda, the strength of the magnetic field is $\sim 5\,\mu$G, while in galaxies with high star-formation rate the field is stronger $\sim (20-30)\,\mu$G. The strongest magnetic fields are observed in starburst galaxies with $B \sim (50-100)\,\mu$G [71]. In spiral galaxies, the field often manifests symmetries with respect to the galactic disk and the rotation axis of the galaxy [71]. The actual strength and structure of the galactic magnetic field is extremely complex and differs on small and large scales. As the Galactic magnetic field influences many physical processes in the universe, it is possible to study the properties of the Galactic magnetic field indirectly by different observations.

Polarized Synchrotron Emission is a powerful tool for the indirect measurement of the GMF. The synchrotron light is emitted mainly by relativistic electrons in the presence of the magnetic field. The emitted radiation from a source provides information about the strength of the magnetic field and the degree of its polarization can be used to estimate the field's structure. The emissivity of synchrotron radiation with wavelength ν of a single electron of energy E in a magnetic field B is

$$J(\nu, E) \propto B_{\perp} \left(\frac{\nu}{\nu_c}\right)^{1/3} f\left(\frac{\nu}{\nu_c}\right), \tag{3.12}$$

where $B_{\perp}$ is the magnetic field strength in the direction perpendicular to the line-of-sight, ν_c is the critical frequency, and $f\left(\frac{\nu}{\nu_c}\right)$ is the cutoff function [71].

Measurement of **Faraday rotations** of polarized emission can be used for deducing the line-of-sight component of the magnetic field ($B_{\parallel}$) in the Galaxy. The Faraday rotation is a phenomenon that causes the rotation of the plane of polarization of linearly polarized wave when it passes through a magnetic field. The change of the polarization angle ϕ depends on the square of the wavelength λ as

$$\phi = \phi_0 + \mathrm{RM}\lambda^2, \tag{3.13}$$

where ϕ_0 is the polarization angle of the light from the source and RM is the rotation measure. The RM can be calculated as

$$RM = \frac{e^3}{2\pi m_e^2 c^4} \int_0^{l_s} n_e(l) B_{||}(l) \mathrm{d}l, \tag{3.14}$$

where l goes from the observer at $l = 0$ to the source at $l = l_s$, m_e is the mass of an electron, $B_{\parallel}$ is the line-of-sight component of the magnetic field, and n_e is the number density of electrons [71]. From observations of a multiwavelegth polarized source a single value of the RM is obtained that corresponds to the line-of-sight component of the magnetic field between the observer and the source. Moreover, a negative or a positive sign of the RM indicates the direction of the field [72].

Pulsars are ideal candidates for measurements of the RMs as they are highly polarized and have no intrinsic Faraday rotation. Furthermore, they are widely populated within the Galaxy. Currently, there are approximately 700 measurements of RMs from Galactic pulsars [73]. Using the RMs together with the known distances of the pulsars, a 3D map of the GMF can be obtained. Extragalactic point sources are also used to map the GMF

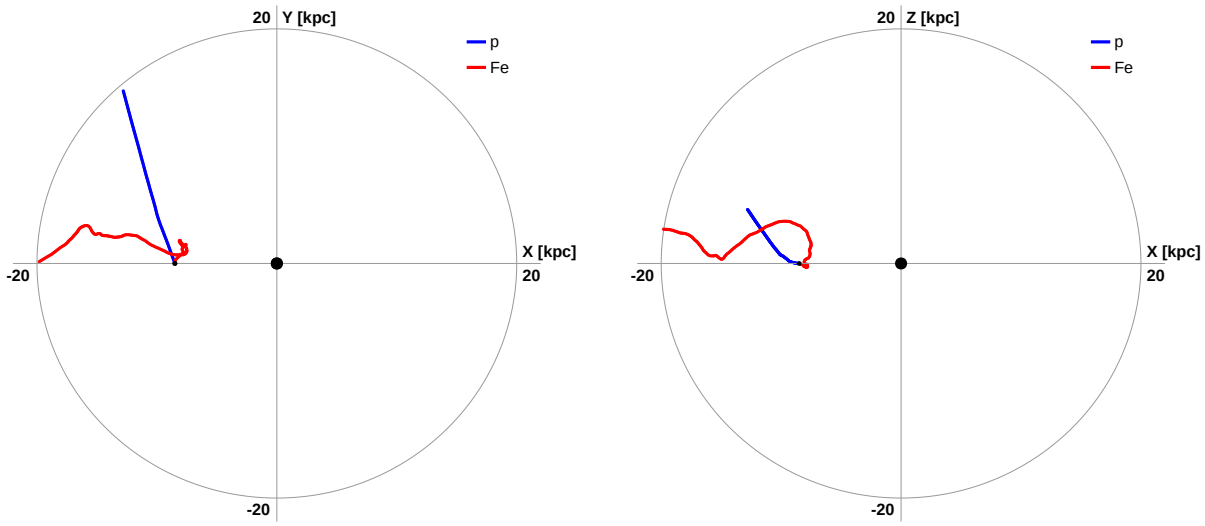

Figure 3.4: Trajectory of a backtracked proton (blue) and iron nucleus (red) with energy 10^{19} eV in the JF12 model of GMF projected into the Galactic disk xy plane (left) and xz plane (right).

using RMs. However, the RMs of extragalactic sources are corresponding to a passage through the whole Galaxy.

Other observations that can be used for indirect measurements of the GMF are the Zeeman splitting effect, Polarized Thermal Dust Emission or starlight polarization. For more detailed review of the different measurement techniques see for example [71, 72, 74].

To precisely describe the complete nature of the magnetic field of our Galaxy is a very complex problem. From the measurements of RMs, synchrotron radiation and other observations it seems that the GMF in our Galaxy is composed of a large-scale regular field component and a small-scale turbulent component, both having the strength in orders of few μG [75]. The turbulent component has coherence lengths of $\sim (50 - 150)$ pc [76] while the regular component has a coherence length of the size of the visible Galactic disc [71].

Current models of the Galactic magnetic field

Over the years, many models of the GMF have been proposed [75–79]. Individual models differ not only in the strengths of individual components of the field but also in the very components included. Some of the models suppose that the Galactic halo has a negligible magnetic effects compared to the rest of the Galaxy and some models include the halo as one of the important components that significantly contribute to the total magnetic field. Two models of the GMF, Jansson–Farrar (JF12) [75, 80] and Terral–Ferrière (TF17) [78], that are used in this work are described in more detail below.

The influence of the GMF on the propagation of UHECRs is not negligible, especially for particles with lower rigities. To illustrate different behavior of particles with the same

energy but different rigidity a trajectory of a proton and an iron nucleus with energy 10^{19} eV in the presence of the GMF (JF12 model is used) is shown in Figure 3.4 in xy plane and in xz plane. Both particles were injected with the same arrival direction on Earth. In case of ultra-high-energy protons, the deflections of cosmic rays in the GMF might be in orders of few degrees only. However, for low rigidities, the deflections might be up to 180° and the information about the origin of the particle is lost.

Jansson–Farrar model

The Jansson–Farrar model of the GMF is based on measurements of Faraday rotations and polarized synchrotron emission. The model composes of a large-scale regular field, a striated random component and a turbulent random component [75, 80].

The large-scale regular field is modeled in three separate components. The disk field is defined in the xy plane between radii of 3 kpc and 20 kpc from the Galactic center (GC). The disk field is defined purely with azimuthal component between 3 kpc and 5 kpc. Above 5 kpc, the field is modeled in 8 spiral regions following the spiral character of the

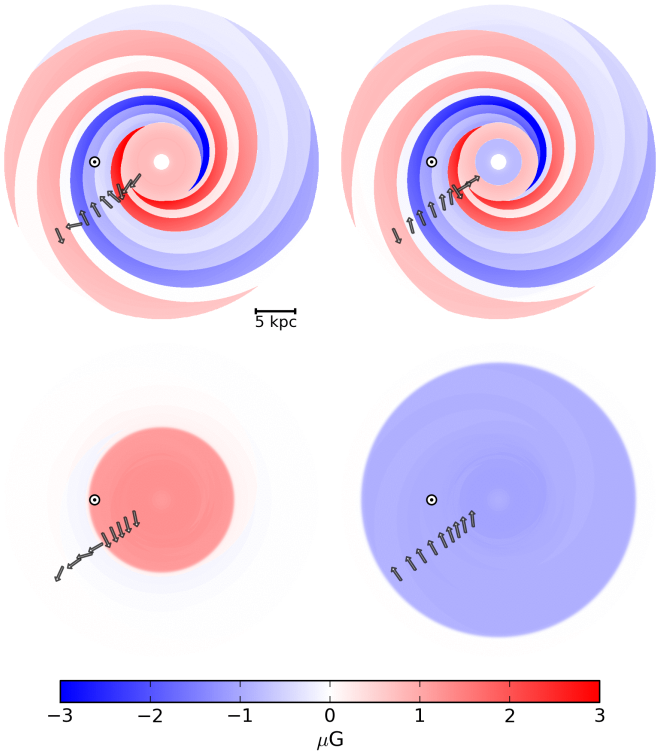

Figure 3.5: Visualisation of the strength and orientation of the JF12 model of the GMF in the Galactic disk at height $z = 10$ pc (top left), $z = -10$ pc (top right), $z = 1$ kpc (bottom left) and $z = -1$ kpc (bottom right). Position of the Solar system is marked with a circle. Taken from [75].

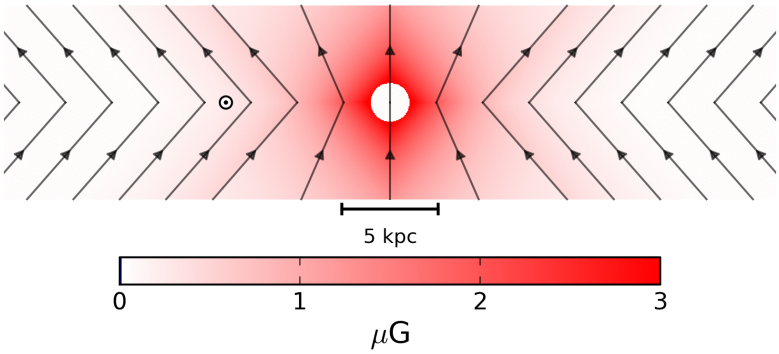

Figure 3.6: Visualisation of the strength and orientation of the JF12 X-field in the xz plane. Taken from [75].

Galaxy and the field strength decreases with radius as r^{-1} and vanishes at $r > 20$ kpc. A transition between the disk field and the toroidal halo field is defined at height $h_{\text{disk}} = 0.4$ kpc in z direction. The visualisation of the field in the plane of the Galactic disk at height $z = \pm 10$ pc and $z = \pm 1$ kpc is depicted in Figure 3.5. Finally, the halo field is accompanied by an out-of-plane halo component that is referred as the X-field. The X-field is an axisymmetric and poloidal field, lacking an azimuthal component (see Figure 3.6).

The striated field composes of random fields whose strength and orientation varies on a small scale but they are aligned to a particular axis over large-scale features of the regular large-scale component. The striated field is parameterized with respect to the regular field as $B^2_{\text{stri}} = \alpha B^2_{\text{reg}}$ with a single value of the α parameter $\alpha = 1.36 \pm 0.36$ [75]. Therefore, the striated field has the same magnitude with respect to the regular field everywhere in the Galaxy. The small-scale turbulent component of the field is composed of randomly oriented magnetic fields on small scales with coherence length l_c of the order 100 pc or less [80].

The parameters of the JF12 model are obtained using the WMAP7 Galactic synchrotron emission map [81]. However, new measurements performed by the Planck mission suggest that the original parameters should be adjusted to fit the new and more precise Planck data [82]. The most significant changes to the model parameters are the decrease of the amplitude of the X-shaped field component and decrease of the field strength in one of the arms in the disk. Furthermore, the random field was adjusted as well. In the original JF12 model, the turbulent field is dominated by one spiral arm, where the strength of the turbulent field is more than twice as large than in the rest of the arms. In this work, we use the updated parameters of the model based on the Planck measurements [82] and the field is referred to as *JF12Planck*. Visualisation of the JF12Planck field in xy plane at $z = 0$ pc and in xz plane at $y = 0$ pc is shown in Figure 3.7.

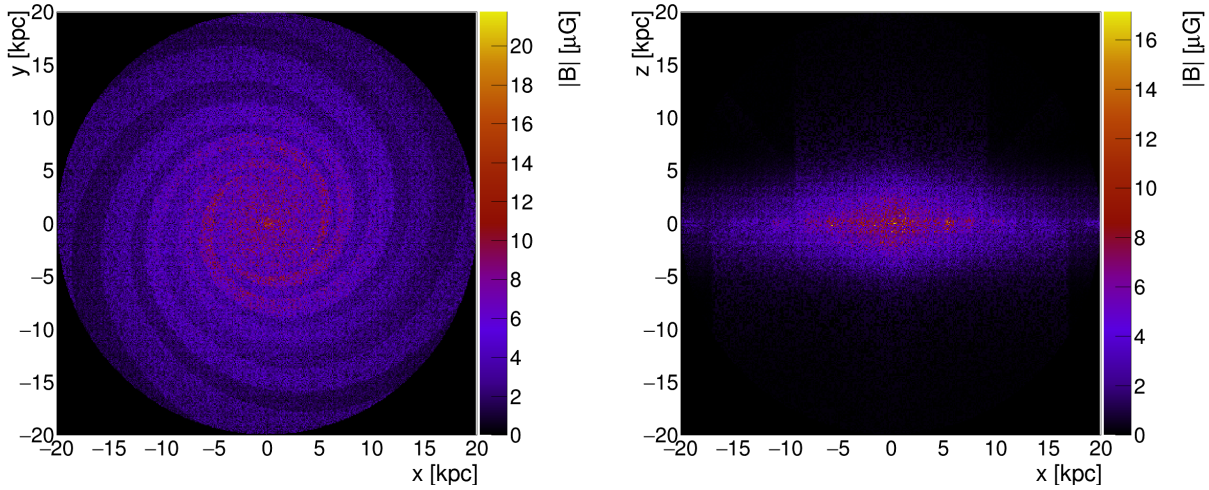

Figure 3.7: Visualisation of the strength of the JF12Planck model of GMF field in xy plane at $z = 0$ pc (left) and xz plane at $y = 0$ pc (right) with the Galactic center in the coordinates $(x, y, z) = (0, 0, 0)$ kpc. All three components of the field are included with the coherence length of the turbulent component $l_c = 60$ pc. The plots are produced with values of the strength of the field obtained from CRPropa 3 [83]. Figure taken from my publication [84].

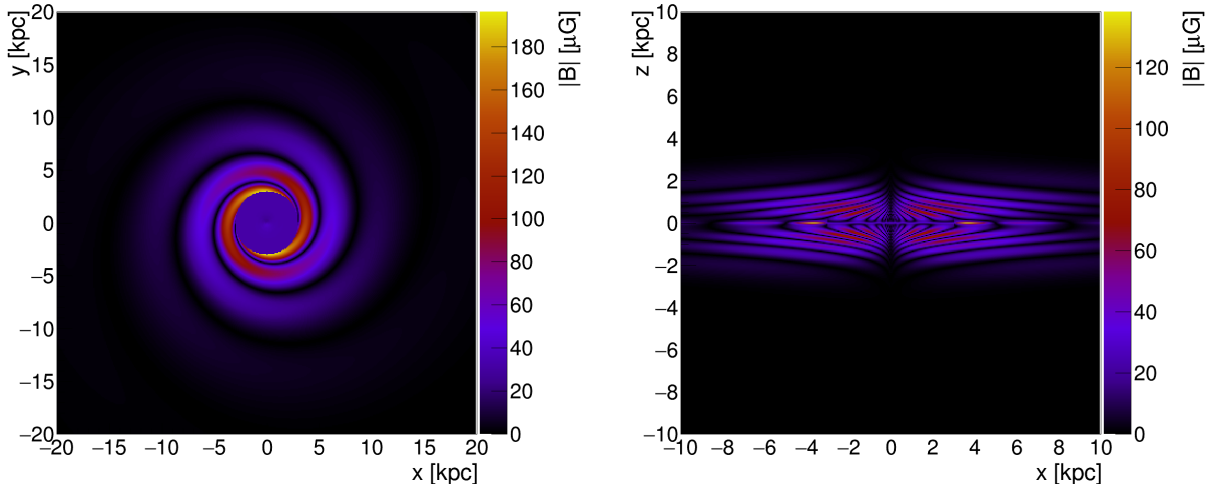

Figure 3.8: Same as Figure 3.7 but for the Ad1C1 variant of the TF17 model of the GMF. Figure taken from my publication [84].

Terral–Ferrière model

The Terral–Ferrière model of the GMF is based on measurements of Faraday rotations of extragalactic point sources [78]. The general model is composed of a halo field and a disk field. The authors investigate multiple models for both the halo and disk and their combinations. As the best fit, two models of the halo and three models of the disk are

chosen and their respective six combinations.

The three disk fields are referred to as Ad1, Bd1 and Dd1 and two models of the halo-field C0 and C1. All disk models are following the spiral character of the Galaxy and are composed of mainly horizontal magnetic fields. While the disk field is supposed to be a symmetric field, the models of the halo field are considered to be antisymmetric. The combinations of all the disk fields with the bisymmetric halo (C1) perform better than the combinations with the axisymmetric halo-field (C0). Therefore, in this work, only field models with C1 halo are taken into account. The field strength in xy plane at $z = 0$ pc and in xz plane at $y = 0$ pc for the three combinations of the TF17 field, namely Ad1C1, Bd1C1, and Dd1C1 are shown in Figures 3.8, 3.9, and 3.10, respectively. The individual models appear to have very large local values of the magnetic field mainly in the disk. The extreme values of the halo field for high z in the Bd1C1 option of the field is caused by the behaviour of the equations describing this field model, see [78]. The main goal of the TF17 model is to describe the halo-filed, therefore the results obtained with this field should be interpreted with caution.

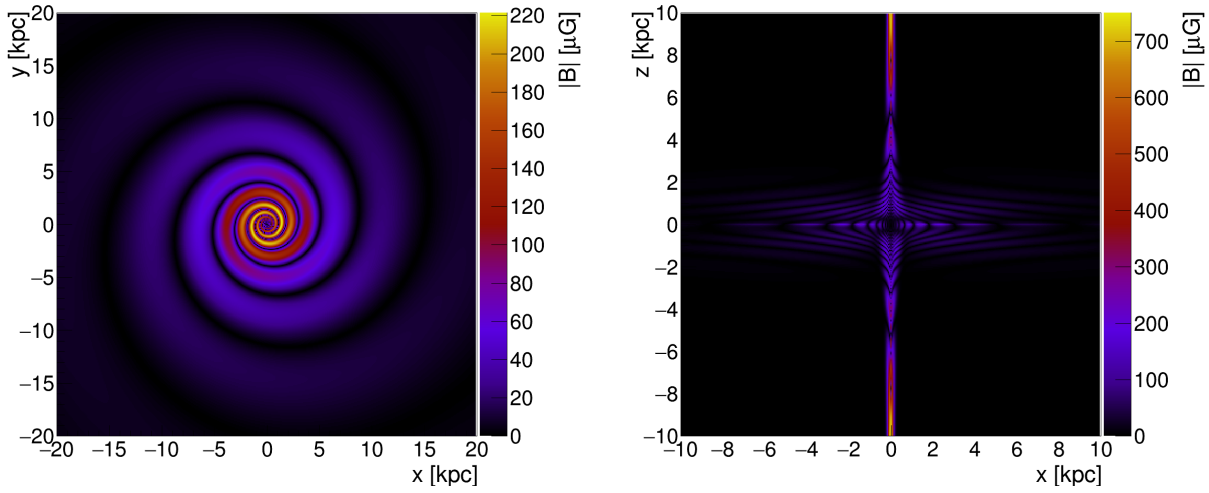

Figure 3.9: Same as Figure 3.7 but for the Bd1C1 variant of the TF17 model of the GMF. Figure taken from my publication [84].

3.2.2 Extragalactic magnetic field

The magnetic fields in the universe are not only confined within galaxies, but they extend to galaxy clusters and beyond. The exact extend of the EGMF is not well understood as well as its origin. However, it might have significant influence of the propagation of UHECRs, causing not only deflections from the direction of their source but also prolonging their trajectories and, consequently, subjecting them to more energy losses compared to the propagation on straight lines.

There are observational evidences of the presence of magnetic fields in galaxy clusters [71]. Observations suggest existence of these fields on ∼Mpc scales with the field strength

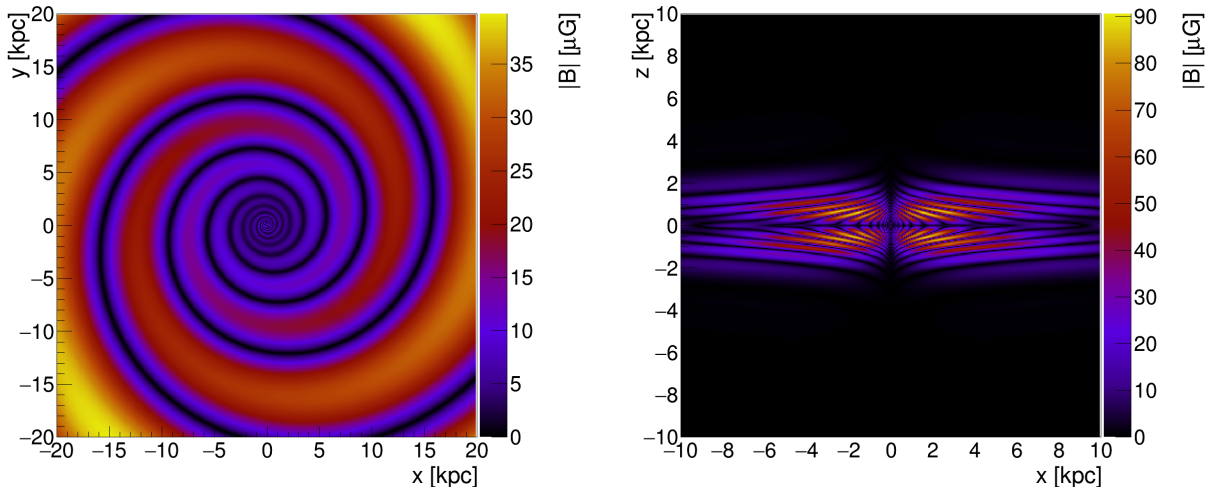

Figure 3.10: Same as Figure 3.7 but for the Dd1C1 variant of the TF17 model of the GMF. Figure taken from my publication [84].

in the orders of few μG [68]. Galaxy clusters are connected via filaments, where some measurements also suggest an existence of magnetic fields. Nevertheless, the strength of EGMF in the filament regions should be weaker compared to the galaxy cluster regions, approximately $0.1 - 10\,\mathrm{nG}$ [54]. Lower limits on the magnetisation in the void regions suggest $B > 10^{-16}$ G [85].

The extend of the extragalactic magnetic fields in the universe strongly depends on their origin. Generally, there are two categories of the theories of the EGMF origin. The first group of theories suggests an *astrophysical origin* of such fields. In such a case, the magnetic fields were created at low redshifts, therefore, the EGMF should be mostly confined within the galaxy clusters. Such fields might arise due to ejection of material by active galaxies or return currents created by charged cosmic rays [54]. On the other hand, *cosmological scenarios* suggest that strong seeds of the EGMF, referring to the initial sources that give rise to the formation and development of these magnetic fields, were created at large redshifts during early stages of the universe, such as the inflation period, or the electroweak or quantum chromodynamics phase transitions [54]. In this case, the EGMF should extend well beyond galaxy clusters into the overflows and even voids. These two mutually exclusive groups of theories of the origin of EGMF lead to very different outcomes for the influence on the propagation of extragalactic UHECRs.

There are multiple measurements that restrict the strength of the EGMF. The limits of the magnetic field strength B with respect to the coherence length l_c from different observations are depicted in Figure 3.11. The upper limit of the l_c comes from the Hubble horizon corresponding to the size of the observable universe. The lower limit on the l_c is given by magnetic diffusion causing the decay of the EGMF. The upper limits of the magnetic field strength are obtained from measurements of Zeeman splitting or the H I lines, giving the upper values in the orders of $\sim \mu$G. Other restrictions on the EGMF can be obtained from Faraday rotation measures, CMB anisotropies or cosmological scenarios

for magnetogenesis [54]. The existence of purely cosmological magnetic fields, that are not associated with any matter distribution, have not been observed. Strongest upper limits on the strength of such field is obtained from the measurements of CMB anisotropies suggesting values $B < 10^{-10}$ G [86] (depicted as "JS19" in Figure 3.11).

The deflection of a cosmic ray with charge Z in the EGMF can be estimated as [87,88]

$$\delta\theta_{EG} \simeq 0.15^\circ \left(\frac{D}{3.8\text{Mpc}} \cdot \frac{l_c}{100\text{kpc}}\right)^{\frac{1}{2}} \left(\frac{B_{EG}}{1\text{nG}} \cdot \frac{Z}{E_{100}}\right), \tag{3.15}$$

where D is the distance of the source, l_c and B_{EG} are the coherence length and the strength of the extragalactic magnetic field, respectively, and E_{100} is the energy of the particle in units of 100 EeV. This approximation of the total deflection is for a particle experiencing many small deflections in a turbulent magnetic field. Taking a coherence length of the extragalactic magnetic field 100 kpc and strength of 1 nG, a proton of energy 100 EeV originating in a close source at $D = 3.8$ Mpc would be deflected by $\sim 0.15^\circ$, while a proton with the same energy originating in a source at $D = 100$ Mpc would be deflected by $\sim 0.8^\circ$. However, heavier particles would experience larger deflections as the deflection angle $\delta\theta_{EG}$ scales with Z.

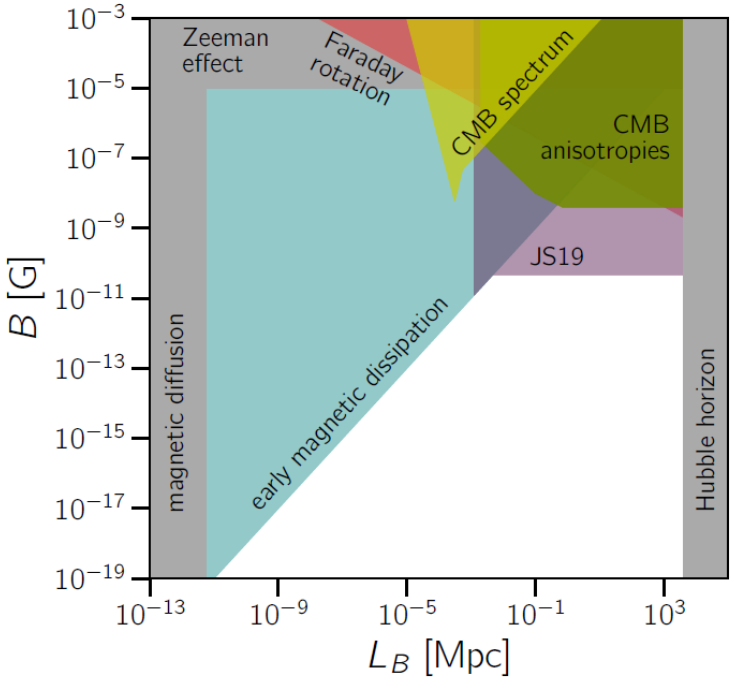

Figure 3.11: Exclusion regions of the strength of the EGMF B with respect to the correlation length L_B obtained from different measurements. Taken from [54].

Chapter 4

State of the art in the observations of ultra-high-energy cosmic rays

Over the last two decades, large-area observatories were able to measure properties of UHECRs with a previously unexpected precision. In this chapter, the most prominent results regarding the energy spectrum, mass composition and arrival directions of UHECRs are introduced with the main emphasis on the measurements at the Pierre Auger Observatory.

4.1 Energy spectrum

The energy spectrum of cosmic rays, depicted in Figure 4.1, extends over more than ten orders in magnitude of energy from $\sim 10^9$ eV over the aforementioned 10^{20} eV. The energy spectrum is steeply decreasing, following a power-law $dN/dE \propto E^{-\gamma}$ with the spectral index $\gamma \sim 2.7$. Nevertheless, there are features in the energy spectrum where the spectral index changes. These features of the energy spectrum of cosmic rays are of great scientific interest as they are imprints of the cosmic-ray origin and physics behind. At lower energies, the flux of the cosmic rays is quite high, with more than 1000 particles per square meter per second at GeV energies. However, cosmic rays at the highest energies are rather rare with flux of $\sim$ one particle per century per square kilometer at 10^{20} eV [89].

A steepening of the energy spectrum called the *knee* occurs around the energy $10^{15.5}$ eV, and was first reported in 1958 in [90]. It is followed by an additional steepening at the energy of $\sim 10^{17}$ eV [40], commonly referred to as the *second knee* or *iron knee*, reported in [91]. These features of the cosmic-ray energy spectrum are often explained as a transition region between the Galactic and extragalactic cosmic rays, although the true meaning of these two features is still under debate. Following the Peter's cycle [92], particles accelerated by a given source should achieve the same maximum rigidity, therefore the maximum energy of the particle then scales with its charge. Consequently, the transition region from Galactic to extragalactic cosmic rays for heavier nuclei would be at higher energies than for protons.

Above 10^{17} eV, the energy spectrum falls with the spectral index $\gamma \sim 3.3$ until the so

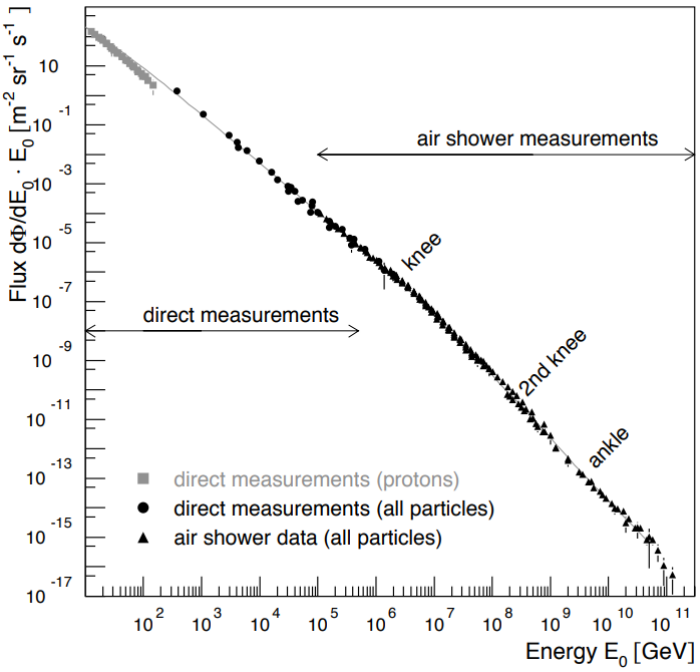

Figure 4.1: All-particle energy spectrum of cosmic rays. Taken from [89].

called *ankle* at the energy $\sim 5 \cdot 10^{18}$ eV where a hardening of the spectrum occurs and the spectral index changes to $\gamma \sim 2.5$ [40]. A new feature in the spectrum, *instep*, was reported in 2020 in [40] at the energy $\sim 1.4 \cdot 10^{19}$ eV where the spectrum steepens again to $\gamma \sim 3.05$.

Finally, there is a steep suppression of the energy spectrum at the energy $\sim 5 \cdot 10^{19}$ eV where the spectral index changes to $\gamma \sim 5.2$ [40]. Following the discovery of CMB [94], this suppression was independently described in 1966 by Greisen [64] and Zatsepin&Kuzmin [65] as a consequence of interactions of cosmic rays with CMB and is called the GZK cutoff. The GZK cutoff represents a theoretical energy limit for cosmic rays, stemming from energy losses, specifically due to photo-pion production and photodisintegration on CMB, and states that we should not observe cosmic rays (protons) with higher energies from far sources (above ~ 100 Mpc). However, it is still not clear whether the suppression is caused solely by the energy losses of cosmic rays or by reaching the maximum energy of particle acceleration around astrophysical sources in the nearby universe. The individual features of the energy spectrum can be seen in Figure 4.2 where the flux is multiplied by E^3 in order to highlight the changes in the spectral index.

Despite the great progress in the past years, the measurements of the energy spectrum of cosmic rays at the highest energies by the two largest current observatories, the Pierre Auger Observatory in the Southern hemisphere and the Telescope Array (TA) in the Northern hemisphere, do not perfectly agree [93,95,96]. The comparisons of the energy spectra measured by Auger and TA are depicted in Figure 4.3. The top left panel shows the

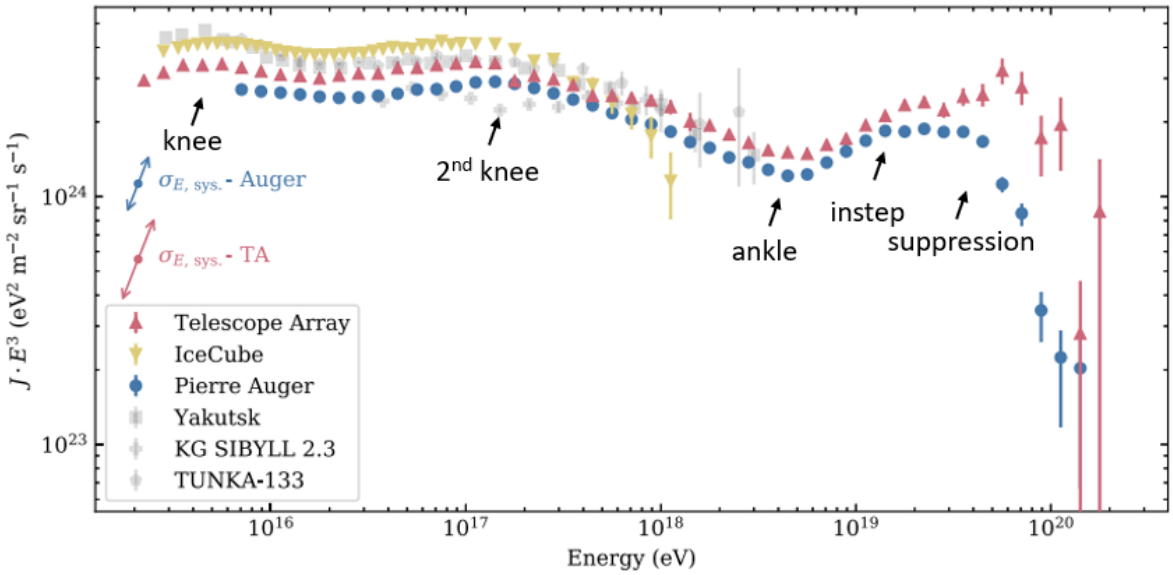

Figure 4.2: All-particle energy spectrum of ultra-high-energy cosmic rays as measured by multiple ground-based experiments. The flux is multiplied by E^3 to highlight the spectrum features. Modified from [93].

energy spectra measured in the full field of view of the two experiments. The two energy spectra align well up to few 10^{19} eV when an energy shift of $\pm 4.5\%$ is applied as can be seen in the top right panel. The reason for introducing such a shift is because the two experiments use different models for the fluorescence yield, and apply different corrections for aerosols and the invisible energy [93, 95, 96]. However, such a shift still does not align the two energy spectra at the highest energies. Comparison of the measured energy spectrum in a common declination band of the two observatories, between $-15.7°$ and $24.8°$, is shown in the bottom panels. The bottom left panel shows the two energy spectra in the common declination band shifted by $\pm 4.5\%$, which does not completely compensate for the differences between the two spectra at the highest energies. To align the spectra in the common declination band over the whole energy range, an energy-dependent shift of $\pm 10\% \times \log 10(\mathrm{E}/10^{19}\,\mathrm{eV})$ above 10^{19} eV needs to be applied, see the bottom right panel. Whether this disagreement of the measured spectra is caused by detector effects or is of an astrophysical origin is still under debate.

4.2 Mass composition

Another important information about the UHECRs is their mass. This information can be obtained only indirectly by measuring parameters of the air shower that are sensitive to the mass-composition of the primary particle. There are multiple mass-sensitive variables that are being applied in current observatories. Although these mass-sensitive parameters can

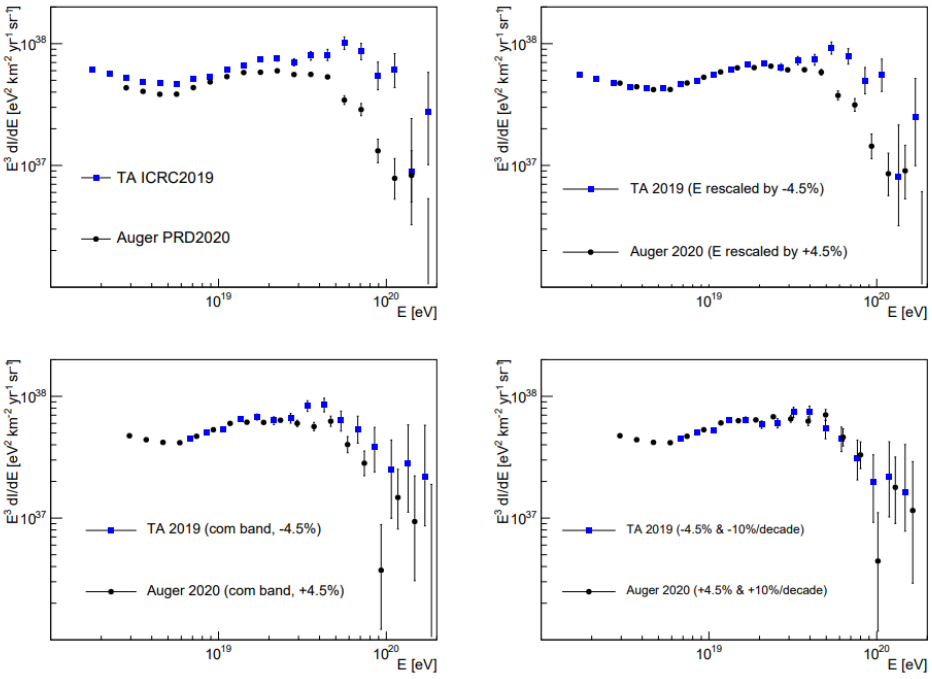

Figure 4.3: *Top:* The energy spectrum of cosmic rays measured by the Pierre Auger Observatory and Telescope Array in the full field of view (left) and the two spectra after rescaling the energy by ±4.5 % (right). *Bottom:* The energy spectrum measured by the Pierre Auger Observatory and Telescope Array in the common declination band, between −15.7° and 24.8°. The rescaling of energy by ±4.5 % (left) and the additional energy-dependent rescaling of $\pm 10\,\% \times \log 10(\mathrm{E}/10^{19}\,\mathrm{eV})$ above 10^{19} eV was applied. Taken from [95].

not distinguish the type of the primary particle on an event-by-event basis, the statistical distribution of such parameters still carries an important information.

The most prominent variable used as a mass-sensitive parameter is the depth of shower maximum X_{max} described in Section 1.2. The shower maximum is a statistical variable and the first and second moments of its distribution are mass-sensitive parameters frequently used in the community. While the shower maximum is a widely spread distribution for primary protons, for iron nuclei, the distribution of shower maxima is narrower with the mean being situated in the shallower depths in the atmosphere than for protons. The X_{max} can be very well observed by the fluorescence detectors. However, new techniques are being developed to reconstruct the X_{max} using surface detectors, which should greatly enhance the statistics and our knowledge about cosmic-ray mass composition in the future [97]. Another exciting new possibility is to use radio detectors for the determination of shower maximum, especially for inclined showers [98, 99].

The first and the second moments of X_{max} distribution as measured by multiple experiments are shown in Figure 4.4 together with the predicted values by three models of

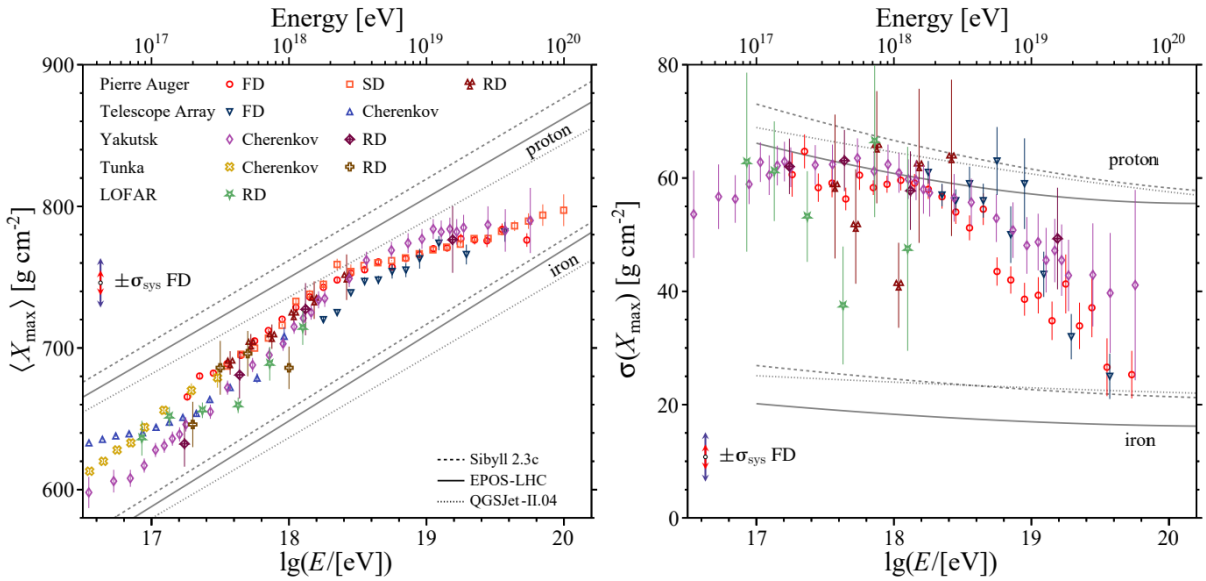

Figure 4.4: Energy evolution of the mean (left) and the variance (right) of the $X_{\max}$ distribution as measured by multiple experiments. Predictions by three models of hadronic interactions are shown for proton and iron nuclei. Taken from [93].

hadronic interactions. At the EeV energies, the mass composition of cosmic rays seems to be dominated by light particles (protons and helium nuclei). With the increasing energy, the mean of the shower maximum indicates a turn to heavier primaries. Similar tendency is seen with the second moment of the $X_{\max}$ in the left panel of Figure 4.4.

The mean and variance of the $X_{\max}$ distribution measured by the Pierre Auger Observatory can be interpreted using the mean and variance of $\ln A$ as can be seen in Figure 4.5 [100]. This transformation of the $X_{\max}$ moments into the $\ln A$ moments depends on the model of hadronic interactions used. Interpreting the data with EPOS-LHC and SIBYLL 2.3 shows a transition to heavier mass composition towards higher energies, up to the mean composition compatible with the mass of nitrogen nuclei in the last energy bin. Using QGSJETII-04, the predicted mean mass at the highest energies does not go much above the mass of helium nuclei. However, this model also leads to nonphysical values of $\sigma^2(\ln A)$ in a wide range of energy, as can be seen in the bottom middle panel of Figure 4.5.

Another evidence of a mixed composition for energies $(10^{18.5} - 10^{19.0})$ eV was found by the Pierre Auger Observatory using the correlation between the shower maximum and measured signal in surface detectors at 1000 m from the shower core [100, 101]. In case of the single-element scenario, such correlation coefficient r_G, the Gideon–Hollister correlation coefficient [102], should be positive or only slightly negative. Even in the scenario of a mixed composition of protons and helium nuclei the correlation coefficient found using the model predictions is positive. However, the measured value of the correlation factor in the energy range between $10^{18.5}$ eV and $10^{19.0}$ eV was reported to be significantly negative which strongly suggests a mixed composition with presence of particles with $A > 4$ (see

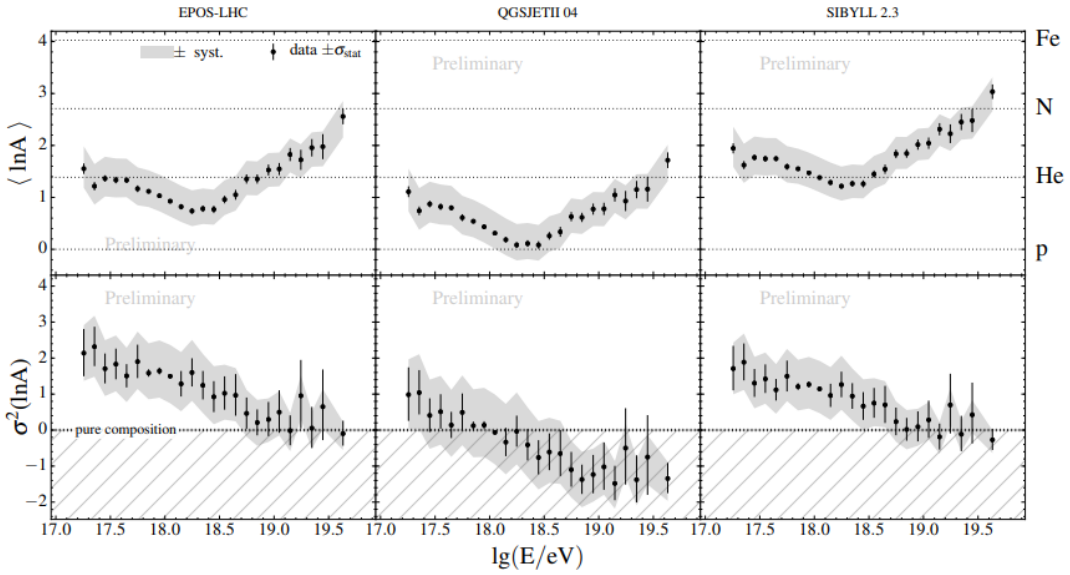

Figure 4.5: Energy evolution of the mean $\ln A$ (top) and variance of $\ln A$ (bottom) interpreted using the first two moments of $X_{\max}$ measured by the Pierre Auger Observatory for three models of hadronic interactions. From left to right: EPOS-LHC, QGSJETII-04 and SIBYLL 2.3. Taken from [100].

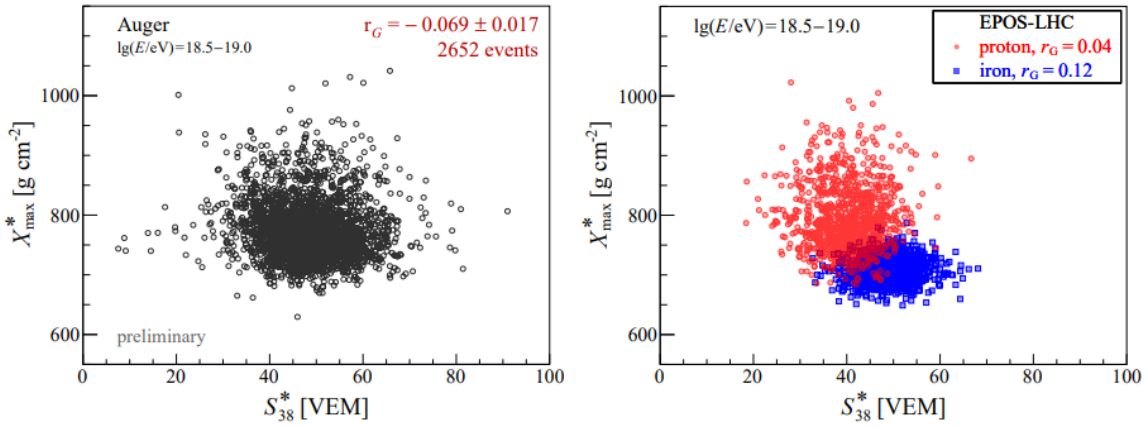

Figure 4.6: Correlation of the energy-corrected $X_{\max}$ and energy-corrected S_{38} of data measured by the Pierre Auger Observatory in the energy range from $10^{18.5}$ eV to 10^{19} eV (left) and for primary protons and iron nuclei predicted by air-shower simulations using EPOS-LHC (right). Taken from [100].

Figure 4.6).

There are multiple pieces of strong evidence suggesting that current models of the hadronic interactions do not describe the UHERC air-shower physics well [34]. Even heavier mass composition at the highest energies than reported above can be obtained using methods that assume ad-hoc modifications to the current models of hadronic interactions while significantly improving description of the measured data [103–105].

The measurement of the mass-sensitive parameters can be performed also by other techniques than the direct reconstruction of $X_{\max}$ from longitudinal profiles measured by FDs. One of such techniques, called the *delta method* utilises the rise time of the signals generated in the surface detectors [106]. Another approach of $X_{\max}$ estimation from signals induced in SDs is using deep neural network [107]. This method can achieve a resolution of $X_{\max}$ of 38 g/cm^2 for proton-induced showers at 10 EeV and a resolution better than 20 g/cm^2 for iron-induced showers at 20 EeV. The estimation of the $X_{\max}$ can be also obtained from SDs using the shower universality [16].

4.3 Arrival directions

An important information about the origin of ultra-high-energy cosmic rays is carried in their arrival directions. Even though the particles are deflected in magnetic fields during their propagation from the source to Earth and at low energies cosmic rays lose the directional information about their sources, at the highest energies, the deflections are smaller and by analysing their arrival directions we can learn about their possible sources. Both the Galactic and extragalactic magnetic fields can influence the trajectories of UHECRs. However, in case of few strong nearby sources or in the case of heterogeneous distribution of sources, large-scale and medium-scale anisotropies in the arrival directions of cosmic rays might arise on Earth helping us to identify their possible origin.

Large-scale anisotropy

The Pierre Auger Observatory published an important result about observing a large-scale dipole anisotropy in the arrival directions of cosmic rays with energies above 8 EeV [2] in 2017 with the statistical significance over 5.2σ. The updated distribution of arrival directions of cosmic rays with energies $E > 8$ EeV in the right ascension is shown in Figure 4.7 [108]. The measured data are fitted with the first and second harmonic functions. The corresponding amplitude of the first harmonic is $\sim 4.7\,\%$ with a probability of arising by chance from an isotropic distribution $\sim 3 \cdot 10^{-8}$. A three-dimensional dipole leads to the amplitude of $6.5^{+1.3}_{-0.9}\%$ with the dipole direction pointing towards the galactic longitude ℓ and latitude b of $(\ell, b) = (233^\circ, -13^\circ)$, and angular uncertainty of $\sim 15^\circ$. A distribution of the arrival directions of cosmic rays above 8 EeV smoothed by a 30° top-hat function is shown in Figure 4.8 in the galactic coordinates. The dipole direction is indicated by a cross and surrounded by the 1σ and 2σ confidence-level contours.

Since the dipole points far from the Galactic center ($\sim 125^\circ$), this result strongly

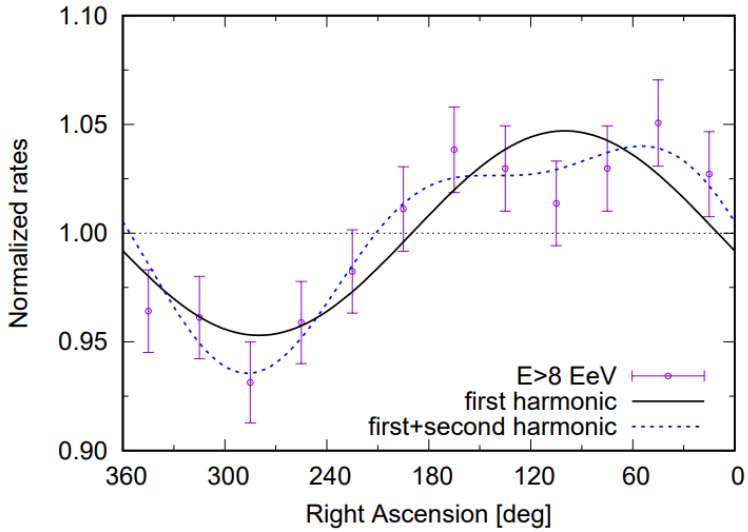

Figure 4.7: Relative rates of arrival directions of cosmic rays in the right ascension for energies above 8 EeV measured by the Pierre Auger Observatory. The first and the first+second harmonic obtained from the Fourier analysis is plotted in black and blue lines, respectively. Taken from [108].

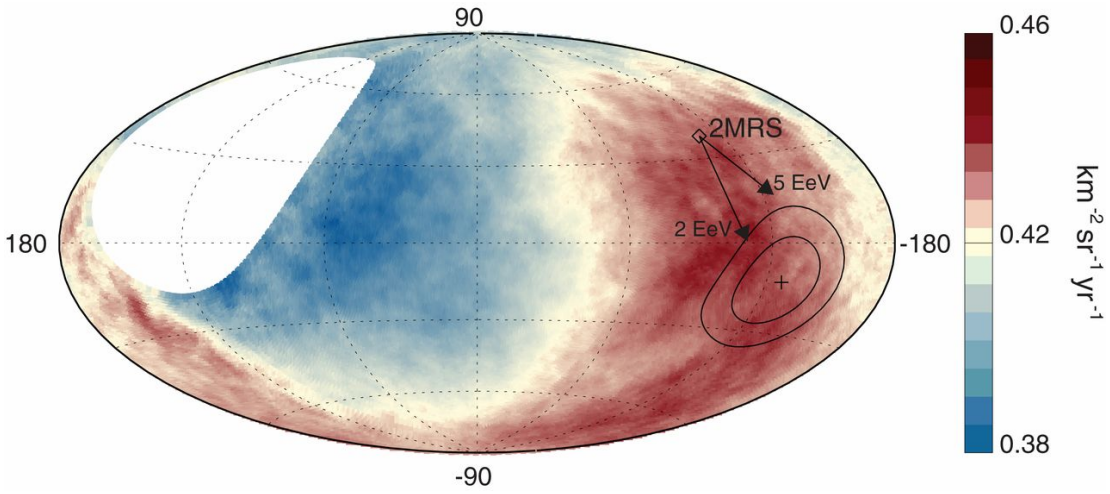

Figure 4.8: The flux of cosmic rays recorded by the Pierre Auger Observatory with energy above 8 EeV in galactic coordinates smoothed with a 45° top-hat function. The direction of the dipole is indicated by a cross together with the 1σ and 2σ confidence level regions. The direction of the 2MRS dipole is shown with diamond marker and the arrows represent the deflections of particles from 2MRS direction with rigidity 5 EeV and 2 EeV in the GMF. Taken from [2].

indicates that cosmic rays above 8 EeV are of an extragalactic origin. If these cosmic rays were mostly produced in the Milky Way, the dipole would be expected to have higher amplitude and to point towards the Galactic center or its close vicinity [108].

The same analysis was done for other energy intervals, namely, at lower energies from 4 EeV up to 8 EeV and at higher energies for three energy bins; (8-16) EeV, (16-32) EeV and ≥ 32 EeV [108]. The amplitude of the dipole in the right ascension is not significant in the low-energy bin $(4-8)$ EeV. The reconstructed amplitude in the right ascension is 0.5 % with p-value 0.6. The three-dimensional dipole reconstruction in this energy bin leads to an amplitude $2.5^{+1.0}_{-0.7}$% which is about three times weaker than in the case of energies above 8 EeV. In the case of the three energy bins with higher energies, a growing amplitude of the reconstructed dipole with energy was found. The amplitude with respect to the energy is shown in the left panel of Figure 4.9. The directions of the dipole in galactic coordinates for all energy bins are depicted in the right panel of Figure 4.9. All reconstructed dipole directions point towards similar area. However, no spatial evolution of the direction with energy can be clearly seen. Follow-up work analyzed the equatorial dipole amplitude using data covering more than three orders of magnitude in energy with $E \geq 0.03$ EeV [109]. While none of the reconstructed amplitudes below 8 EeV are significant, the directions of the reconstructed dipole for energies below 1 EeV point not far from the direction towards the Galactic center, thus suggesting a shift between the mostly Galactic cosmic rays and mostly extrgalactic cosmic rays somewhere between 1 EeV and few EeV.

Intermediate-scale anisotropies

Anisotropies at the intermediate angular scale[1] can show an association of the origin of UHECRs with a given type of astrophysical sources or one particular source. Searches for correlations of the arrival directions of cosmic rays with catalogues of sources are being performed mainly for two types of galaxies; starburst galaxies (SBGs) and active galactic nuclei (AGNs), as well as blind searches for overdensities in the arrival directions of cosmic rays [110–113].

Latest results of the blind searches for excess of cosmic rays performed by the Pierre Auger collaboration were presented in [112]. The number of detected particles within a window of a given radius on the sky is compared with the expectations from isotropic distribution over the whole field of view of the Observatory which covers $\sim 85\%$ of the whole sky. The radius of such a window is ranged between 1° and 30° and the lower threshold of the energy is varied from 32 EeV to 80 EeV. The most significant excess is found at galactic coordinates $(\ell, b) = (305.4^\circ, 16.2^\circ)$ for events above 41 EeV and top-hat smoothing of radius 24° [112]. A total of 153 events were observed in this region compared to 97.7 expected from isotropy. The sky map of local Li-Ma significance for this search is shown in the left panel of Figure 4.10 in the galactic coordinates.

A search for intermediate-scale anisotropies in the Telescope Array data shows an excess, called a *hot-spot*, in the arrival directions of cosmic rays with energies above 57 EeV

[1]Intermediate anisotropies are at the angular scale larger than $\sim 1^\circ$ and smaller than $\sim 45^\circ$, this definition follows Reference [110].

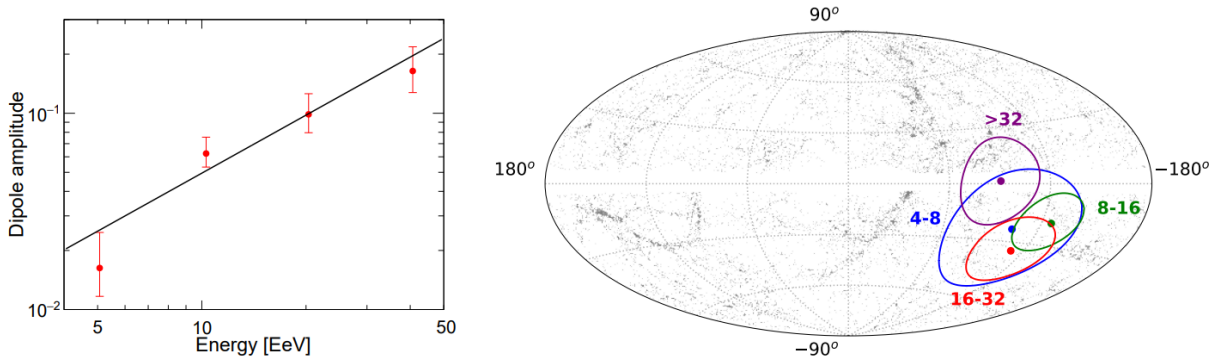

Figure 4.9: *Left:* Evolution of the three-dimensional dipole amplitude with energy as measured by the Pierre Auger Observatory. *Right:* Reconstructed direction in galactic coordinates of the three-dimensional dipole for individual energy bins in EeV. Taken from [114].

at a position $(\alpha, \delta) = (144.3°, 40.3°)$ in equatorial coordinates, see the right panel of Figure 4.10. The published results in [113] show a statistics from 12-year data set and in the 20° region around the hot-spot position. In total, 40 events were detected, while the expected number from the isotropic distribution is 14.6. The local significance of this hot-spot was estimated as 3.2σ. The hot-spot seen by the Telescope Array is close to the supergalactic plane, which contains multiple local galaxy clusters including the Ursa Major cluster, the Virgo cluster and the Coma cluster. To determine the origin of this hot-spot, a better understanding of the mass composition of these events together with more detailed models of the Galactic and extragalactic magnetic fields are needed.

Correlations of the arrival directions of cosmic rays measured by the Pierre Auger Observatory with galaxy catalogues have been presented in [110,112]. The arrival directions of cosmic rays are compared to the flux patterns expected from the catalogs based on the likelihood-ratio analysis. The explored catalogues are the large-scale distribution of matter based on the Two Micron All-Sky Survey, catalogue of starburst galaxies and the catalogue of AGNs observed in hard X-rays with Swift-BAT and jetted AGNs from the Fermi-LAT 3FHL catalogue. The lower energy threshold of cosmic rays is varied from 32 EeV up to 80 EeV. The maximum test statistic (TS) is found in two regions, first around energy $\sim$ 40 EeV and the second one above the energy $\sim$ 60 EeV. The largest test statistic is obtained for correlation with the starburst galaxies with $TS = 25$ for threshold energy 38 EeV and post trial p-value $3.2 \cdot 10^{-5}$. The highest test statistic for the all-galaxies catalogue, AGNs and jetted AGNs is 18.0, 19.4 and 17.9, respectively. Even though the current analyses are not able to select a preferred catalogue of sources due to low statistics, the correlations found are an important result suggesting an anisotropic distribution of the arrival directions of cosmic rays at the intermediate angular scales.

The flux patterns expected from the aforementioned four catalogues exhibit a strong excess patters in a similar region. This region is located in the direction of the Centaurus A

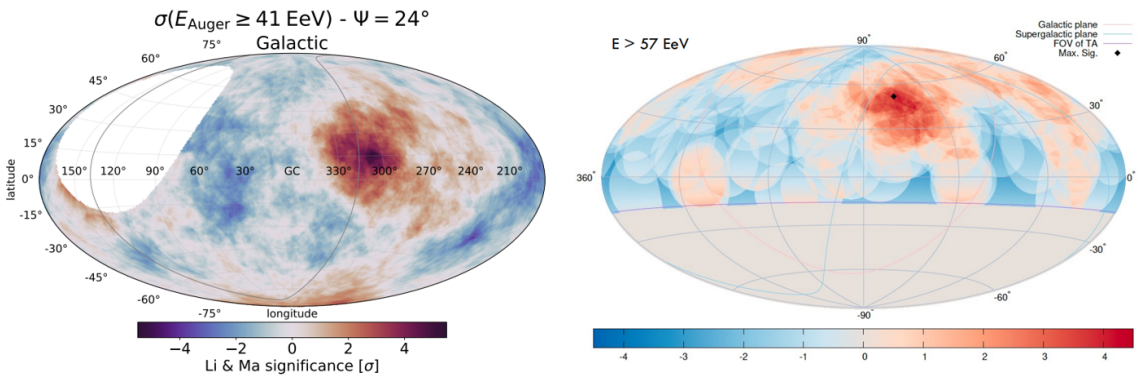

Figure 4.10: *Left:* The Li-Ma significance map in galactic coordinates for the blind search in arrival directions of cosmic rays above 41 EeV measured by the Pierre Auger Observatory with top-hat smoothing with radius 24° [112]. *Right:* Scaled distribution of arrival directions of cosmic rays with energies $E > 57$ EeV in equatorial coordinates measured by Telescope Array. The colour scheme represents an excess or a deficit of the cosmic ray flux with respect to the isotropic expectations. Black marker shows the location of the center of the hot spot. Taken from [113].

or NGC 4945. Centaurus A is a radio galaxy located ~ 3.7 Mpc from Earth and NGC 4945 is a Seyfert galaxy with distance ~ 3.6 Mpc. The most significant excess found in the blind search in the Pierre Auger Observatory data is located 2.9° from the NGC 4945 and 5.1° from Centaurus A. A targeted search of correlation of arrival directions of cosmic rays with the direction of Centaurus A leads to a post-trial significance of 3.9σ for energies above 38 EeV using the top-hat smoothing with radius 27°. This corresponds to a total of 215 observed events from this region compared to 152 events expected from an isotropic distribution. With a distance of only ~ 3.7 Mpc in coordinates $(\ell, b) = (309.5°, 19.4°)$ Centaurus A is one of the most discussed candidate source of UHECRs.

Cosmic rays above 100 EeV

The arrival directions of cosmic rays with energies above 100 EeV in equatorial coordinates recorded by the Pierre Auger Observatory and Telescope Array are shown in Figure 4.11. Although a clustering of some events can be seen, there is no apparent correlation with nearby source candidates. This might be caused by the rather heavy mass composition at the highest energies that causes larger deflections of the particles in the GMF and EGMF than would be expected for protons or light mass composition.

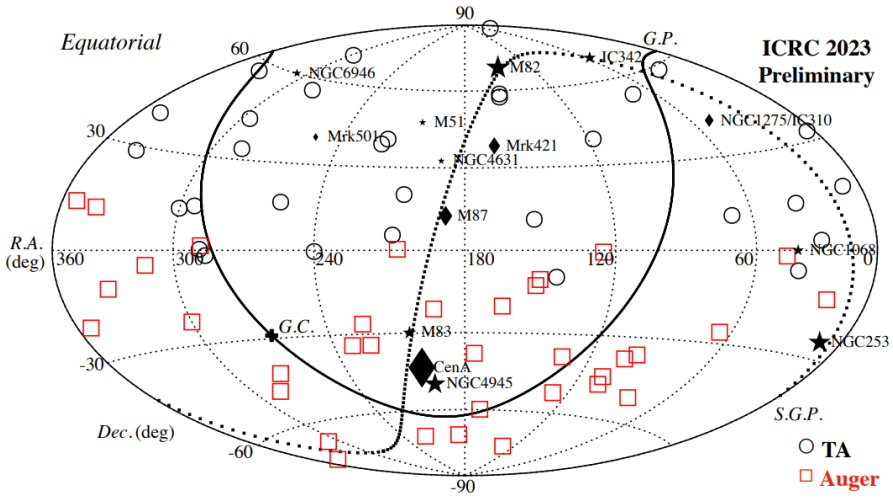

Figure 4.11: The arrival directions of cosmic rays with energy above 100 EeV recorded by the Pierre Auger Observatory and Telescope Array together with nearby astronomical source candidates. The plot is in equatorial coordinates. Taken from [115].

Chapter 5

Influence of the Galactic magnetic field on dipole anisotropy in arrival directions of ultra-high-energy cosmic rays

This research topic is motivated by the observation of the dipole anisotropy in arrival directions of cosmic rays above 8 EeV first reported by the Pierre Auger collaboration in [2], see Section 4.3. The direction and the amplitude of this dipole suggest an extragalactic origin of UHECRs. The direction of the dipole points approximately 125° away from the Galactic center, which is more than expected from the deflections in the current models of the GMF if these particles were of a Galactic origin. Moreover, in case of the Galactic origin, the amplitude of a dipole is expected to be larger than the observed one. Observation of the dipole anisotropy in arrival directions also indicates an anisotropic distribution of extragalactic sources of UHECRs because, according to Liouville's theorem, an anisotropic distribution of arrival directions of cosmic rays can not arise from an originally isotropic distribution [116].

Cosmic rays are influenced by the GMF during their propagation within the Galaxy on their journey to Earth (see Chapter 3). The GMF causes deflections of the cosmic-ray particles that depend on their charge Z and energy E and the properties of the magnetic field they are crossing. Therefore, the measured direction of the dipole anisotropy on Earth does not need to correspond to the direction of the anisotropy outside the Galaxy since the GMF can shift the dipole direction. Moreover, the amplitude of the dipole might be modified during the propagation, therefore, the amplitude of the extragalactic anisotropy does not need to correspond to the measured one. Especially at low rigidities, the GMF tends to smear the anisotropies and isotropises the cosmic-ray flux.

Monte Carlo simulations of cosmic-ray propagation in multiple models of the GMF are utilised in this work in order to investigate the influence of the GMF on the dipole anisotropy observed on Earth. A dipole anisotropy of cosmic-ray flux arriving at the edge of the Galaxy is assumed, hereafter called as the *extragalactic dipole*. Various mass-

composition mixes of the cosmic-ray flux above 8 EeV are investigated. The goal of this study is to investigate possible features of the extragalactic dipole, including its direction and amplitude, that is compatible with the measured dipole on Earth after propagation in the GMF.

The influence of the GMF on the dipole anisotropy and possible directions of the extragalactic dipole were studied by the author of this thesis and previously presented in [84, 117, 118]. This chapter is mainly based on the published results [84] and introduces some specifics of this study in more detail.

The simulations of cosmic-ray propagation are described in Section 5.1. The reweighting process of the simulated particles and the reconstruction of the dipole is presented in Section 5.2. Influence of the GMF on the dipole amplitude and direction without any constrains on the measured dipole on Earth is described in Section 5.3 and the results presenting the possible directions of the extragalactic dipole for single-element scenario and for the mixed mass composition are presented in Section 5.4. The dipole at lower energies, between 4 EeV and 8 EeV and its connection to the dipole above 8 EeV is discussed in Section 5.5. Cross-checks of the obtained results are described in Section 5.6 followed by the discussion of the obtained results in Section 5.7.

5.1 Simulating the cosmic-ray propagation

Cosmic-ray propagation in the GMF is simulated with the CRPropa 3 (version 3.1.7) [83]. Particles are propagated within the Galaxy, which is defined as a sphere of radius 20 kpc with Galactic center in the center of coordinates at $(x, y, z) = (0, 0, 0)$ kpc. The position of the observer is set to coordinates $(x, y, z) = (-8.5, 0, 0)$ kpc corresponding approximately to the location of Solar system in the Milky Way.

5.1.1 Propagation in the Galaxy

Generally, for simulations of propagation of cosmic rays in the GMF, two techniques can be implemented. The first technique is *direct tracking* of particles propagating in the Galaxy towards an observer inside the volume of the Galaxy. In this case, the observer needs to be large enough (usually ≥ 100 pc) in order to collect sufficient statistics of the particles reaching it. The probability that a particle hits the observer is decreasing when reducing the size of the observer. Therefore, this technique can be demanding on the CPU time as vast majority of the particles never reach the observer and are disregarded from the simulation. The second possibility of simulating particle propagation within the Galaxy is the so-called *backtracking*. Using the backtracking technique, the observer serves as a point-like source of anti-particles that are being propagated in the GMF. In this scenario, no particles are lost in the simulation and much larger statistics can be obtained in very short time. By exchanging the anti-particles to particles and flipping the momentum of the particle, according to time-charge invariance this backtracking technique is compatible with tracing the particles coming from the opposite direction [83, 119]. However, this

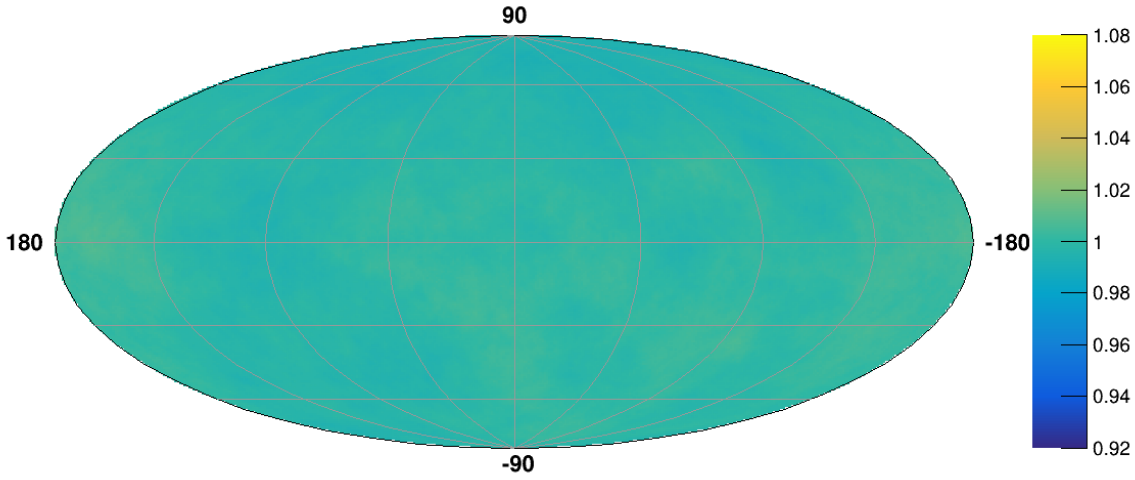

Figure 5.1: Distribution of the arrival directions on Earth in of protons with energy 10^{19} eV in galactic coordinates smoothed by a 45° top-hat function. Particles were propagated in the JF12Planck model of GMF.

technique can not be applied when energy losses of cosmic rays (see Chapter 3) have to be taken into account. For propagation of cosmic rays above 8 EeV from the edge of the Galaxy to an observer on Earth, the energy losses can be neglected as the mean free path of the individual interactions is much larger than the propagation distances travelled by the particles within the Galaxy [55]. Even for iron nuclei, the trajectory length did not exceed 500 kpc in our simulations.

In order to simulate an isotropic flux of extragalactic cosmic rays arriving on Earth using the backtracking method, an isotropic flux of cosmic rays with opposite charge can be simulated from the point like observer. After inverting the charge and momentum, the simulated flux corresponds to an isotropic flux of cosmic rays entering the Galaxy and reaching the observer. Note, that the distribution of these cosmic rays creating an isotropic flux on the observer is not isotropic at the edge of the Galaxy, since these are only the cosmic rays reaching Earth. The reason for that is that not all the trajectories are equally probable to reach Earth and flux from some extragalactic directions is magnified while from other directions the flux might be demagnified. These magnification patters depend on the model of the GMF applied in the simulation and the rigidity of the particles.

An illustration of this effect is shown in Figure 5.1 and Figure 5.2 for protons of energy 10^{19} eV propagated in the JF12Planck model of the GMF. While Figure 5.1 shows the distribution of the arrival directions of protons on Earth that is isotropic within statistical fluctuations in the scale of few tenths of a percent, Figure 5.2 shows a map of arrival directions of the same particles at the edge of the Galaxy. The sky maps are in galactic coordinates and the colour represents the relative number of particles with arrival directions

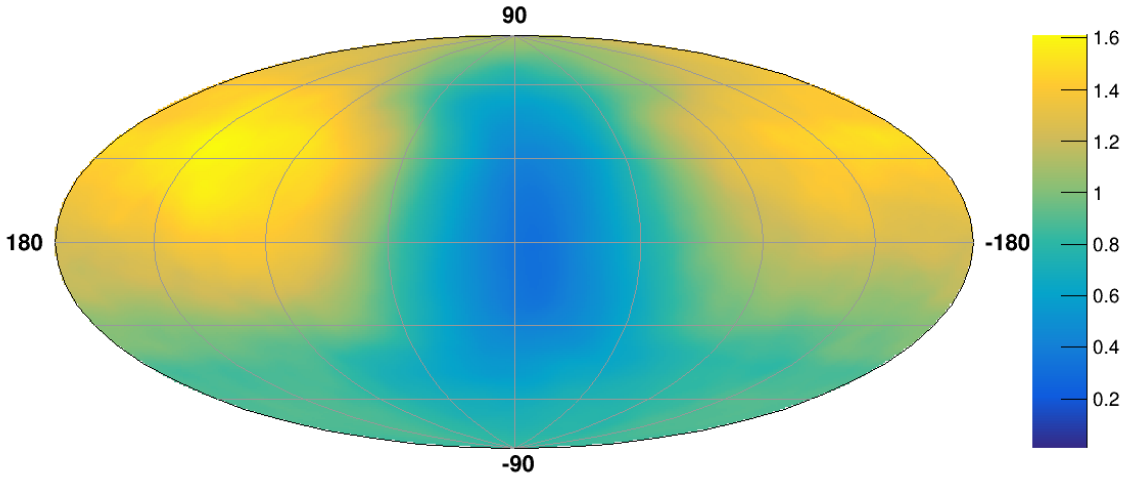

Figure 5.2: Same as Figure 5.1 but at the edge of the Galaxy. The simulation set of particles is the same one.

in a given spatial bin. The maps are smoothed with a top-hat function with 25° radius. This example shows that for a given model of the GMF and given rigidity of particles, cosmic rays originating in the vicinity of the direction of the Galactic center are less likely to reach Earth compared to other directions. Moreover, trajectories with initial direction in positive latitudes are generally also more likely to reach Earth than cosmic rays originating in the directions with negative latitudes.

In this study, the backtracking method is applied[1]. (Anti)particles are backtracked from an isotropically emitting source in coordinates $(x, y, z) = (-8.5, 0, 0)$ kpc and they are collected at the edge of the Galaxy. The start and end coordinates of the particle, as well as its start and end momentum are saved. A condition on the maximum trajectory length was applied in the simulations, requesting that the total trajectory length travelled by a cosmic ray is smaller than 500 kpc. However, no particles were rejected by this criterion.

5.1.2 Energy spectrum and particle species

An isotropic flux of cosmic rays is simulated separately for four types of cosmic-ray species; protons (^{1}H), helium (^{4}He), nitrogen (^{14}N), and iron (^{56}Fe) nuclei. For each element, a total of 250,000 particles is simulated[2].

[1]The results that were previously presented in [117, 118] were obtained using the direct tracking technique. The direct tracking and backtracking approach was compared and the results are compatible within statistical errors.

[2]For comparison, the dipole anisotropy in arrival directions of cosmic rays above 8 EeV reconstructed from data measured by the Pierre Auger Observatory is based on $\sim 32,000$ events [2].

The particles are simulated in the energy range from 8 EeV up to 100 EeV. The energy spectrum is a power law $\mathrm{d}N/\mathrm{d}E \propto E^{-\gamma}$ with the spectral index $\gamma = 3$. This spectral index was chosen as a close approximation of the spectral index of cosmic rays above 8 EeV [40]. Note that the obtained results were also checked for spectral indices 2.5 and 3.5 (see Section 5.6).

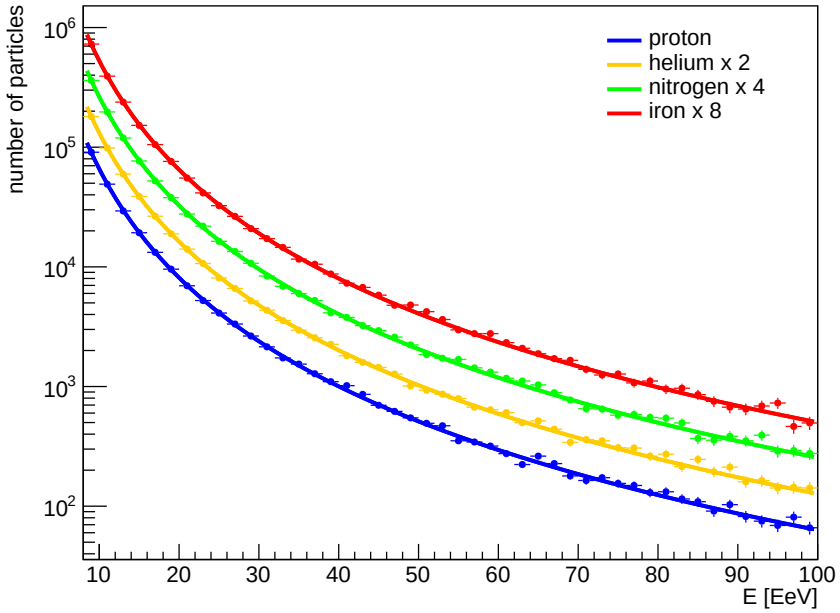

Figure 5.3: Energy spectrum of the simulated cosmic rays for the four particle species after the propagation in the JF12Planck model of the GMF. For better comparison, the flux of helium, nitrogen and iron nuclei is multiplied by 2, 4 and 8, respectively.

Since the energy losses of cosmic rays are not taken into account and due to the back-tracking method of cosmic-ray propagation no particles are lost, the energy spectrum of cosmic rays after the propagation in the GMF remains unchanged. The energy spectrum of the four particle species propagated in the JF12Planck field of the GMF is depicted in Figure 5.3 and fitted by

$$\frac{\mathrm{d}N}{\mathrm{d}E} = AE^{-\gamma}. \tag{5.1}$$

The results of the fitted parameters of the energy spectra for the four elements are shown in Table 5.1.

5.1.3 Models of the Galactic magnetic field

The particles were propagated within the Galaxy in multiple models of the GMF. The first model is the JF12Planck model of the GMF [82] that is based on the JF12 model of the

	A [-]	γ [-]
H	$(6.82 \pm 0.08) \cdot 10^7$	3.01 ± 0.01
He	$(6.80 \pm 0.08) \cdot 10^7$	3.01 ± 0.01
N	$(6.77 \pm 0.08) \cdot 10^7$	3.01 ± 0.01
Fe	$(6.81 \pm 0.08) \cdot 10^7$	3.01 ± 0.01

Table 5.1: The results of the energy spectrum fit of the individual simulated particle elements for one realisation of the JF12Planck model of the GMF. The A parameter is the scaling factor of the function (5.1) and γ is the fitted spectral index. In the plot, the energy spectrum of the individual elements is scaled by a factor of 2, 4 and 8 for He, N and Fe, respectively.

GMF [75, 80] with adjusted parameters to fit the measurements by the Planck mission. For description of the model see Section 3.2.1. To account for the uncertainties of the GMF model, multiple realisations of the field were simulated. Three coherence lengths l_c of the turbulent component of the field were simulated; 30 pc, 60 pc and 100 pc. Lowering the coherence length acts in a similar manner as decreasing the overall strength of the field [120]. For each coherence length, multiple realisations of the field were simulated with different seeds of the random field. The turbulent field of the JF12Planck model of the GMF is modeled within CRPropa 3 as Kolmogorov-type turbulent magnetic field [83]. The JF12Planck model was used in superposition with the model of the magnetic field in the central mass zone of the Galaxy [121, 122]. The latter implements the field up to 3 kpc from the Galactic center as the JF12 model does not implement any field in this central region. In the following text, the presented results for the JF12Planck field are taken as a sum of the different realisations of the field, unless stated otherwise.

For comparison, particles are also propagated in the TF17 model of the GMF. The TF17 model composes of various combinations of multiple disk and halo fields (see Section 3.2.1). For the purpose of this work we use combinations of three different models of the disk field (Ad1, Bd1, Dd1) together with a bisymmetric model of the halo field (C1). These combinations lead to the best fitted observational values and are able to reproduce the X-shape behavior in the polarised light [78]. There are no random components in this model of the GMF, therefore, only one realisation of the particle propagation is performed for each of the three options of the TF17 model of the GMF.

5.2 Reconstruction of the dipole in arrival directions

The generated simulations correspond to an isotropic flux of particles entering the Galaxy and reaching Earth. Based on the observation of the large-scale dipole in arrival directions of cosmic rays measured by the Pierre Auger Observatory, we assume a dipole distribution of particles entering the Galaxy as well. In order to achieve such distribution, the simulated particles are reweighted according to the travel direction of cosmic rays at the edge of the Galaxy as

$$w = A_0 \cos\delta + 1, \tag{5.2}$$

where A_0 is the amplitude of the extragalactic dipole and δ is the angular distance between the direction of the initial momentum of the particle and that of the imposed extragalactic dipole direction. With such reweighting, the amplitude is expressed in the means of a percentage of the relative excess with respect to the mean flux. The extragalactic amplitudes of the dipole are investigated in the range from 6.5% up to 20% in discrete steps of 2% (the first step is 1.5 from the amplitude 6.5% to 8%). The GMF can influence the amplitude of the dipole after propagation to the observer. Generally, the extragalactic amplitude A_0 should be equal or higher than the amplitude on the observer on Earth, $A_{\rm obs}$, due to the effect of isotropisation of the cosmic-ray flux in the GMF. We explore the possible directions of the extragalactic dipole by imposing the weights into the particle flux in all possible extragalactic directions of the dipole with a step of 1° in longitude and 1° in latitude.

To reconstruct the three-dimensional direction and amplitude of the dipole on the observer level, a reconstruction procedure from [123] was used. Discrete versions of the zeroth and first moments of the flux on the observer are calculated as

$$S_0 = \sum_k \frac{1}{w_k} \quad \text{and} \quad \mathbf{S} = \sum_{\rm k} \frac{\mathbf{u}_{\rm k}}{{\rm w}_{\rm k}}, \tag{5.3}$$

where the sums go over all particles k reaching the observer with the weight w_k. $\mathbf{u}_k$ is the vector of their arrival direction to the observer. The amplitude $A_{\rm obs}$ and the direction $\mathbf{D}_{\rm obs}$ of the dipole on the observer then can be calculated as

$$A_{\rm obs} = 3\frac{\|\mathbf{S}\|}{S_0} \quad \text{and} \quad \mathbf{D}_{\rm obs} = \frac{\mathbf{S}}{\|\mathbf{S}\|}. \tag{5.4}$$

The parameters of the dipole in the right ascension and the three-dimensional dipole are calculated for the single-particle species for the different initial amplitudes A_0 and all the extragalactic directions of the dipole in latitude and longitude in a grid of $1° \times 1°$.

In case of a mixed composition, for simplification, we assume that the abundance of individual elements remains the same in the whole energy range (due to the steeply falling energy spectrum, the dominant contribution to the large-scale anisotropy comes from the energies just above 8 EeV). The dipole properties for a mixed composition of cosmic rays are obtained by combining the dipoles calculated for the single species with weights corresponding to the fraction of a given element in the the all-particle mix (for the derivation of the dipole amplitude for multi-particle mix see Appendix A). Since we are not assuming any restrictions on the mass composition, we mix the four particle species with a step in relative fractions of 5%, going from the lightest, pure proton, to the heaviest, pure iron, composition.

5.3 Constraints on the extragalactic dipole

The influence of the GMF on the amplitude and direction of the dipole are presented in this section and the differences of the predictions between individual models of the GMF are shown.

5.3.1 Change of the dipole amplitude

The amplitude of a dipole flux of cosmic rays entering the Galaxy A_0 does not need to be equal to the amplitude of the dipole flux observed on Earth $A_{\rm obs}$ due to the diffusive propagation of cosmic rays in the GMF. The effects of the GMF on the dipole amplitude were also examined in [124]. The level of the decrease of the amplitude depends strongly on the rigidity of the particles and the direction of the dipole. It is also important to note that different predictions of the decrease of the amplitude arise when considering different models of the GMF.

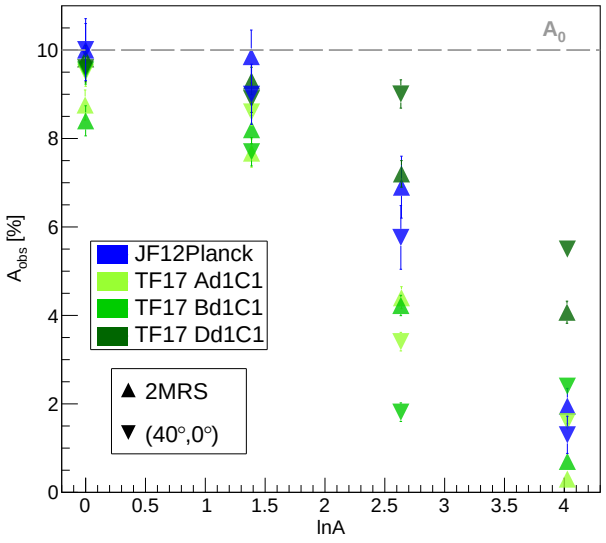

Figure 5.4: Reconstructed dipole amplitude on the observer for particles of energies above 8 EeV with mass A propagated in the TF17 (green) and the JF12Planck (blue) models of the GMF. The imposed dipole amplitude (A_0) is 10% for two extragalactic directions of the dipole; The example direction was chosen to the 2MRS [125] dipole in coordinates $(l_0, b_0) = (251°, 37°)$ and the direction $(l_0, b_0) = (40°, 0°)$. The error bars represent 1σ certainty levels. Figure taken from my publication [84].

The change of the amplitude for different cosmic-ray species and two different directions of the extragalactic dipole are depicted in Figure 5.4 for cosmic rays propagated in the JF12Planck and the three options of the TF17 model of the GMF. The simulated energy spectrum is the same for all elements, from 8 EeV up to 100 EeV with the spectral

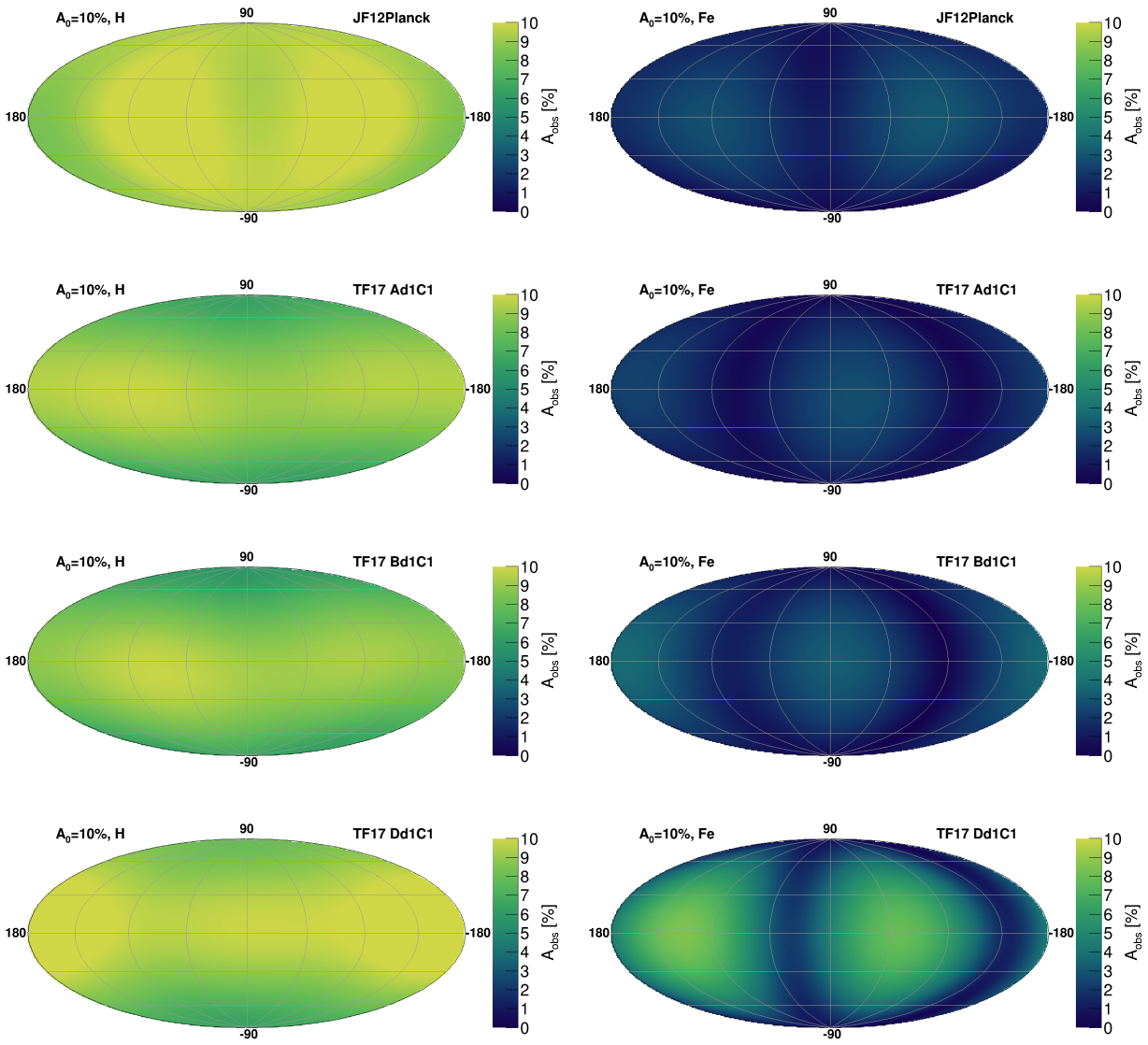

Figure 5.5: Sky maps in galactic coordinates of extragalactic dipole directions with initial amplitude of $A_0 = 10\%$ for protons (left) and iron nuclei (right) of energies above 8 EeV. The colour scale corresponds to the amplitude of the dipole on the observer after propagation in the JF12Planck with $l_c = 60$ pc, Ad1C1, Bd1C1, and Dd1C1 option of the TF17 model of the GMF from top to bottom, respectively. Figures for JF12Planck and TF17 Bd1C1 taken from my publication [84].

index $\gamma = 3$. Therefore the rigidity of the cosmic-ray flux decreases with increasing atomic number. The imposed extragalactic amplitude is $A_0 = 10\%$. One of the imposed directions corresponds to the 2MRS dipole direction [125]. The second direction, $(l_0, b_0) = (40°, 0°)$, is chosen randomly in order to demonstrate the different behavior of the amplitude suppression and it does not correspond to any significant astrophysical system. The decrease of the amplitude is evolving with the atomic number for all models of the GMF. A minimal suppression of the amplitude is found for pure proton scenario, while for pure iron nuclei the originally dipole flux can be almost completely isotropised during the propagation, with the exception of the TF17 Dd1C1 option of the GMF model where the amplitude remains above 4% for both directions of the dipole. The large differences between predictions of the decrease of amplitude are visible especially in the case of nitrogen nuclei scenario for extragalactic dipole in the direction $(l_0, b_0) = (40°, 0°)$. The Dd1C1 option of the TF17 model of the GMF shows an amplitude on the observer of $\sim 9\%$, while the Bd1C1 model shows a suppression of the amplitude down to lower than $\sim 2\%$.

The change of the amplitude for all the possible extragalactic directions of the dipole is visualised in Figure 5.5 for the individual models of the GMF and two particle species, protons and iron nuclei. In case of the JF12Planck model of the GMF, the sky map is constructed from simulations of cosmic-ray propagation in one realisation of the field with the coherence length of 60 pc. The sky maps represent the sky above the observer in galactic coordinates and each point corresponds to an extragalactic direction of the imposed dipole. The colour shows the amplitude of the dipole on the observer $A_{\rm obs}$ for a given extragalactic direction of the dipole. The initial extragalactic dipole amplitude is $A_0 = 10\%$ for all cases.

The minimal suppression of the amplitude is found in two extended lobes around longitudes of $\sim \pm 90°$ for both protons and iron nuclei in case of the JF12Planck model of the GMF, see Figure 5.5 (top). In case of pure protons, the lowest amplitude reconstructed on the observer is found to be $\sim 8\%$, while for iron nuclei the arrival directions can get completely isotropised during the propagation in the GMF and the flux is then compatible with an isotropic distribution. Similar suppression of the amplitudes is found for other realisations of the JF12Planck field.

In case of the TF17 model of the GMF, a minimal suppression of the amplitude is found in directions close to the Galactic plane for pure proton scenario. Since the Dd1C1 option of the TF17 field has the lowest strength of the magnetic field from the three TF17 options, the suppression of the amplitude is smaller than for the Ad1C1 and Bd1C1 options. The maximal suppression from the initial amplitude $A_0 = 10\%$ is down to $\sim 6\%$ for protons in the Bd1C1 field. Different suppression patterns are found in case of pure iron nuclei, where minimal suppression is found in directions towards and opposite the Galactic center for the Ad1C1 and Bd1C1 options of the TF17. The Dd1C1 option of the TF17 model suggests similar suppression pattern as the JF12Planck model, however, with weaker suppression of the amplitude. Complete isotropisation of arrival directions can also be observed in certain directions of the extragalactic dipole when considering iron nuclei propagated in the TF17 model of the GMF as well.

5.3.2 Shift of the dipole direction

In addition to the attenuation of the dipole amplitude after propagation in the GMF, the direction of the dipole can be modified as well. Similarly to the previous case, the shift of the dipole direction[3] depends on the model of the GMF used, rigidity of the particles and the extragalactic direction of the dipole. Minor shifts of the dipole are possible in orders of few degrees. However, the shift can be as high as $\sim 180^\circ$ for some directions of the dipole and low rigidity of particles.

The shifts of the dipole direction for protons and iron nuclei are visualised in Figure 5.6 for the individual models of the GMF. The sky maps represent the sky above the observer in galactic coordinates and each point represents the extragalactic direction of the dipole. The colour shows the size of the angular shift of the dipole between the extragalactic direction and the direction of the dipole on the observer after propagation in a given model of the GMF. Again, the sky maps for the JF12Planck model of the GMF are shown for one realisation of the field with the coherence length $l_c = 60$ pc. In order to better visualise the shift for different primary particles, different scales are used for protons and iron nuclei.

The maximum shift of the dipole in case of protons is found to be $\sim 15^\circ$ using the JF12Planck model and $\sim 18^\circ$ for the TF17 model. In case of iron nuclei, the dipole shift can be much higher than in the case of protons going up to the aforementioned 180°. The patterns of the dipole shift are strongly dependent on the model of the GMF used. The most similar prediction of the dipole shift are for the Ad1C1 and Bd1C1 options of the TF17 field for both protons and iron nuclei.

5.4 Properties of the extralactic dipole compatible with measurements

To compare the reconstructed dipoles obtained from the simulations and the measurement of the dipole anisotropy in the arrival directions of cosmic rays above 8 EeV by the Pierre Auger Observatory [2], both the direction of the dipole and the amplitude of the dipole are taken into account. We explore all possible mass-composition mixes of the four primary particles and mix them with a step of 5% in relative fractions, including single-component scenarios of p, He, N and Fe. No cuts are applied on the mass composition since the mass composition of cosmic rays is not known precisely enough, as discussed in Section 4.2.

The direction and amplitude of the dipole on the observer is reconstructed for all investigated mass-composition mixes, extragalactic directions of the dipole and extragalactic amplitudes of the dipole using Equations (5.4). Reconstructed directions and amplitudes are then compared with the features of the dipole measured by the Pierre Auger Observatory. The realisations of the extragalactic dipole (with given direction, mass composition and amplitude) are selected as solutions if the direction and amplitude of the resulting

[3]Here, shift of the dipole is defined as the angular difference between the extragalactic direction of the dipole and the direction of the dipole on the observer after propagation in the GMF.

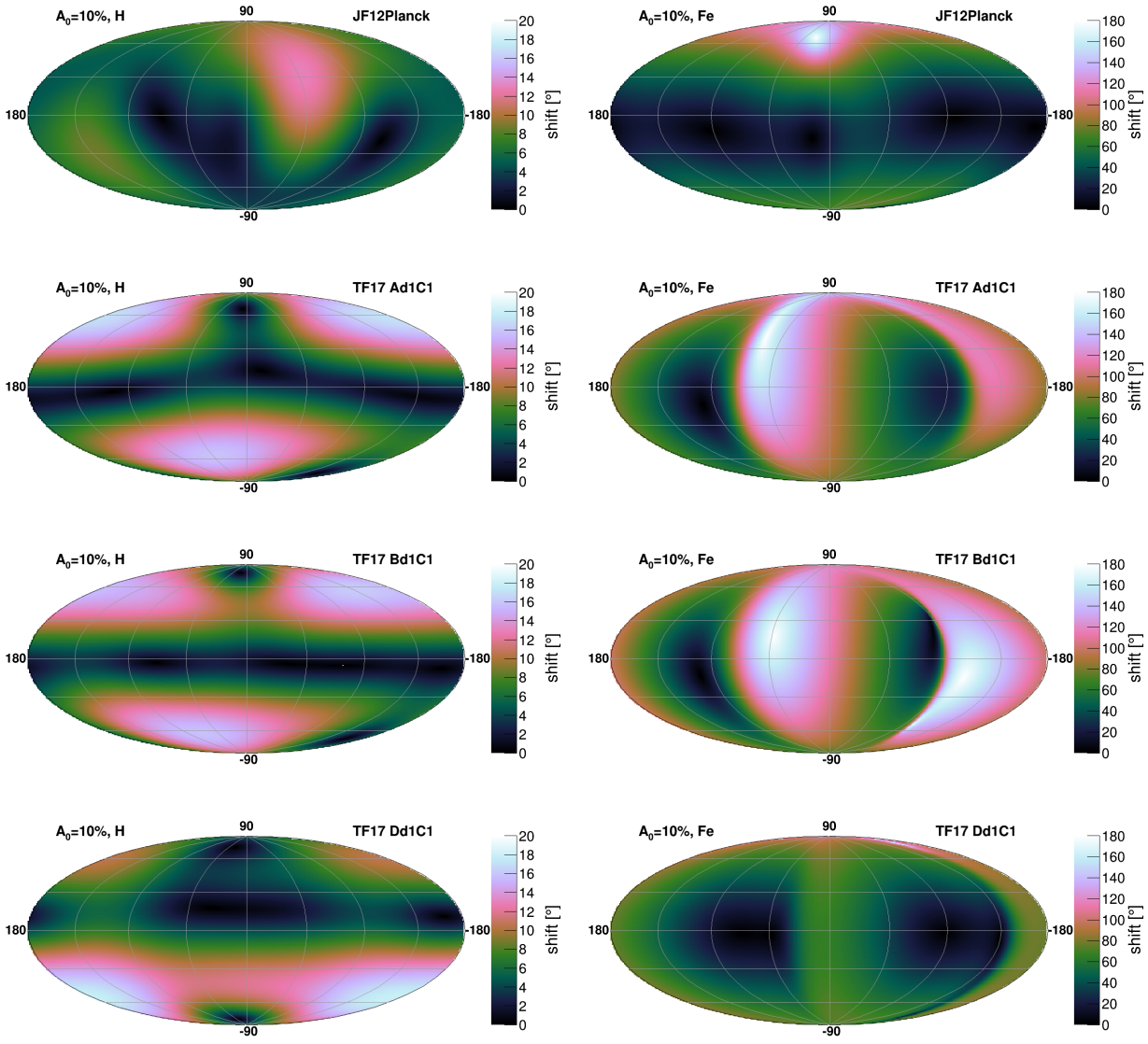

Figure 5.6: The shift of the dipole direction for different extragalactic directions of the dipole for protons (left) and iron nuclei (right) of energies above 8 EeV using the JF12Planck model with $l_c = 60$ pc, Ad1C1, Bd1C1, and Dd1C1 option of the TF17 model of the GMF from top to bottom, respectively. The sky maps are in galactic coordinates. Figures for JF12Planck and TF17 Bd1C1 taken from my publication [84].

dipole on Earth agree with the Auger measurements at 1σ or 2σ level, i.e. an amplitude of $6.5^{+1.3}_{-0.9}\%$ and direction with right ascension $\alpha_{\rm d} = (100 \pm 10)^\circ$ and declination $\delta_{\rm d} = (-24^{+12}_{-13})^\circ$. In the following figures, the solutions identified for simulations using the JF12Planck model of the GMF are taken as a sum of solutions found for the individual realisations of the field. In case of the TF17 model of the GMF, the identified solutions are shown as a sum of solutions found using the Ad1C1, Bd1C1, and Dd1C1 options of the TF17 model.

5.4.1 Single-element scenario

The simplest case of the cosmic-ray composition is the single-element scenario. Even though the current measurements suggest mixed composition of cosmic rays above 8 EeV, we first present the allowed extragalactic directions of the dipole for the single-element scenario, in order to demonstrate the differences between the individual primaries. The simulated energy spectrum is the same for the four particle species, therefore the influence of the GMF becomes more significant with the higher atomic number as the rigidity decreases.

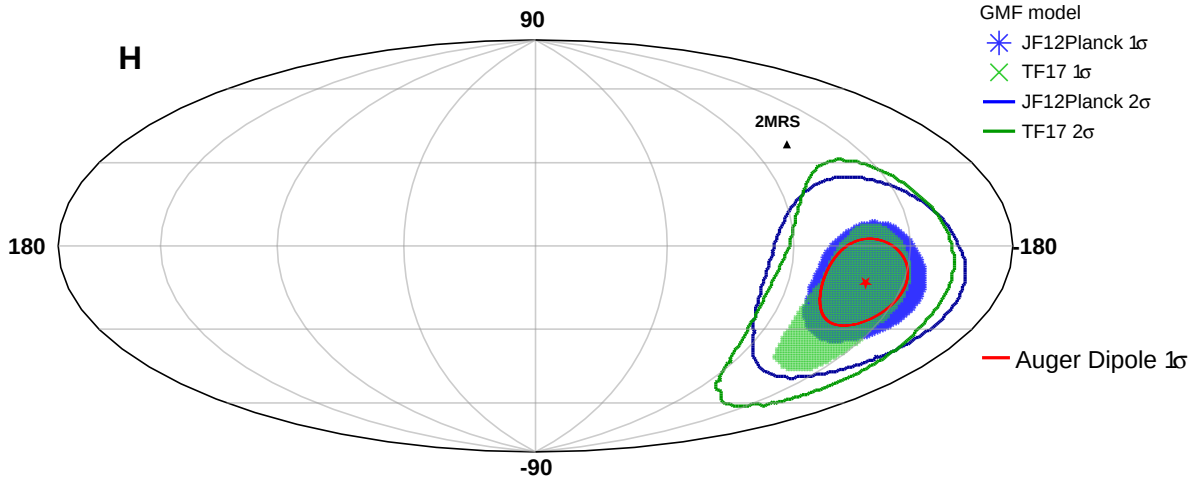

Figure 5.7: The directions of the extragalactic dipole in galactic coordinates compatible with the measured direction and amplitude by the Pierre Auger Observatory at 1σ and 2σ level found for the JF12Planck and the TF17 models of the GMF for the pure-proton scenario. The results from the Pierre Auger Observatory are indicated in red for 1σ c.l. Direction of the 2MRS dipole is depicted by the black triangle. Figure taken from my publication [84].

Proton: The identified possible directions found for the JF12Planck and TF17 models of the GMF for pure protons are shown in Figure 5.7 at the 1σ and 2σ level. The allowed

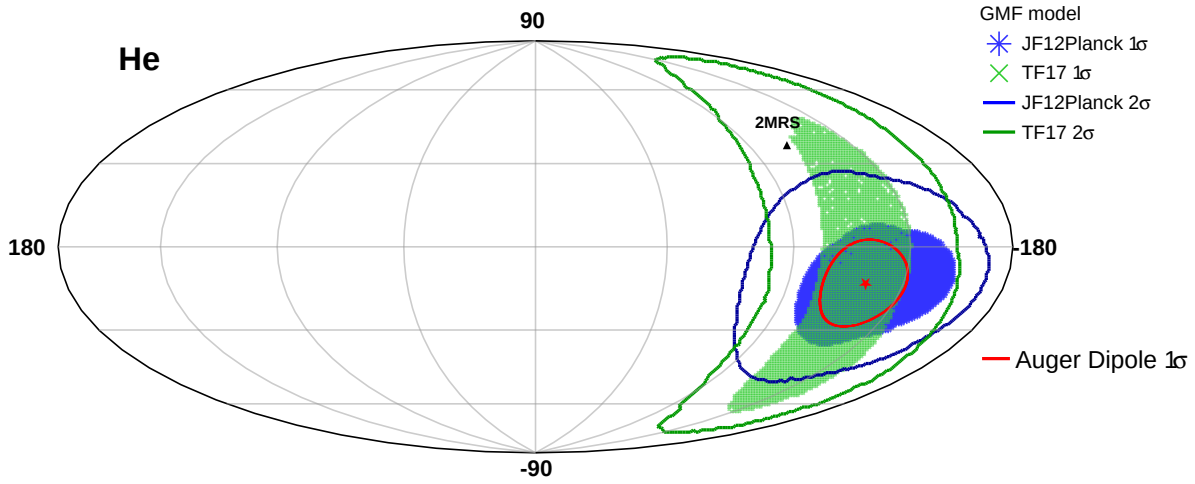

Figure 5.8: Same as in Figure 5.7, but for pure-helium scenario. Figure taken from my publication [84].

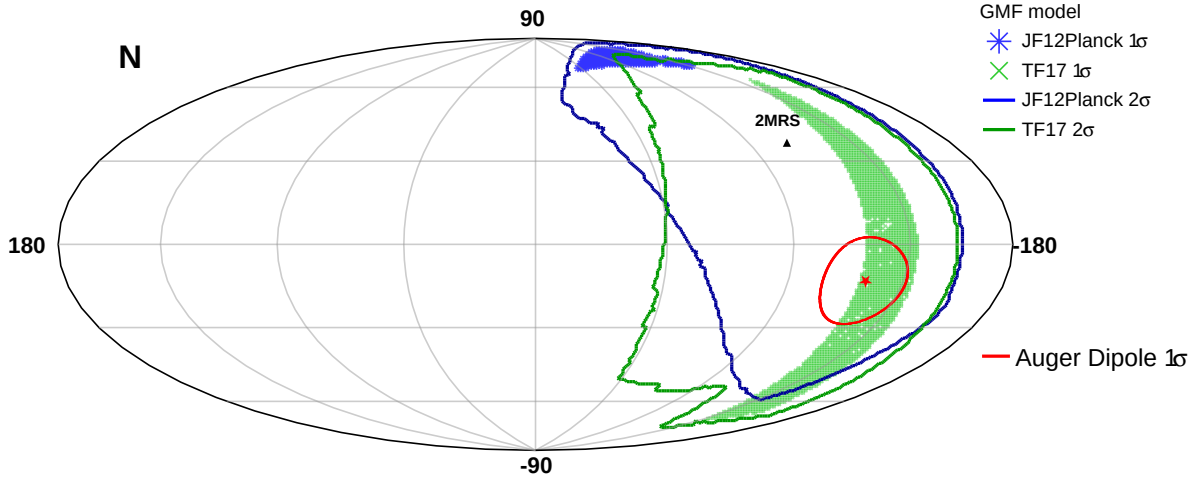

Figure 5.9: Same as in Figure 5.7, but for pure-nitrogen scenario. Figure taken from my publication [84].

directions of the extragalactic dipole are located in a close vicinity of the measured dipole direction. At the 1σ level, the directions are within $\sim 25^\circ$ and $\sim 35^\circ$ from the measured direction of the dipole on Earth for the JF12Planck model and TF17 model of the GMF, respectively. Furthermore, in case of a pure-proton scenario, all the solutions are for

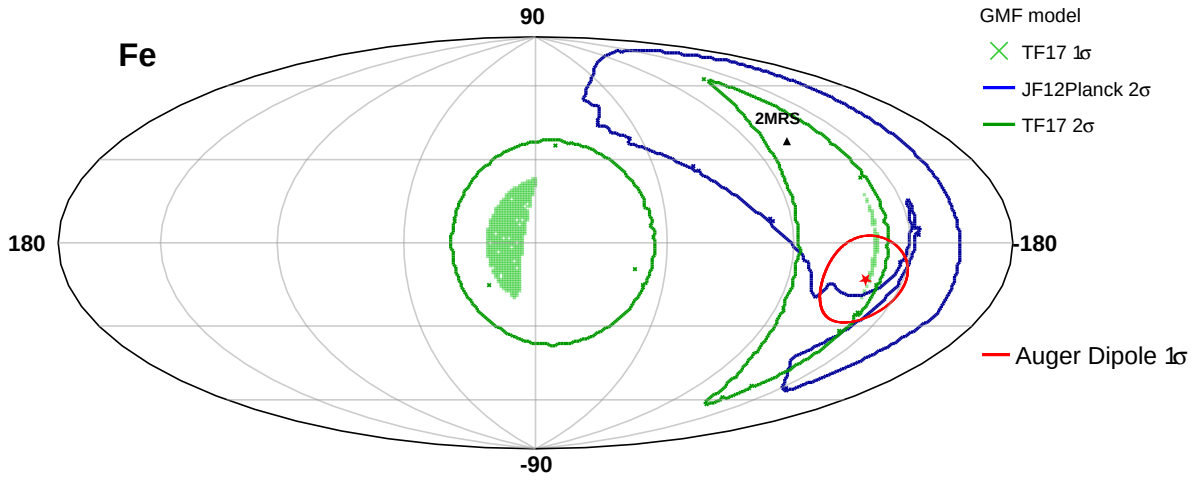

Figure 5.10: Same as in Figure 5.7, but for pure-iron scenario. No solutions are found for comparison at the 1σ level for the JF12Planck model. Figure taken from my publication [84].

extragalactic amplitudes of the dipole $A_0 \leq 10\%$ for both models of the GMF.

Helium nuclei: The areas of allowed directions of the extragalactic dipole in case of pure-helium scenario are depicted in Figure 5.8 for the two GMF models. Similarly to the pure-proton composition, the allowed directions of the extragalactic dipole in case of pure helium nuclei simulated in the JF12Planck model of the GMF at the 1σ level are rather close to the direction of the dipole measured by the Pierre Auger Observatory (specifically, within $\sim 35°$). However, the area of allowed directions of the extragalactic dipole at the 1σ level are extending up to $\sim 60°$ from the measured direction of the dipole using the TF17 model of the GMF. The initial amplitudes of the solutions are $A_0 \leq 10\%$ and $A_0 \leq 16\%$ for the JF12Planck and TF17 model of the GMF, respectively.

Nitrogen nuclei: Allowed directions of the extragalactic dipole for pure-nitrogen scenario at the 1σ and 2σ level are depicted in Figure 5.9 for the two GMF models. Because of the lower rigidities, the dipole is modified during the propagation in the GMF more extensively compared to protons or helium nuclei. That results in the allowed directions at the 1σ level in case of the JF12Planck GMF model located from $\sim 85°$ to $105°$ from the measured direction of the dipole on Earth. These solutions are for initial amplitudes $\geq 14\%$. The allowed directions of the extragalactic dipole at the 1σ level for the TF17 model are located in an extended band around longitudes from $210°$ to $240°$ and initial amplitudes $\geq 10\%$. It is worth noting that all the identified allowed directions for the TF17 model of the GMF are coming from the simulations using the Dd1C1 option of the model.

Iron nuclei: The allowed extragalactic directions of the dipole for the pure-iron nuclei

scenario at the 1σ and 2σ level are depicted in Figure 5.10 for the two GMF models. No allowed directions of the extragalactic dipole are identified at the 1σ level for the JF12Planck model of the GMF. Solutions were only identified at the 2σ level. Concerning the TF17 model, two areas of allowed directions of the extragalactic dipole are found for the initial amplitude $A_0 = 20\%$. The first area is located in a narrow band around the mean longitude of 232° close to the measured direction of the dipole by Auger and was found using the Dd1C1 option of the TF17 model of the GMF. The second area is found for the Bd1C1 option of the TF17 model of the GMF and the directions are located in a close vicinity of the direction of the Galactic center. This, however, does not suggest a possible Galactic origin of the cosmic rays above 8 EeV as the simulated flux is of extragalactic origin.

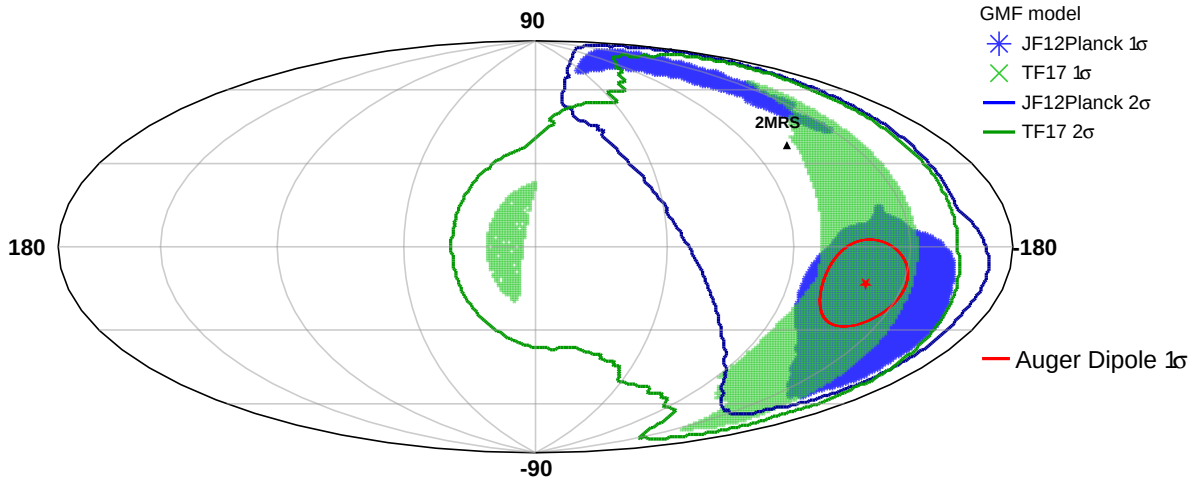

Figure 5.11: The directions of the extragalactic dipole in galactic coordinates found for all various mass composition scenarios for the JF12Planck and TF17 models of GMF within 1σ. Areas of possible directions of the extragalactic dipole compatible with the measurements within 2σ are shown by blue and green contours for the JF12Planck and TF17 models, respectively. The 1σ contour of the dipole measured by the Pierre Auger Observatory above 8 EeV is shown in red and the direction of the 2MRS dipole is displayed with the black triangle marker. Figure taken from my publication [84].

5.4.2 Mixed mass composition scenario

Current measurements of the mass composition of cosmic rays suggest that above 8 EeV the mass composition is mixed and the mean $\ln A$ is evolving with increasing energy towards heavier mass composition [49,100,101], see Section 4.2. In this study, we assume a constant abundance of individual elements in the whole energy range from 8 EeV up to 100 EeV for

simplicity. This approximation can be used as the dominant contribution to the large-scale anisotropy comes from the energies just above 8 EeV due to the steeply decreasing flux. No restrictions on the mean mass composition were used in this work. Therefore, we take into account all the possible mixes of the four elements with a step in relative fractions of 5%, going from the lightest, pure proton, to the heaviest, pure iron, composition.

The identified allowed directions of the extragalactic dipole throughout all the possible mass-composition mixes of the primaries, including the single-element scenarios, are shown in Figure 5.11 for both models of the GMF. Two separated areas of the allowed extragalactic directions are found for both models of the GMF at the 1σ level. At the 2σ level, there is no separation and the allowed directions of the extragalactic dipole are located in one closed area for both models. These areas extend as far as $\sim 115^\circ$ and $\sim 155^\circ$ from the measured direction of the dipole on Earth for the JF12Planck and TF17 model of the GMF, respectively.

In case of the JF12Planck model of the GMF, the first group of solutions at the 1σ level is located in an extended area around the measured dipole direction, within $\sim 45^\circ$ dominated by low-mass mixes. The second area of allowed directions of the extragalactic dipole goes as far as $\sim 105^\circ$ from the measured direction of the dipole and these solutions are for nitrogen-dominated mass-composition mixes.

One of the areas of the allowed directions of the extragalactic dipole at the 1σ level using the TF17 model of the GMF is identical to the previously mentioned area for the pure iron nuclei that is located close to the direction of the Galactic center and corresponds to the initial amplitudes of $A_0 = 20\%$ and particles propagated in the Bd1C1 option of the TF17 model of the GMF. The second group of solutions is located within $\sim 80^\circ$ from the measured direction of the dipole and covers a wide range in latitudes and narrower band of longitudes.

The normalized number of allowed directions of the extragalactic dipole in the 1° by 1° grid in longitude and latitude with respect to the mean (variance of) $\ln A$ for different initial amplitudes at the 1σ level is shown in the left (right) panels in Figure 5.12 and Figure 5.13 for the JF12Planck and TF17 models of the GMF, respectively. The evolution of the number of solutions with the mean $\ln A$ and increasing initial amplitude is visible. With the higher initial amplitude of the extragalactic dipole, a heavier composition is needed in order to describe the data well. The heavier elements are needed to sufficiently suppress the amplitude so that after the propagation inside the Galaxy the amplitude decreases and is compatible with the measured amplitude by the Pierre Auger Observatory.

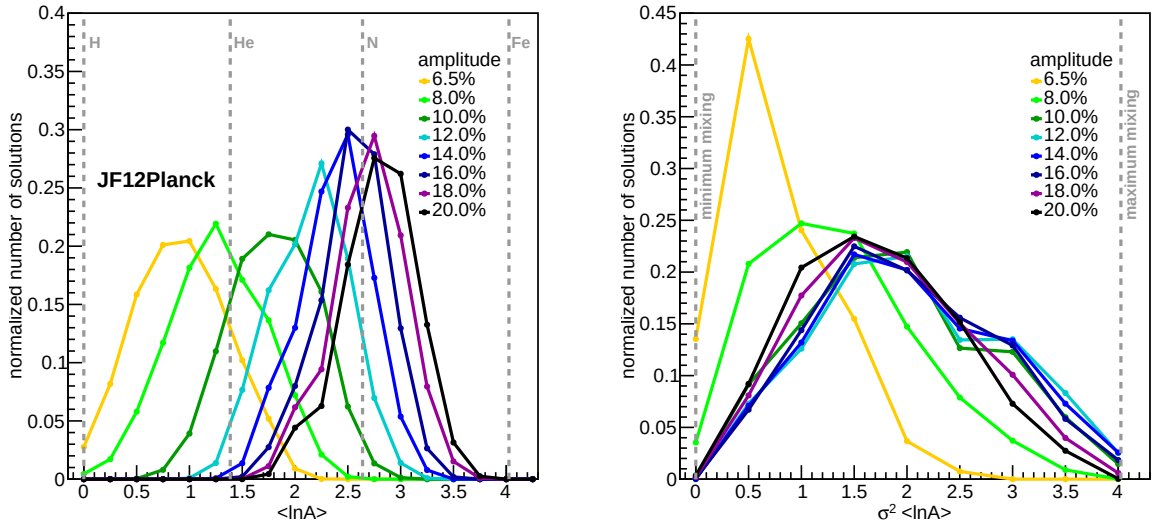

Figure 5.12: Number of allowed extragalactic directions of the dipole with respect to mean $\ln A$ (left) and with respect to the variance of the $\ln A$ (right) for different initial amplitudes for JF12Planck model of the GMF. Only directions with 1σ agreement with the measurement by the Pierre Auger Observatory are shown. Figure taken from my publication [84].

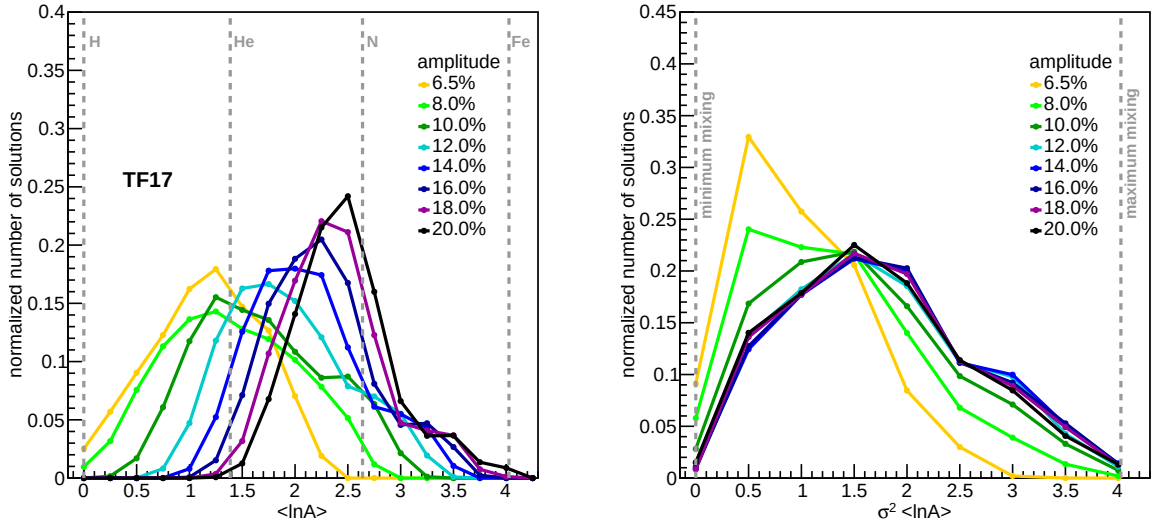

Figure 5.13: Same as in Figure 5.12, but using the TF17 models of the GMF. Figure taken from my publication [84].

5.5 Dipole in arrival directions at lower energies

The search for large-scale anisotropies by the Pierre Auger Observatory shows that the most significant dipole is found for energies above 8 EeV. However, dividing the detected cosmic rays into multiple energy bins also suggests that the dipole amplitude is evolving with energy (see Section 4.3). At lower energies, from 4 EeV up to 8 EeV, the direction of the reconstructed dipole is pointing towards right ascension $(80 \pm 60)^\circ$ and declination $(-75^{+17}_{-8})^\circ$ with amplitude $2.5^{+1.0}_{-0.7}$ % [108]. Nevertheless, this dipole is not statistically significant (less than 3σ).

A possible common origin of these two dipole anisotropies cannot be excluded. However, it is not known if the sources producing cosmic rays with energies $(4-8)$ EeV have the same or different distribution as the sources of cosmic rays above 8 EeV. The lower amplitude of the dipole at energies $(4-8)$ EeV might be caused by the influence of the GMF and isotropisation of the cosmic-ray flux. Nevertheless, it is also possible that the distribution of sources is different and that additional sources, that are not capable of accelerating particles to the highest energies, contribute here as well, possibly even as an isotropic component. We investigate allowed extragalactic directions of the dipole at these lower energies and the possibility of the same origin of the dipole between $(4-8)$ EeV and above 8 EeV. For that purpose, we repeat the same analysis using simulations of cosmic rays of energies $(4-8)$ EeV in the two models of the GMF.

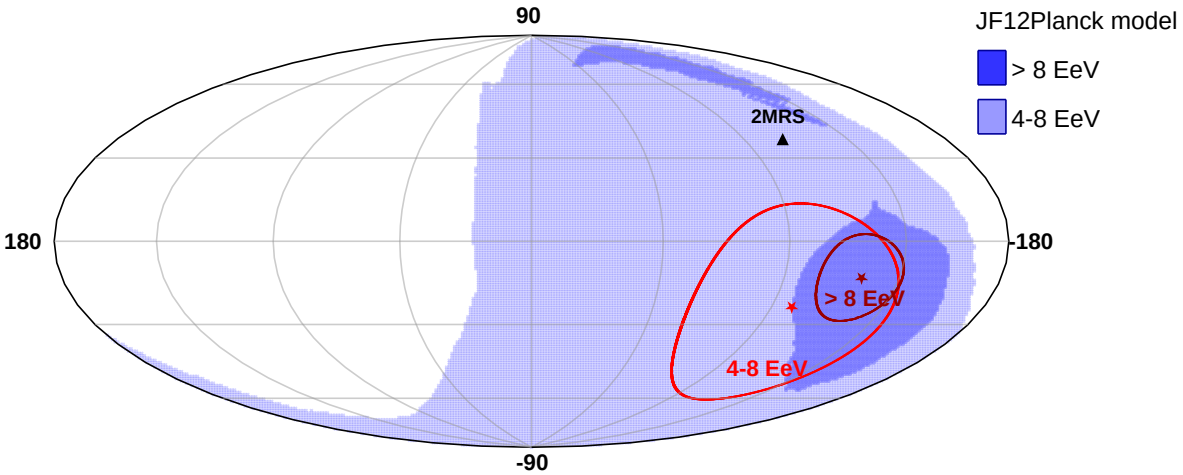

Figure 5.14: Areas of the allowed extragalactic dipole directions in galactic coordinates compatible with the measured direction of the dipole within 1σ by the Pierre Auger Observatory (red contour) with energies $4-8$ EeV (light blue) and above 8 EeV (dark blue) using the JF12Planck model of the GMF. The amplitude of the lower energy dipole on Earth is considered to be less than 4%. Figure taken from my publication [84].

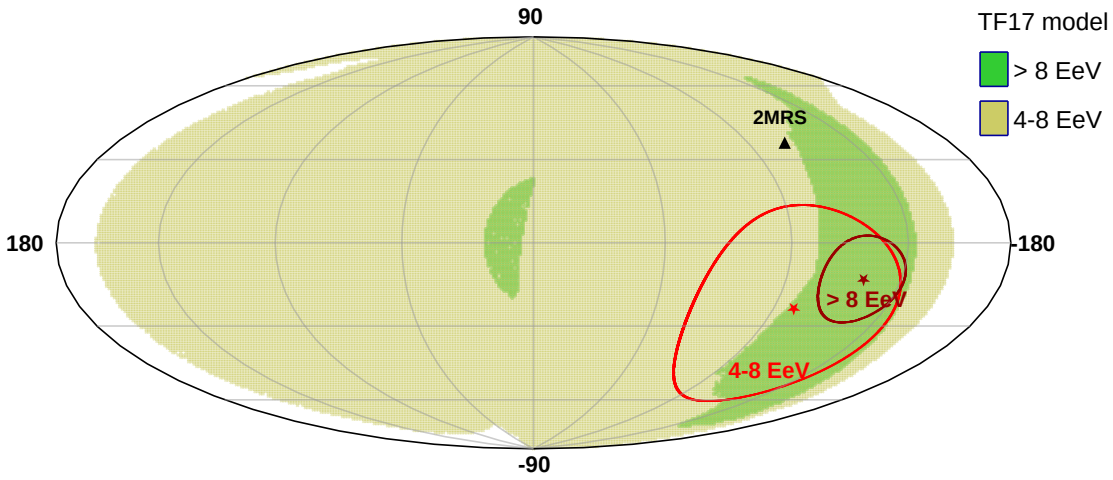

Figure 5.15: Same as in Figure 5.14, but using the TF17 model of the GMF. Figure taken from my publication [84].

The directions of the extragalactic dipole of cosmic rays between 4 EeV and 8 EeV compatible with the measurements by the Pierre Auger Observatory at the 1σ level are shown in Figure 5.14 and Figure 5.15 for the JF12Planck and TF17 models of the GMF, respectively. The allowed directions at the 1σ level presented in the previous section for the dipole above 8 EeV are plotted here as well for comparison. It can be seen that the areas of allowed direction of the extragalactic dipole at energies $(4 - 8)$ EeV are much more extended compared to the results for the higher-energy bin. There are two reasons for this. The first one is the fact that the uncertainties of the measurement of the dipole properties are much larger for the dipole at lower energies, leading to a larger amount of solutions compatible at the 1σ level. Secondly, the cosmic-ray flux has lower rigidity, causing larger deflections in the GMF. In case of the JF12Planck model of the GMF, the allowed extragalactic directions of the dipole at lower energies extend through more than half of the sky (Figure 5.14), mostly located at longitudes above 180°. In case of the TF17 model of the GMF, the allowed directions are covering almost the whole sky (Figure 5.15).

5.6 Cross-checks of obtained results

5.6.1 Spectral index

Few simplifications are used in the presented approach. One of such is the use of the spectral index $\gamma = 3$ for the whole energy range. In reality, there are features in the energy spectrum where the spectral index changes (see Section 4.1). The value used in this work was chosen as a close approximation of the spectral index of cosmic-ray energy spectrum

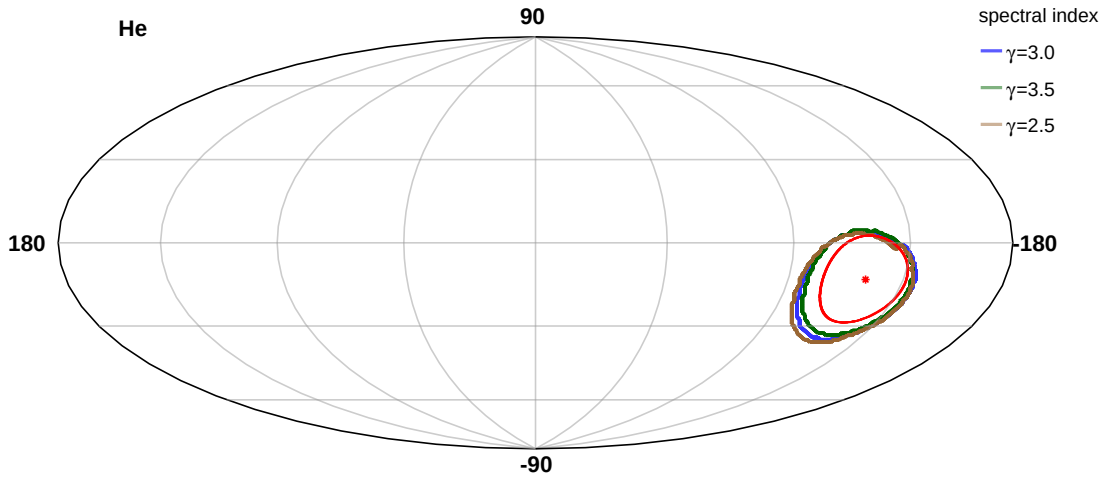

Figure 5.16: Allowed directions of the extragalactic dipole of cosmic rays above 8 EeV for allowed extragalactic directions at the 1σ level in case of helium nuclei propagated in the JF12Planck model of GMF for three spectral indices. The red marker depicts the measured direction of the dipole on Earth together with the red 1σ contour. Figure taken from my publication [84].

measured above 8 EeV by the Pierre Auger Observatory [40] and Telescope array [126]. Moreover, as the energy spectrum is steeply decreasing, the dipole anisotropy is dominated by particles with energies just above 8 EeV, where the $\gamma = 3$ is a good approximation of the spectral index.

In order to study how the results change under different spectral indices, we investigate two different spectral indices, namely $\gamma = 2.5$ and $\gamma = 3.5$ for pure proton and pure helium scenario as a cross check of the obtained results. We check the resulting areas of allowed extragalactic directions at the 1σ level for one realisation of the JF12Planck field. We find that borders of these areas for spectral indices $\gamma = 2.5$ and $\gamma = 3.5$ differ by maximally 3° when compared to the presented results for the spectral index $\gamma = 3$. The allowed directions of the extragalactic dipole for the three spectral indices and for the case of helium nuclei are shown in Figure 5.16.

5.6.2 χ^2 tests

The allowed directions of the extragalactic dipole presented in Section 5.4 were obtained by comparing the features of the three-dimensional dipole according to [108] at the 1σ and 2σ level with the three-dimensional dipole reconstructed for the simulated particles using Equations (5.4). The dipole in the arrival directions on the observer in the right ascension can be reconstructed by the Rayleigh analysis as in [2]. However, the behavior of the dipole

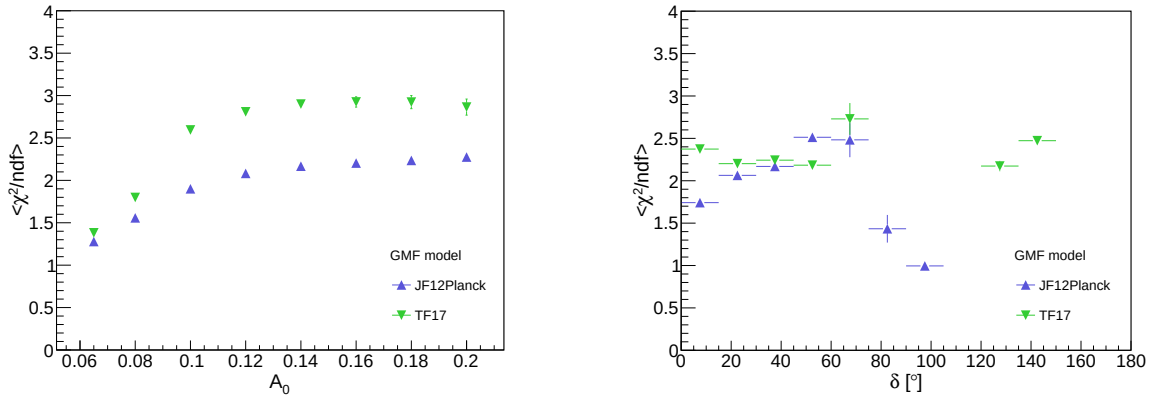

Figure 5.17: The evolution of the mean χ^2/ndf of the dipole fit of the arrival directions of cosmic rays in the right ascension with initial amplitude of the dipole (left) and with the angular distance between the direction of the extragalactic dipole and the measured dipole direction on Earth. The results for the two models of the GMF are shown. Figure taken from my publication [84].

in the right ascension in this work was checked by fits of the normalized distributions of arrival directions for all the found solutions by the dipole function

$$f(x) = A_{obs}^{dip} \sin(x + \phi_{dip}) + 1, \tag{5.5}$$

where A_{obs}^{dip} corresponds to the dipole amplitude in the right ascension on the observer and ϕ_{dip} is a phase of the dipole distribution and by a dipole+quadrupole function

$$g(x) = A_{obs}^{dip} \sin(x + \phi_{dip}) + A_{obs}^{quad} \sin(2x + \phi_{quad}) + 1, \tag{5.6}$$

where A_{obs}^{quad} corresponds to the quadrupole amplitude in the right ascension on the observer and ϕ_{quad} is its phase shift. The distribution of the arrival directions in the right ascension was also compared to the isotropic flux.

In case of the JF12Planck model of the GMF, distribution of the χ^2/ndf values for the dipole case has the mean of 1.9 with a standard deviation of 0.9, while the mean of the χ^2/ndf values distribution for the isotropy is $\chi^2/ndf = 72$ with a standard deviation of 24.

Concerning the TF17 model of the GMF, the distribution of the χ^2/ndf values for the dipole fit has the mean of $\chi^2/ndf = 2.2$ with a standard deviation of 1.0. The isotropy fit has a mean value of $\chi^2/ndf = 79$ with a standard deviation 27.

In case of the quadrupole fit, for both of the models of the GMF, the fitted quadrupole amplitude is not statistically significant (under 3σ) and is an order of magnitude lower compared to the dipole amplitude.

The evolution of the mean χ^2/ndf with the initial amplitude of the extragalactic dipole and with the angular distance between the direction of the extragalactic dipole and the measured dipole direction is shown in Figure 5.17.

5.6.3 Uncertainties of the Galactic magnetic field models

The models of the GMF used for this work of course contain uncertainties of the individual fitted model parameters. In the results previously presented in this chapter, only the best-fit parameters were used for each of the GMF models.

Concerning the JF12Planck model of the GMF, the uncertainties of the model were implemented by using multiple coherence lengths of the random turbulent component of the field. Similar approach was also used in [120]. Changing the coherence length of the turbulent field works in a similar manner as changing the strength of the overall field.

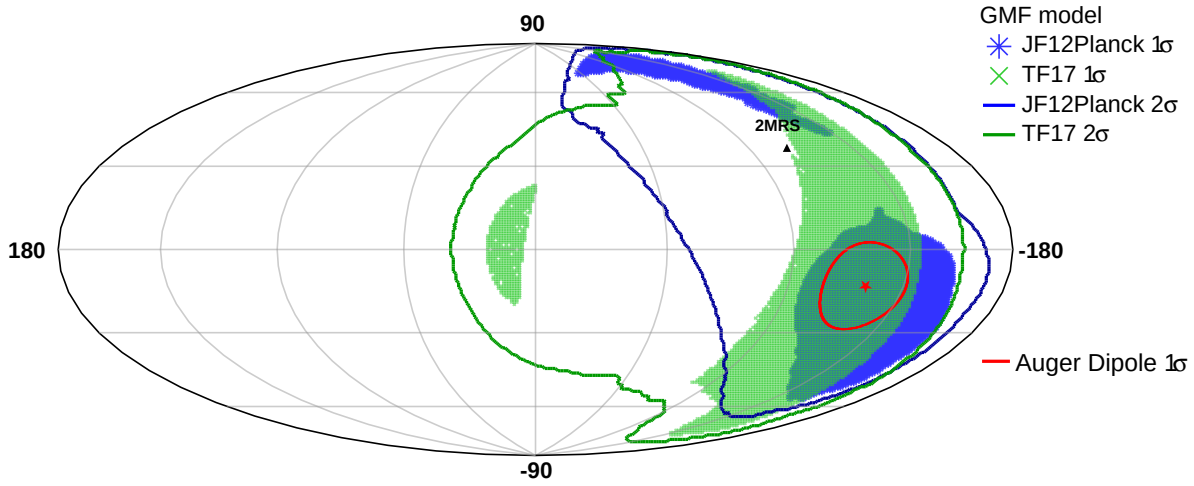

Figure 5.18: Same as Figure 5.11 with the strength of the three options of the TF17 model of the GMF adjusted by ±10%. Figure taken from my publication [84].

The TF17 model of the GMF does not include any random components, therefore this GMF model is static. In order to investigate the model uncertainties in an approximate way, we made some ad-hoc changes to the field strength parameters by changing them by ±10% in both the disc and the halo field components[4]. New simulations of the particle propagation in all three options of the TF17 model of the GMF were performed and the overall skymap of the allowed directions of the extragalactic dipole combining the results from the "best fit" model and the adjusted models can be seen in Figure 5.18. Overall, the allowed areas of extragalactic dipole directions are slightly larger (by $\sim$ few degrees) compared to the results obtained for the best fit model (Figure 5.11) as is expected when such changes to the model are applied.

[4]Similar approach can not be used in case of the JF12Planck model of the GMF as this model is a multi parameter model and not all of the parameters are independent. Consequently, such ad-hoc changes can result in unexpected alterations, not only in the field strength but also in its overall structure and it can not be guaranteed that such modified field is still consistent with the observational values of Faraday rotations and polarized light that it was fitted to.

5.7 Discussion of the results

The directions of the extragalactic dipole of cosmic rays above 8 EeV compatible with the measurement by the Pierre Auger Observatory at the 1σ and 2σ level are shown in Section 5.4 in Figures (5.7-5.11). In case of light composition (protons and helium nuclei), the results suggest the direction of the extragalactic dipole within $\sim 35^\circ$ and $\sim 60^\circ$ from the measured dipole direction on Earth for the JF12Planck and TF17 models of the GMF, respectively. Taking into account heavier composition, the direction of the extragalactic dipole can be as far as $\sim 115^\circ$ (JF12Planck) and $\sim 155^\circ$ (TF17) from the measured dipole on Earth at the 2σ level. The chosen approach of using multiple realisations of the JF12Planck model of the GMF with multiple coherence lengths was done in order to include uncertainties of the model. In case of the TF17, where no random components of the field are present, the uncertainties were mimicked by using three options of the field. Altering the strength of the TF17 model of the GMF was also investigated (see Section 5.6.3). However, it is worth noting that results obtained with the TF17 model of the GMF should be interpreted with caution as this GMF model reaches very high amplitudes of the field strength, especially in the Ad1C1 and Bd1C1 options (see Section 3.2.1).

The identified areas of the allowed directions of the dipole include interesting astrophysical systems, that are often considered as candidate sources of UHECRs or correspond to higher density of matter regions in local universe. At the 2σ level, the Centaurus A region lies within the region of allowed directions of the extragalactic dipole identified in Section 5.4. This source is generally interesting as a candidate source of UHECRs as it is close to the Milky Way (~ 3.8 Mpc). Furthermore, the direction of the 2MRS dipole [125] is well within the allowed directions of the extragalactic dipole presented in Section 5.4. The origin of large-scale anisotropies from the source distribution following a large-scale structure (LSS) was investigated in [120] and shows that a dipole similar to the one we observe on Earth might arise from such a source distribution. In that study, pure proton composition is found not to be compatible with the measured data. However, this is not in contradiction with presented results in this thesis, even though it is shown that allowed dipole directions for pure-proton scenario exist. This is due to the fact, that we allow the extragalactic dipole in all possible directions and not only towards the LSS. However, current measurements of UHECRs above 8 EeV are in contradiction with the pure-proton scenario [100].

Concerning the mass composition of cosmic rays above 8 EeV, the experimental results suggest the mean $\ln A$ of cosmic rays heavier than helium nuclei [100]. Moreover, there are hints that the mean $\ln A$ is currently underestimated due to uncertainties of models of hadronic interactions used for the mass-interpretation of measurements [104, 127]. Based on the presented results, allowed directions of the extragalactic dipole with the mean $\ln A$ heavier than helium nuclei can be found for all the investigated initial amplitudes. Further constraints on the initial amplitude might be made using an energy dependent mass composition of cosmic rays.

Regarding the dipole at lower energies, our results can not confirm or reject the possibility of the same origin of the dipole anisotropies at $(4 - 8)$ EeV and above 8 EeV. The

regions of allowed directions of the extragalactic dipole at energies $(4-8)$ EeV and above 8 EeV overlap for both models of the GMF (see Figure 5.14 and Figure 5.15). However, the much larger areas of allowed directions of the extragalactic dipole at $(4-8)$ EeV energies extend over a large part of the sky.

Chapter 6

Single-source scenario at the highest energies

The energy spectrum of cosmic rays at the ultra-high energies is measured with a high precision by two current experiments; the Pierre Auger Observatory [9] in the Southern hemisphere and the Telescope Array [128] in the Northern hemisphere. Overall, the two measured energy spectra agree well, however, at the highest energies (above $\log(E/\mathrm{eV}) = 19.5$) the spectrum measured by the Pierre Auger Observatory and Telescope Array exhibit different flux suppression as was described in Section 4.1. This disagreement might be caused by the ability of the two experiments to observe different sources on the sky in the Northern and Southern hemispheres. In this work, a simplified scenario of a single source that would explain the structure of the end of the energy spectrum above $10^{19.5}$ eV as measured by the Pierre Auger Observatory is investigated.

This part of the thesis is a follow up on a research done for the Master's thesis of the author [129]. Compared to [129], the presented results in this Chapter are obtained for updated data points of the energy spectrum of cosmic rays above $10^{19.5}$ measured by the Pierre Auger Observatory. Moreover, based on the measurements by the Pierre Auger Observatory concerning the mass composition of the cosmic ray flux [100, 130], additional conditions are employed also on the mass composition of the simulated particles originating from a single source. These results were presented during my doctoral studies in [131, 132] and parts of the text are taken from these publications.

Section 6.1 presents the simulation approach of the extragalactic propagation of cosmic-ray particles and the source features. Section 6.2 describes the method of comparison of the energy spectrum predicted from simulated propagation of cosmic rays with the data measured by the Pierre Auger Observatory. The results are presented in Section 6.3 with the possible source features that are able to describe the measured energy spectrum above $10^{19.5}$ eV well. In Section 6.4, the possible single-source features describing well both the energy spectrum and the mass composition at energies above $10^{19.5}$ eV are presented. The obtained results are discussed in Section 6.5 together with a discussion about the possible anisotropy patterns in the arrival directions of cosmic rays in case of a single source at the highest energies.

6.1 Simulations of extragalactic cosmic rays from single source

The propagation of cosmic rays from a source to Earth is simulated in CRPropa 3 using the one-dimensional mode of propagation of particles in the universe. This means, that particles are propagated on a straight lines from the source to the observer and no effects of the Galactic and extragalactic magnetic fields are taken into account. Simulated particles can undergo energy loss processes by interactions with CMB and EBL during the propagation, as described in Chapter 3. The Gilmore12 [61] model of EBL is used. The individual energy loss processes, that were described in detail in Section 3.1, are electron-pair production, photo-pion production, and photodisintegration, that are caused by interactions with CMB and EBL. The photodisintegration cross sections are obtained from TALYS 1.6 [133] within the CRPropa 3. Moreover, particles can undergo a nuclear decay in case of unstable nuclei and additional energy losses are caused also by the cosmological redshift.

Four types of particles are propagated from the source to Earth; proton, helium ^{4}He, nitrogen ^{14}N and iron ^{56}Fe nuclei. Particles are injected with a power-law energy spectrum with the spectral index $\gamma = 2$ from the minimum energy $\log_{10}(E_{\mathrm{min}}/\mathrm{eV}) = 19.5$ up to a maximum rigidity $\log_{10}(R_{\mathrm{max}}/\mathrm{V}) = 20.5$. The position of the source ranges from 3 Mpc up to 100 Mpc with discrete steps. Between 3 Mpc and 20 Mpc the step is 1 Mpc and a step of 10 Mpc is used further of. For each type of the particle and the source distance a separate simulation set is created. Each simulation set consists of 10,000 particles[1].

To investigate potential sources with capability to accelerate particles to different maximum energies and different energy spectra, we apply a broken-rigidity exponential cutoff to the simulated energy spectrum as

$$\frac{\mathrm{d}N}{\mathrm{d}E} = E^{-\gamma} \cdot f_{\mathrm{cut}} \ , \tag{6.1}$$

where γ is the spectral index and f_{cut} is the rigidity exponential cutoff function defined for a given rigidity cutoff R_{cut} as

$$f_{\mathrm{cut}} = \begin{cases} 1 & (E < ZeR_{\mathrm{cut}}) \\ e^{\left(1-\frac{E}{ZeR_{\mathrm{cut}}}\right)} & (E > ZeR_{\mathrm{cut}}) \end{cases} , \tag{6.2}$$

where Z is the proton number of the particle, see e.g. [134,135]. We investigate the rigidity cutoff from $\log_{10}(R_{\mathrm{cut}}/\mathrm{V}) = 18.5$ with discrete steps of 0.1 up to $\log_{10}(R_{\mathrm{cut}}/\mathrm{V}) = 20.5$. Lower rigidity cutoffs were not investigated as the energy spectrum at the highest energies would be dominated by the exponential behavior of the generated energy spectrum for all the considered cosmic-ray species.

[1]This number is the amount of particles emitted from the source, the amount of particles collected on Earth then varies according to the source distance and type of the particle.

The energy spectrum is also reweighted to follow different spectral indices in the range $\gamma \in (1, 3)$ with a step of 0.5. The four particles are mixed with a step of 10% in the relative fraction making total of 286 possible mass composition scenarios at the source.

6.2 Comparison of simulations with measured data

The simulated energy spectrum for a given source distance and mass-composition mixes is reweighted to various spectral indices and rigidity cutoffs. The shape of the final energy spectrum is then compared with the shape of the energy spectrum measured by the Pierre Auger Observatory in the energy range from $10^{19.5}$ eV up to $10^{20.2}$ eV. The data of the cosmic-ray flux in individual energy bins measured by the Pierre Auger Observatory [52] is listed in Table 6.1.

In this work, we only compare the two energy spectra (measured and simulated) based on the shape of the measured spectrum and neglect the total flux. We take into account the statistical errors of the measured spectrum and statistical errors obtained from the simulations. In order to compare the shape of the measured and simulated energy spectra, both energy spectra are scaled so that the flux in the first energy bin $\log_{10}(E/\text{eV}) = 19.5 - 19.6$ is equal to 1.0. The reduced χ^2/ndf, where ndf = 6, is calculated for the simulated and measured energy spectra after the rescaling. A good agreement between the data and a simulation is defined by two conditions: the first condition is given by $\chi^2/\text{ndf} \leq 2$, the second condition requires that the simulated energy spectrum must contain particles in all the investigated energy bins.

$\log_{10}(E/\text{eV})$	J [$\text{km}^{-2}\text{yr}^{-1}\text{sr}^{-1}\text{eV}^{-1}$]
19.55	$\left(1.252^{+0.052}_{-0.050}\right) \cdot 10^{-21}$
19.65	$\left(5.98^{+0.32}_{-0.31}\right) \cdot 10^{-22}$
19.75	$\left(1.93^{+0.17}_{-0.15}\right) \cdot 10^{-22}$
19.85	$\left(8.10^{+0.99}_{-0.88}\right) \cdot 10^{-23}$
19.95	$\left(1.86^{+0.46}_{-0.38}\right) \cdot 10^{-23}$
20.05	$\left(5.5^{+2.5}_{-1.8}\right) \cdot 10^{-24}$
20.15	$\left(2.9^{+1.7}_{-1.2}\right) \cdot 10^{-24}$

Table 6.1: Data of the cosmic-ray flux measured by the Pierre Auger Observatory in energy bins $\log_{10}(E/\text{eV})$ with a step of 0.1 [52].

Additional conditions based on the mass composition measurements by the Pierre Auger Observatory can be applied in order to further restrict the features of a possible single source creating the energy spectrum at the highest energies as well as mass composition compatible with the measured data. The current data suggest a heavy composition at the highest energies (see Figure 4.4 in Section 4.2). Following the results from [100], we

take into account interpretation of the data measured by the Pierre Auger Observatory using EPOS-LHC and Sibyll 2.3c models of hadronic interactions. Interpretation by the QGSJet II-04 model is not taken into account as it suggests nonphysical values of the variance of the mean $X_{\max}$ (see Figure 4.5). Newer results were also presented in [136] using the measurements of $X_{\max}$ by FD detectors and using a deep neural network approach of extracting the $X_{\max}$ from the surface detectors. In this work, we require the mass composition of particles propagated to Earth with energy above $10^{19.5}$ eV to be heavier than nitrogen, i.e. $\langle \ln A \rangle_{Earth} \geq \ln 14$. Moreover, the variance of the mass composition must satisfy $\sigma^2 (\ln A)_{\text{Earth}} \leq 0.5$.

6.3 Single-source features constraining the energy spectrum

The energy spectra for different source distances D, spectral indices γ, maximum rigidity cutoffs R_{cut} and mass composition mixes are compared with the shape of the energy spectrum measured by the Pierre Auger Observatory by calculating the reduced χ^2 value. Without the additional condition on the mass composition on Earth, the phase space of allowed single source features producing the shape of the energy spectrum compatible with the measured one is quite large.

Good descriptions of the energy spectrum can be found for all the investigated spectral indices and the maximum rigidity cutoffs of the source. The minimum χ^2/ndf identified for the individual spectral indices with respect to the maximum rigidity cutoff is depicted in Figure 6.1. Note that the minimal values of χ^2/nfd are cut from the top at the value 2.5 in order to better visualise the values in the region of interest between $\chi^2/\text{ndf} = 0.0 - 2.0$. Sources with lower spectral indices, $\gamma = 1.0$ and $\gamma = 1.5$, are able to describe the shape of the energy spectrum above $10^{19.5}$ eV well only for a narrow range of rigidity cutoff values between $R_{\text{cut}} = 10^{19.0}$ V and $R_{\text{cut}} = 10^{19.6}$ V. For higher spectral indices, the range of possible R_{cut} values increases. A good description of the energy spectrum in the whole range of investigated R_{cut} values is found for the spectral index $\gamma = 3$.

The mean mass composition at the source and on Earth for different R_{cut} values for the found solutions is shown in Figure 6.2. The number of identified solutions is represented by the colour scale. Light composition both at the source and on Earth is possible for rigidity cutoff of the source $R_{\text{cut}} \geq 10^{19}$ V, while composition heavier than nitrogen on Earth from a single source can be only achieved for $R_{\text{cut}} \leq 10^{19.5}$ V in order to describe well the measured energy spectrum. No scenario with pure iron nuclei at the source (and on Earth) is able to describe the measured spectrum well. The variance of the mass composition on Earth for different R_{cut} values is depicted in Figure 6.3 with colour scale representing the number of solutions found. Note that the mass composition on Earth is usually lower than at the source due to the propagation effects, such as the photodisintegration of nuclei. However, an opposite case might arise as well, although not as frequently, i.e. the mass composition on Earth is heavier than at the source. This might be caused by the light particles (either

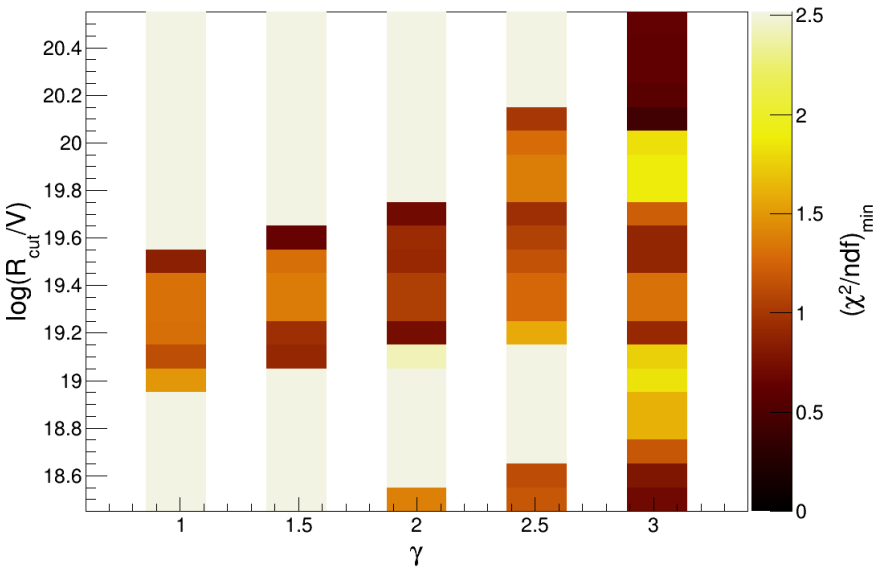

Figure 6.1: A minimal value of χ^2/ndf between measured energy spectrum and simulated energy spectrum identified for given combinations of rigidity cutoff R_{cut} and spectral index γ of the source. Minimal χ^2/ndf is scanned over all considered source distances and mass composition mixes at the source. The colour scale is limited by value of 2.5 from above in order to better visualise the lower values of χ^2/ndf. Figure taken from my publication [132].

from source or products of disintegration) losing too much energy and reaching Earth with an energy lower than $10^{19.5}$ eV. These particles are not taken into account in this work.

The number of found solutions for a given spectral index with respect to the mean mass composition at the source and on Earth is shown in Figure 6.4. It can be seen that a mass composition heavier than nitrogen (both at the source and on Earth) can describe the energy spectrum above $10^{19.5}$ eV well only for the spectral index $\gamma = 3$. On the other hand, the spectral index $\gamma = 1$ can only describe the energy spectrum well for the mean mass composition on Earth lighter than helium.

Figure 6.5 depicts the number of found solutions for a given spectral index and distance of the source. Vast majority of the solutions is for close sources. However, solutions were found even for sources in the distance of 100 Mpc.

6.4 Single-source features constraining the energy spectrum and mass composition

The amount of possible source features describing the energy spectrum well without the additional conditions on the mass composition on Earth is very large. To further restrict the possible features of a single source producing the energy spectrum above $10^{19.5}$ eV

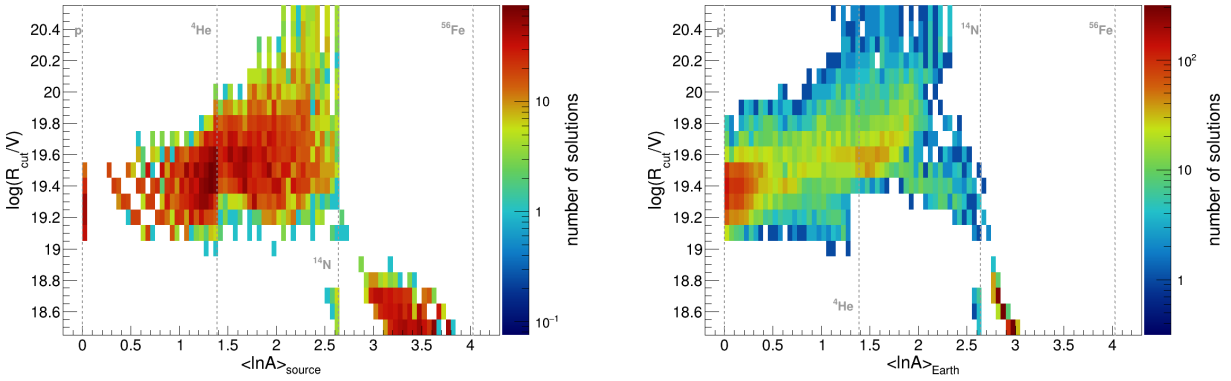

Figure 6.2: Distribution of identified solutions for the maximum rigidity cutoff at the source and the mean mass composition at the source (left) and on Earth (right).

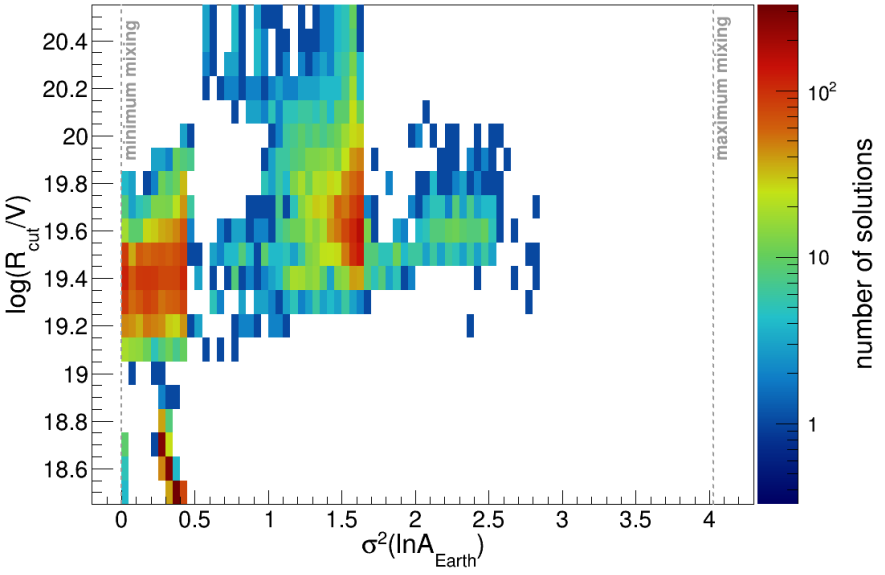

Figure 6.3: Distribution of identified solutions for the maximum rigidity cutoff at the source and the variance of the mass composition on Earth.

as measured by the Pierre Auger Observatory we apply the aforementioned cuts on the mass composition as $\langle \ln A \rangle_{\text{Earth}} \geq \ln(14)$ and $\sigma^2(\ln A) < 0.5$ which significantly restrict the possible single source features as can be already seen from the plots in the previous section.

The number of solutions for different values of R_{cut} with respect to the mean mass composition at the source and on Earth after applying additional mass-composition cuts is shown in Figure 6.6. After the cut on the mass composition on Earth, the rigidity cutoff of the single source is restricted to values $R_{\text{cut}} \leq 10^{19.2}$ V. Such low values of R_{cut} are needed

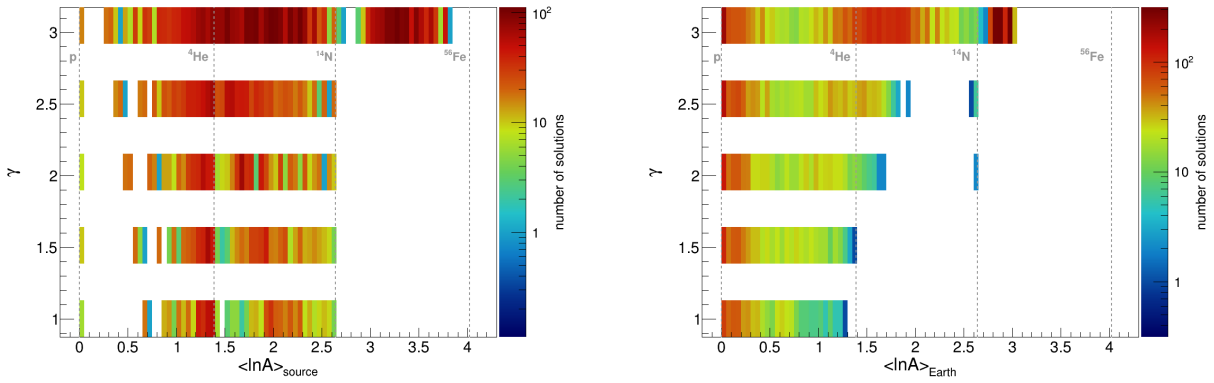

Figure 6.4: Number of solutions describing the energy spectrum above $10^{19.5}$ eV well for different spectral indices at the source with respect to the mass composition at the source (left) and on Earth (right).

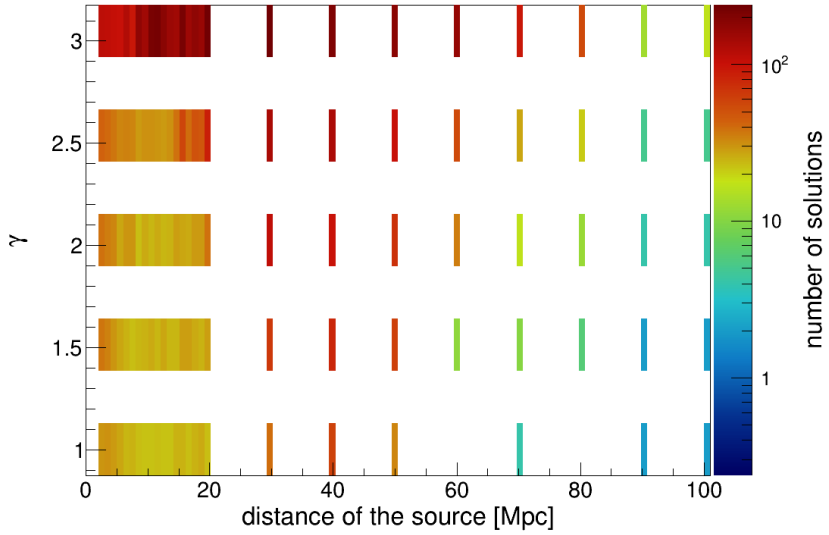

Figure 6.5: Number of solutions describing the energy spectrum above $10^{19.5}$ eV well for different spectral indices at the source with respect to the distance of the source.

in order to sufficiently suppress the presence of light elements in the energy spectrum above $10^{19.5}$ eV.

The number of remaining solutions after the cuts on the mass composition are depicted in Figure 6.7 for different spectral indices with respect to the distance of the source. All the identified solutions are for sources with the spectral index $\gamma = 3$. Moreover, a single source describing well both the energy spectrum and mass composition of cosmic rays above $10^{19.5}$ eV measured by the Pierre Auger Observatory should be closer than $\sim$ 20 Mpc from Earth. Potential single source located farther from Earth can not describe the mass

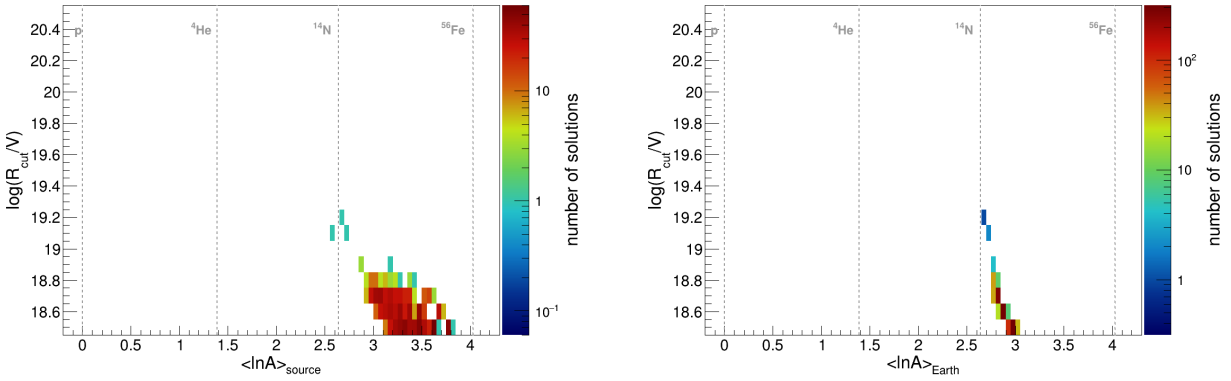

Figure 6.6: Number of identified solutions satisfying conditions on the description of the energy spectrum and mean mass composition on Earth for different rigidity cutoff R_{cut} with respect to the mass composition at the source (left) and on Earth (right).

composition well as the longer trajectory causes disintegration of the heavy elements thus pushing the $\langle \ln A \rangle$ to lower values than required in this work.

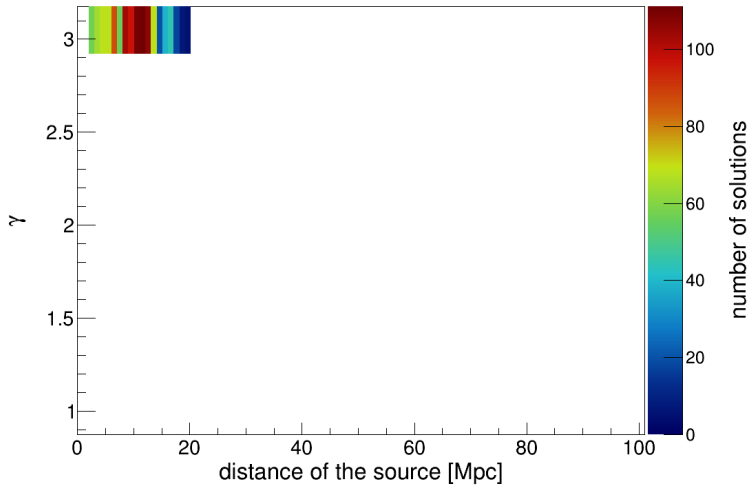

Figure 6.7: Number of identified solutions satisfying conditions on the description of the energy spectrum and mean mass composition on Earth for different spectral indices and distances of the source.

The energy evolution of the $\langle \ln A \rangle$ and the variance of the mass for the solutions found for $R_{\mathrm{cut}} = 10^{18.7}$ V is shown in Figure 6.8. All-particle energy spectra on Earth for these solutions and the decomposed energy spectra for four mass groups ($A = 1$, $1 < A < 5$, $5 \leq A < 17$ and $17 \leq A$) are depicted in Figure 6.9. A transition from the medium heavy to the heavy primary particles is clearly seen for all these particular solutions.

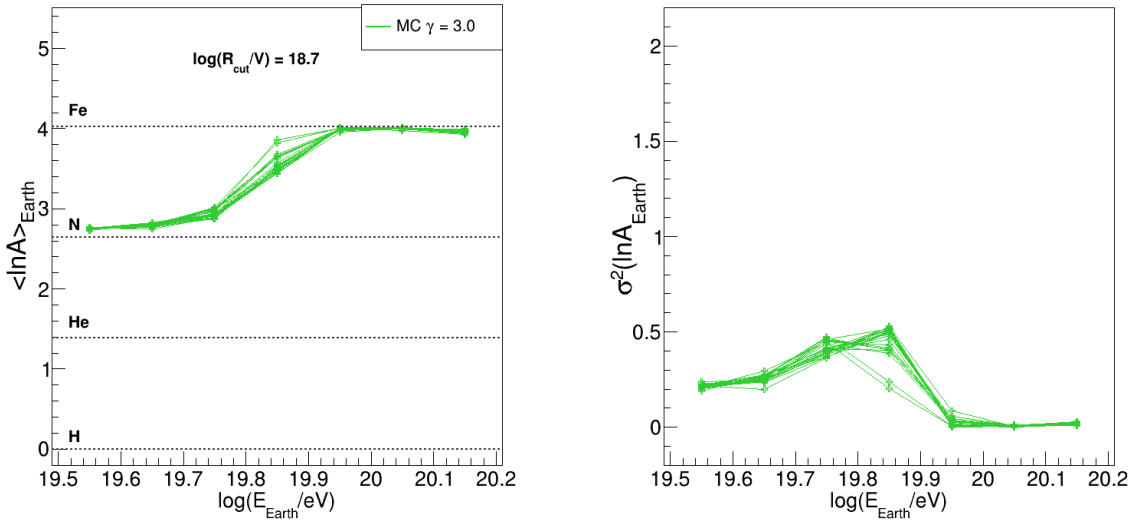

Figure 6.8: Illustration of the energy evolution of the mean mass composition (left) and variance of the mass (right) on Earth for the solutions identified for $R_{\rm cut} = 10^{18.7}$ V satisfying the conditions on the energy spectrum and mass composition on Earth. Figure taken from my publication [132].

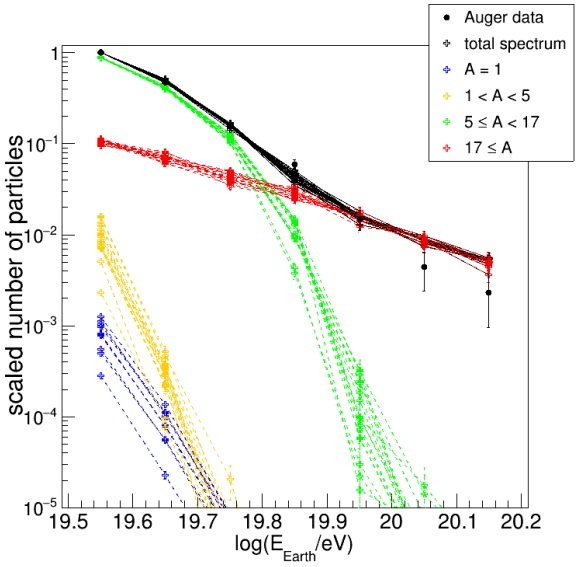

Figure 6.9: The all particle energy spectra on Earth (black lines) and energy spectra for four mass group categories for the solutions identified for $R_{\rm cut} = 10^{18.7}$ V satisfying the conditions on the energy spectrum and mass composition on Earth.

6.5 Discussion of the results

The possible features of a single source that could describe the shape of the energy spectrum and the mean mass composition of cosmic rays above $10^{19.5}$ eV as measured by the Pierre Auger Observatory include the source distance, spectral index, mass composition at the source and rigidity cutoff, as investigated in this chapter. In order to describe the shape of the energy spectrum, all the investigated values of the source features are identified to be able to describe the energy spectrum well apart from the very heavy mass composition at the source. For some source features, only specific combinations of those can describe the spectrum well as can be seen for example in Figure 6.1 for the connection between the spectral index and rigidity cutoff or in Figure 6.2 in the case of rigidity cutoff and mass composition at the source. After applying the additional conditions on the mean mass composition and variance of the mass on Earth, the parameter space of the possible single-source features is largely restricted. In order to describe well both the shape of the energy spectrum and the mean mass composition, the rigidity cutoff value should be $R_{\rm cut} \leq 10^{19.2}$ V, spectral index $\gamma \cong 3$ and the source should be within ~ 20 Mpc from Earth. Note that no magnetic fields are taken into account in this work. Therefore, the actual distance of a source should be even closer after taking into account the deflections of the cosmic ray trajectories.

It is also interesting to check for possible anisotropies that could be caused by a single source contributing at the highest energies. In a scenario when light particles are emitted from a single source at these energies, point like anisotropies are expected and a vast majority of these cosmic rays should be coming from the directions in a close vicinity of the direction of the source.

As an example, the arrival directions of cosmic-ray protons with energy $10^{19.5}$ eV originating in four selected sources and propagated using CRPropa 3 in the JF12Planck model of the GMF are visualised in Figure 6.10. The four selected directions of the sources correspond to the direction of Centaurus A (blue), Fornax A (green), UGC 1841 (red) and CGCG 114-025 (yellow). The extragalactic magnetic field is not simulated and particles are considered to originate in the given source if their arrival direction into the Galaxy is within 3° from the directions of the source[2]. The simulations are done using the backtracking of antiparticles from Earth to the edge of the Galaxy. This shows that detecting and identifying cosmic-ray protons at the highest energies is a great tool for identification of cosmic-ray sources as the deflections are minimal.

However, for heavier nuclei the picture changes. For comparison, the arrival directions of nitrogen nuclei and iron nuclei of the same energy, $10^{19.5}$ eV, and propagated in the JF12Planck model of the GMF are shown in Figure 6.11 and Figure 6.12, respectively. The corresponding rigidity is $\sim 10^{18.65}$ V for the nitrogen nuclei and $\sim 10^{18.1}$ V for the iron nuclei. It can be seen that for heavier cosmic rays the GMF tends to isotropise the arrival directions, although clustering of the events can be still visible, especially in the case of

[2]The deflections caused by the EGMF for particles originating at a source within 20 Mpc from Earth should be small and the 3° window should be sufficient to account for them.

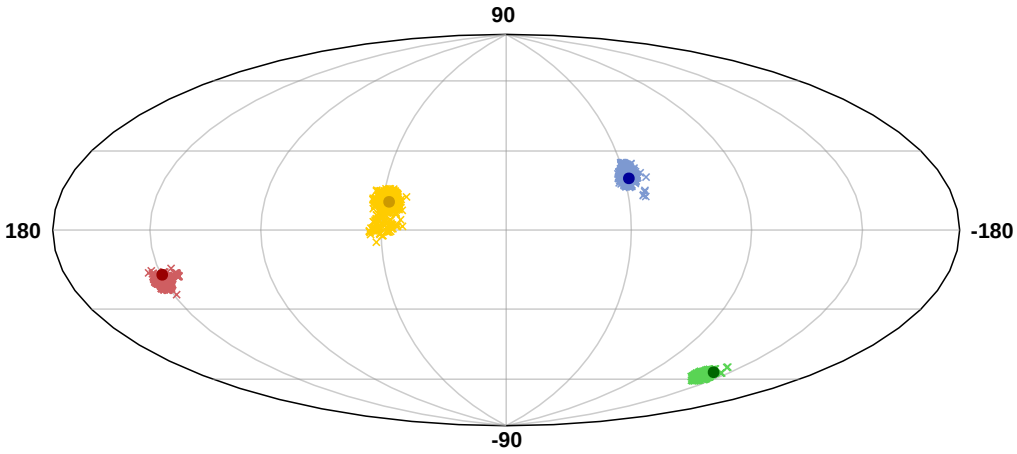

Figure 6.10: Illustration of arrival directions of cosmic-ray protons with the energy $10^{19.5}$ eV on Earth (crosses) originating from four sources in different directions marked with full circles of different colours. Only deflections in the Galactic magnetic field simulated with JF12Planck model are taken into account. The plot is in galactic coordinates.

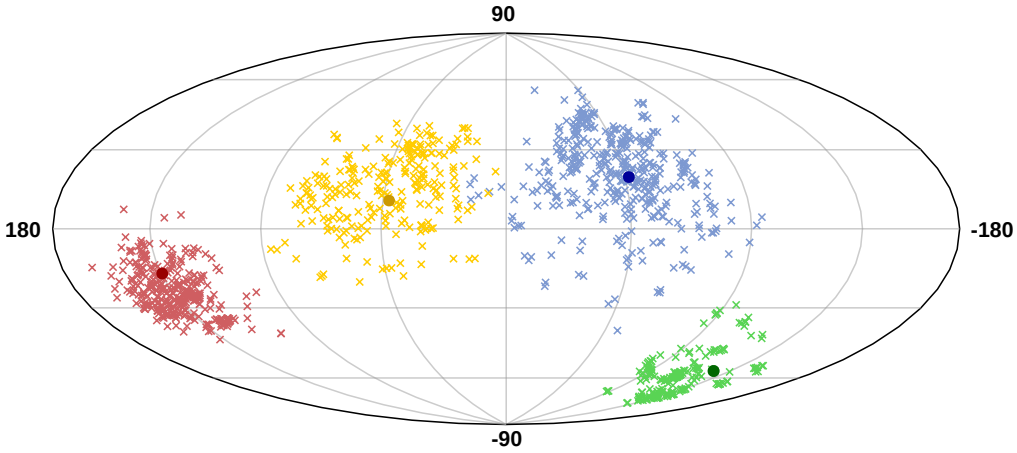

Figure 6.11: Same as Figure 6.10 but for nitrogen nuclei.

the nitrogen nuclei.

The identified solutions of the single-source features that could describe the shape of the energy spectrum and the mean mass composition on Earth presented in this chapter all exhibit a similar evolution of the mean mass composition on Earth with energy (see left panel of Figure 6.8). While at the lower energies at $10^{19.5}$ eV the mean mass composition

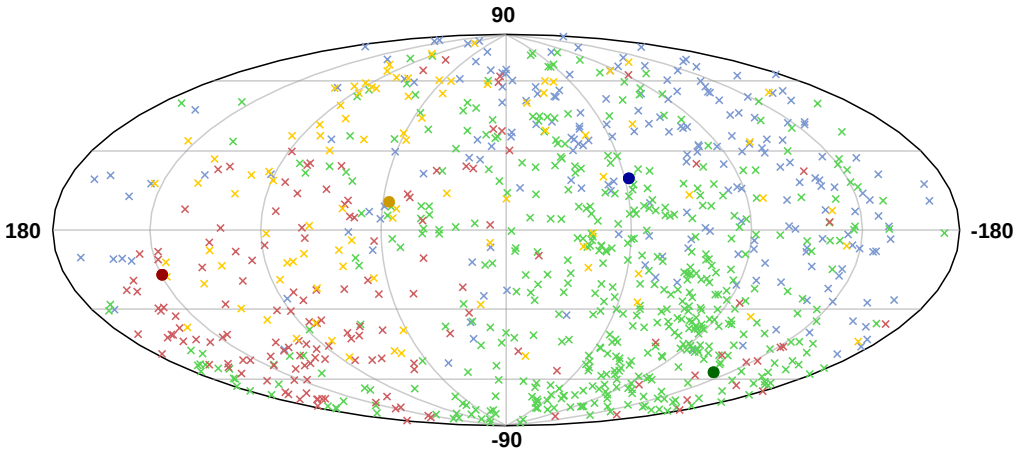

Figure 6.12: Same as Figure 6.10 but for iron nuclei.

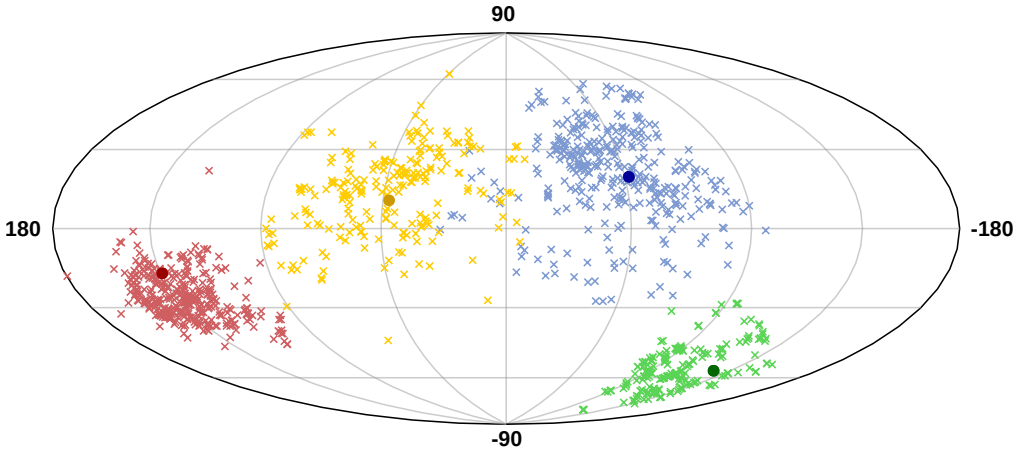

Figure 6.13: Same as Figure 6.10 but for iron nuclei with energies 10^{20} eV.

is close to nitrogen nuclei, at the highest energies, the mean mass is close to iron nuclei. Therefore, for anisotropies in the arrival directions of cosmic rays originating in a single source at energies $10^{19.5}$ eV, the arrival direction patterns similar to Figure 6.11 would be expected. In fact, similar arrival direction patterns would be also expected at the highest energies as the mean mass composition is close to iron nuclei. The corresponding rigidity of an iron nucleus with energy 10^{20} eV is $\sim 10^{18.6}$ V. The arrival directions of iron nuclei with energy 10^{20} eV after propagation in the JF12Planck model of the GMF are shown in Figure 6.13.

The anisotropies of the arrival directions are clearly visible for both nitrogen nuclei at energies $10^{19.5}$ eV and iron nuclei at energies 10^{20} eV. As there is no such clear clustering observed in the real data [112], the single source above $10^{19.5}$ eV is an unlikely scenario. However, a dominant source on an isotropic background, could still be an interesting hypothesis that could be checked in the future research.

Chapter 7

Detection of gamma rays

Gamma rays are high-energy photons that can be produced in various particle interactions. The gamma-ray astronomy focuses on observations of photons with energies above $\sim$ 100 keV. However, the energies of gamma rays can reach values as high as $\sim$ 1 PeV. In case of energies above 100 GeV, we are talking about very-high-energy (VHE) gamma rays. Gamma rays accompany many processes in the Universe and can be produced in electron-positron annihilation, neutral pion decay, synchrotron radiation etc.

A satellite detection of gamma rays is highly effective up to energies of $\sim$ 100 GeV. For higher energies, the space-based observation of gamma rays becomes highly inefficient because of the steeply decreasing gamma-ray flux. Similarly to the detection of cosmic rays, the detection of very high-energy gamma rays is done by ground-based observatories capable of compensating for the reduced flux by allowing detection areas up to $\sim$ km^2.

Ground-based detection of very-high-energy gamma rays employs two distinct techniques (see Figure 7.1):

- Imaging Atmospheric Cherenkov Telescopes (IACTs),
- Array of surface detectors detecting the secondary particles on the ground level.

Imaging Atmospheric Cherenkov Telescopes detect the Cherenkov light emitted during the air-shower development. The advantages of IACTs include their exceptional angular resolution (below $\sim 0.05^\circ$). However, their field of view is limited to less than $\sim 10^\circ$. Therefore, a precise alignment of the telescope with the target of interest is needed. Additionally, observing the Cherenkov light requires cloudless sky and good night-time conditions, limiting their duty cycle to approximately 15%. Current major observatories of gamma-rays utilizing the IACT technique include experiment H.E.S.S. [137] in the Southern hemisphere and experiments MAGIC [138] and VERITAS [139] in the Northern hemisphere. The Cherenkov Telescope Array (CTA) project [140], in two locations will cover both hemispheres and is currently under construction. CTA will be a next-generation facility for observing the very-high-energy gamma rays. The aim of CTA is to improve the sensitivity of energy by a factor five to twenty depending on the energy and it will also extend the observational energy range allowed by the IACT technique from about 20 GeV up to

300 TeV [141], ensuring a large discovery potential in the field of astronomy, astrophysics and fundamental physics.

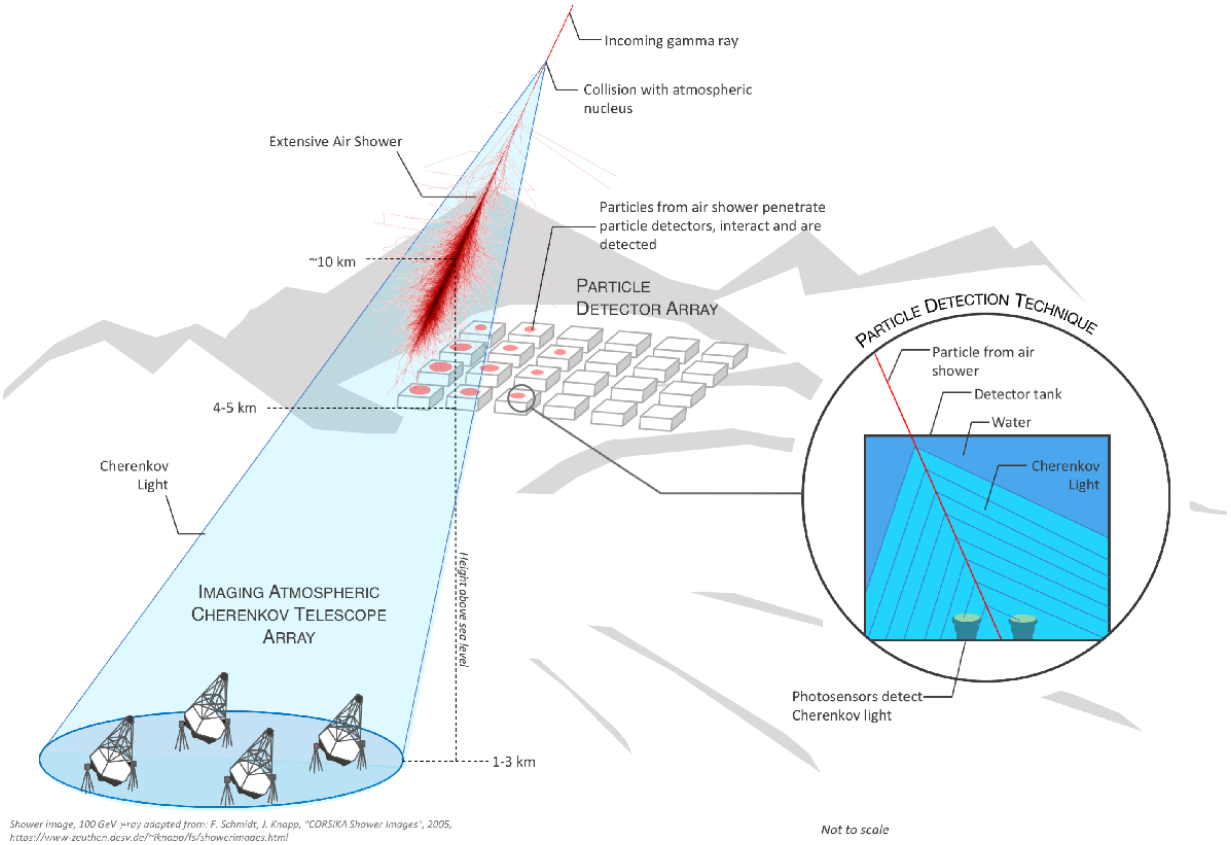

Figure 7.1: Illustration of the two different techniques for detecting gamma-induced air showers. Taken from [142].

The second technique is the use of an array of particle detectors that measure the secondary particles on the ground level. Compared to an EAS generated by UHECRs, the EAS induced by VHE gamma rays develop mainly higher in the atmosphere (above 4 km a.s.l.). Therefore, the observatories of gamma rays equipped with ground-particle detectors need to be placed at higher altitudes. These wide-field observatories allow for 100% duty cycle of observing large part of the sky (field of view $\sim 90°$) with a reasonable angular and energy resolution. Currently, large wide-field observatories of VHE gamma rays are only located in the Northern hemisphere, like High-Altitude Water Cherenkov Observatory (HAWC) [143] or LHAASO [144]. Therefore, large part of the sky is currently not covered by the wide-field detection technique.

The comparison of the typical performances of the two detection techniques is summarized in Table 7.1. One significant challenge for both detection methods is distinguishing between gamma-induced showers and showers induced by charged cosmic rays. In fact, more than 99% of air showers come from charged cosmic rays rather than from gamma rays [145].

7.1 The Southern Wide-field Gamma-ray Observatory

The Southern Wide-field Gamma-ray Observatory (SWGO) is a future gamma-ray ground-based observatory planned to be build in the Southern hemisphere, in South America [146]. The Observatory will detect extensive air showers generated by gamma-rays of energies from $\sim 100s$ of GeV to $\sim 100s$ of TeV with the aim to reach sensitivity up to the PeV region. The main goal of the SWGO is to provide a wide-field coverage of a large part of the southern sky which is now missing in the gamma-ray wide-field detection. This region is of great scientific interest as it contains large part of the Galactic plane, Galactic center and its surrounding as well as the southern Fermi bubble of our Galaxy. The proposed field of view of the SWGO is depicted in Figure 7.2, where the field of view of HAWC observatory [143] is shown for comparison.

Up to this date, scientists from 14 countries - Argentina, Brazil, Chile, China, Croatia, Czech Republic, Germany, Italy, Mexico, Peru, Portugal, South Korea, UK, USA - joined the collaboration. For the Czech Republic, the contributing institute is the Institute of Physics of the Czech Academy of Sciences and the Palacký University. The Czech team joined multiple tasks in the collaboration including the *Site selection task*, *Detector task* and *Simulation and analysis task*.

7.1.1 Design of the SWGO

The primary goal of the SWGO is to cover the sky in the Southern hemisphere, effectively complementing the already established wide-field observatories in the Northern hemisphere, such as HAWC and LHAASO, with the ultimate objective of achieving almost complete sky coverage. Moreover, a close collaboration with the southern part of CTA is expected, to which SWGO can provide alerts for transient objects.

The selection of the Observatory's location is of crucial importance to achieve its scientific objectives. To ensure a sufficient coverage of the southern sky, the optimal latitude for the observatory placement is between 20° and 30° south. The altitude of the SWGO influences the detector sensitivity and consequently the energy threshold and effective area. The current candidate sites are located in three countries; Argentina, Chile and Peru with

	IACT	Array of surface detectors
Field of view	3°-10°	90°
Energy range	30 GeV - 100s TeV	500 GeV - ∼1 PeV
Energy resolution	∼7%	60%-20%
Angular resolution	0.05°-0.02°	0.4°-0.1°
Duty cycle	10%-30%	>95%

Table 7.1: The typical performance of an IACT and an array of surface detectors for gamma-ray observations. Data taken from [146] and updated for LHAASO experiment [144].

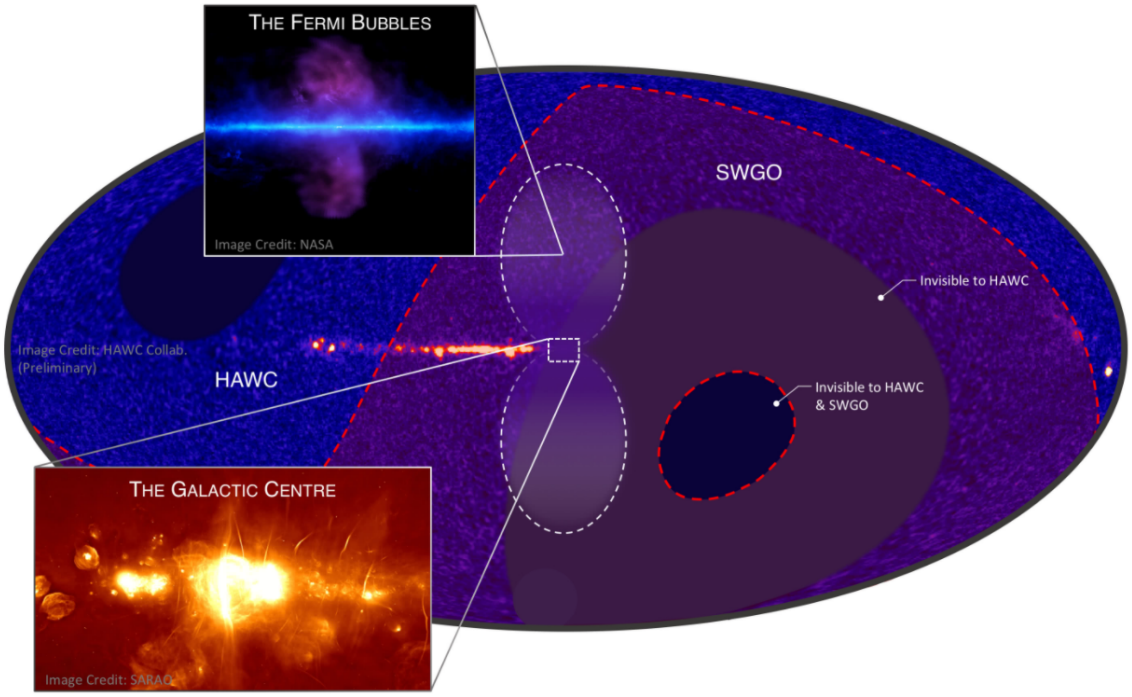

Figure 7.2: The visible sky by HAWC (blue) and SWGO (purple) experiments. Taken from [147].

altitudes ranging from $\sim$ 4400 m a.s.l. to $\sim$ 5000 m a.s.l. Building an observatory at such high altitudes also presents additional challenges, such as water access, existence of an infrastructure or work conditions at high altitudes. Furthermore, the detector and electronics needs to be designed in such a way to account for the harsh conditions at these altitudes including substantial variations in temperature, very low air pressure, strong solar irradiation or wind gusts.

As the SWGO is currently in its R&D phase, the design of the Observatory is now being studied and optimised. There are three basic ideas about the Observatory detection concept;

- **Tanks:** an array of plastic or steel water Cherenkov detectors (similar to the HAWC array).
- **Artificial pond:** detector units in bladders placed in one or multiple artificial ponds (similar to a part of LHAASO array).
- **Natural lake:** detector units in bladders placed in a natural high-altitude lake.

The three detection concepts and the placement of the units are currently all being evaluated. The schematics of these three options are illustrated in Figure 7.3.

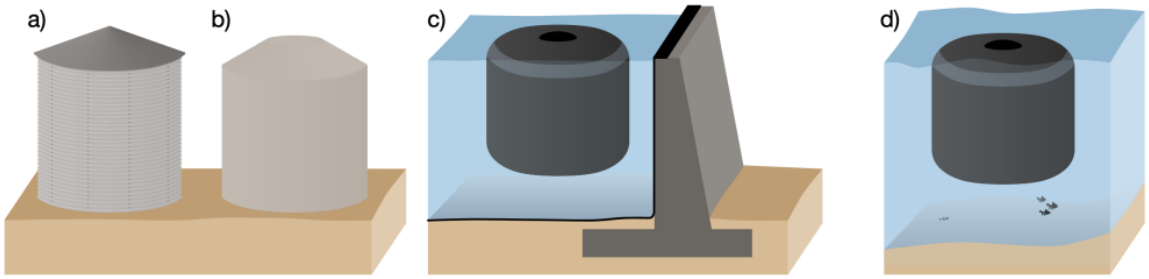

Figure 7.3: Visualisation of the three options of the detection technique at SWGO. a) and b) correspond to the array of surface detectors, c) represents the option of detectors placed in an artificial pond, and d) shows the option of placing detectors in a natural lake. Taken from [148].

Concerning the design of a single station, two main concepts of the detector units are being investigated, both capable of a good gamma-hadron separation; a double-layer detector [149], that allows tagging muons by the signal induced in the bottom layer of the detector due to shielding of the electromagnetic component by the upper part. The other concept of the detector unit is a multi-PMT single-layer detector [150], where the gamma-hadron separation is based on azimuthal asymmetries of the detected signal or azimuthal fluctuations of the signal [151]. However, it should be noted that the number of detector-unit designs that are being evaluated is quite large and the advantages and disadvantages of different concepts are yet to be determined.

The layout of the individual detector units needs to be optimised as well. For low-energy showers, the array of the detectors needs to have large fill factor ($FF \sim 80\%$) as the shower footprint is rather small. However, at the PeV energies, a sparse array with $FF \sim 1\% - 5\%$ should be sufficient. Therefore, the current ideas are of an array that is divided into multiple concentric zones with different FFs. An example of such an array is depicted in Figure 7.4. The array consist of two zones with radius 160 m and 300 m and FFs 80% and 5%, respectively. In the figure, the triggered detectors are shown for two gamma-ray showers falling into the array are shown for a 0.6 TeV (left panel) and 14 TeV energy (right panel) of the primary gamma-ray.

7.1.2 Science case of the SWGO

SWGO aspires to be a multi-purpose experiment that can cover a wide range of scientific topics. The main scientific goals can be divided into four main areas; unveiling galactic particle accelerators, monitoring the transient sky at very high energies, probing particle physics beyond the Standard Model, and the characterization of the cosmic-ray flux [146]. The scientific scope of the Observatory is very large and its full description is out of the

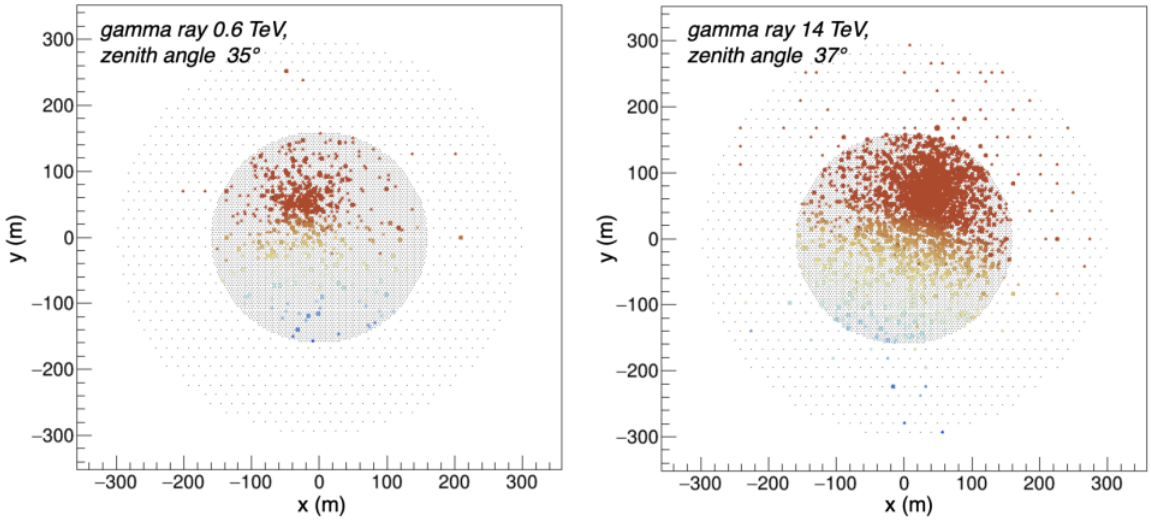

Figure 7.4: An example of the array concept for the SWGO observatory with a 0.6 TeV (left) and 14 TeV (right) event falling inside the inner array. The colour represents the arrival time of the signal in a given station and the size of the marker corresponds to the amplitude of the measured signal in a given detector unit. Taken from [148].

scope of this thesis. However, few selected interesting areas of the future science with SWGO are described in the following paragraphs.

Pevatrons: The observations of VHE gamma rays from the Galactic center and Galactic plane allow to search for sources of very high energy electrons, positrons and cosmic rays. The so-called *pevatrons* are of special importance as these sources are capable to accelerate cosmic rays up to the PeV energies [152]. Emission of PeV cosmic rays should be accompanied by production of VHE gamma rays that originate in decays of neutral pions that are produced in interactions of cosmic rays with interstellar matter. The detection of PeV gamma-rays was previously announced by the LHAASO experiment [153].

Transient objects: Advantage of wide-field gamma-ray observatories is their high duty cycle compared to the IACT experiments. This allows the detection and observation of transient objects including AGNs [154], gamma-ray bursts (GRBs) [155, 156], fast radio bursts (FRBs)[1], X-ray binaries and other transient sources. SWGO will be able to observe known VHE blazars and conduct an unbiased survey of the large part of the southern sky to detect also new VHE blazars. These observations might serve for measurements of the intergalactic magnetic field. The detection of possible GRBs in the VHE regime will also be possible and allow their multi-messenger detection together with gravitational waves and low-energy photons.

Physics beyond the Standard model: One of the main scientific goals of SWGO is the search for physics beyond the Standard model. This includes the search for dark matter, namely Weakly Interacting Massive Particles (WIMPs) from annihilation/decay

[1]Up to this day there was no gamma-ray counterpart detected for the known FRBs [157].

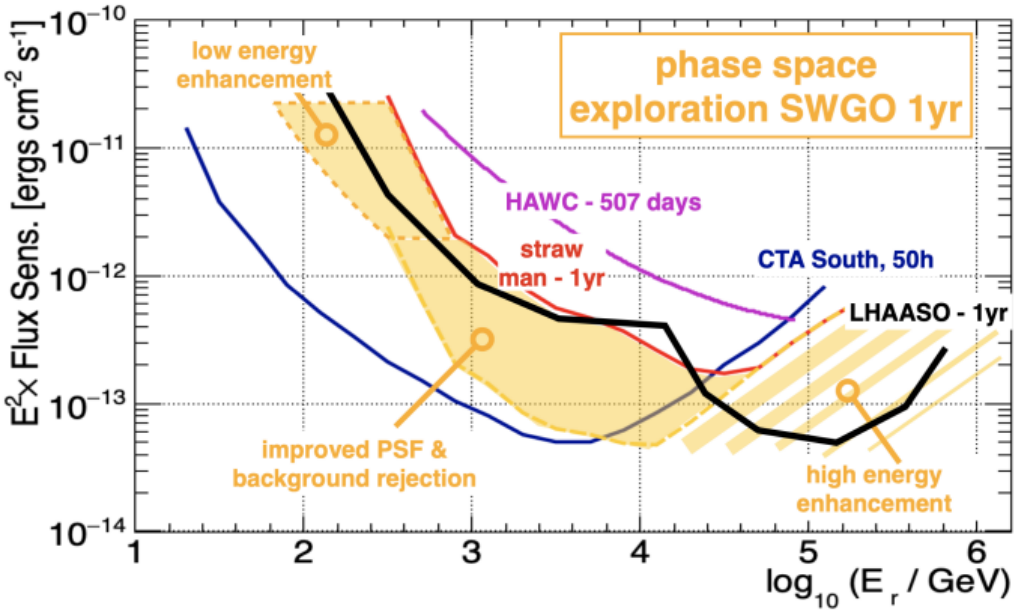

Figure 7.5: Estimated sensitivity of the future SWGO observatory obtained for the straw-man design compared to sensitivities of HAWC, LHAASO and CTA. Taken from [148].

signals in the form of VHE gamma-rays [158, 159]. SWGO will also allow searches for primordial black holes, Lorentz-invariance violations or axion-like particles, for more detail see [146].

Cosmic rays: Last but not least, SWGO will be capable of measuring properties of galactic cosmic rays from TeV energies up to above PeV energies. This includes the energy spectrum and its features around the *knee* region, anisotropies in the arrival directions of cosmic rays and their mass composition [160, 161]. A precise knowledge about the composition of cosmic rays would allow the estimation of the maximum acceleration energy of Galactic sources and size of large-scale anisotropy as a function of rigidity.

The estimation on the SWGO sensitivity is shown in Figure 7.5 as a function of the gamma-ray energy compared to the sensitivities of other experiments. This preliminary sensitivity plot was estimated for a "straw-man" design of the Observatory. The sensitivity is estimated for the case of a steady point source at a zenith angle of 20 ◦ and a daily observational time of 6 hours [146]. However, the new concepts that are being studied could perform even better.

7.2 Simulations of detector responses for the SWGO

Part of my work during doctoral studies was devoted to the studies of the detector design for the future gamma-ray observatory SWGO. This technical and software-development work supplements the physics analysis presented in the first part of the thesis. This section is divided into two subsections. Subsection 7.2.1 presents a study that was done in order to verify the suitability of the simulation software HAWCSim [143] that is being used by the SWGO collaboration for simulations of the detector responses by comparison with the simulation code LATTESSim [162]. Parts of the text in this chapter are taken from an internal note for the SWGO collaboration [163]. Subsection 7.2.2 then shows the results of the detector performance at the single-particle level of a *Mercedes* water Cherenkov detector that were published in [164].

7.2.1 Simulation of the detector response in two softwares

In this section, a project with the aim to verify the suitability of the simulation software HAWCSim [143] that is being used by the SWGO collaboration for the simulations of the detector responses is presented. This software was originally designed for the HAWC. Even though HAWC is an experiment focused on the gamma-ray detection as well, the detectors of the HAWC experiment are 4 meters high, and 7.3 meters in diameter water Cherenkov detectors with black walls [143], while the detectors proposed for the SWGO experiment are expected to be smaller than the HAWC tanks. Moreover, at least some parts of the WCDs for SWGO are intended to have a Tyvek reflective lining. For that reason, different properties of the materials are crucial for each experiment, and it is essential to check the suitability of HAWC code as a framework to evaluate different detector concepts for SWGO.

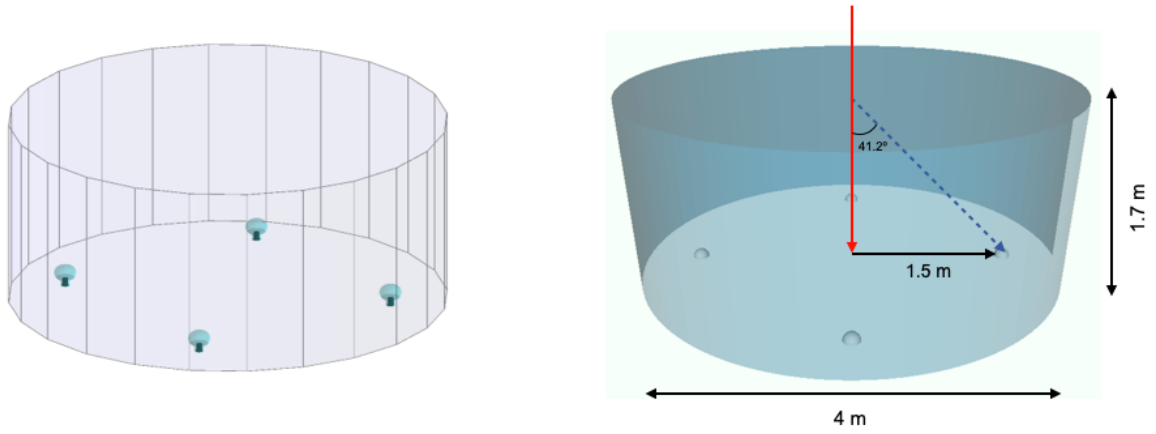

Figure 7.6: Visualisation of the water Cherenkov detector from HAWCSim (left, made in HAWCSim) and LATTESSim (right, taken from [165]).

In order to check the suitability of the HAWCsim software for SWGO purposes, we are performing double-checks of the simulation output using two different simulation codes. The result of the simulated detector responses from HAWCsim are compared with the output obtained from the simulation framework used for the LATTES experiment [162] - LATTESsim[2]. Both simulation codes are based on the GEANT4 simulation toolkit [166–168].

For the comparison, we use simulations of single detector response generated by 2 GeV vertical muons. The detector concepts in both simulation codes are made as similar as possible to suppress differences in the output caused by the geometry effects, material properties and other adjustable features.

The used detector design is a single-layer WCD with the water height of 1.7 m and 2 m radius [150]. Four 8-inch PMTs are placed equidistantly on the bottom of the tank in a circle of 150 cm radius around the tank centre. The visualisation of the WCD is shown in Figure 7.6 in HAWCsim (left) and LATTESsim (right). The WCD inner surface is completely covered with Tyvek.

In order to be able to distinguish between detector properties and geometrical effects, the 2 GeV vertical muons were injected in two modes:

1. muons placed in the centre of the WCD,

2. uniformly distributed muons over the tank surface.

In both cases, muons are injected 10 cm above the top of the tank surface. In the first mode, a total number of 10,000 particles injected to the centre of the tank at coordinates $(x, y, z) = (0, 0, 180)$ cm with energy 2 GeV were simulated in HAWCsim and LATTESsim. In the second mode with uniform distribution of muons, there were 10,000 injected muons simulated in HAWCsim and 100,000 injected muons simulated in LATTESsim.

Centered muons

The first mode of simulations injects the vertical 2 GeV muons 10 cm above the tank surface in the center of the tank. The simulations of the detector response were done in the two softwares, HAWCsim and LATTESsim, which allows the comparison of the distribution of the number of photo-electrons created for individual muons and the average time-trace of the signal created. This comparison can be seen in Figure 7.7. The left panel of Figure 7.7 shows a high agreement of the two outputs for the distribution of the signal strength. The average time traces obtained from HAWCsim[3] and LATTESsim depicted in the right panel of Figure 7.7 show similar behaviour. There is a strong first peak corresponding to

[2]The outputs from simulations performed in LATTESsim were provided by Bernardo Tomé and Ruben Conceição, LIP - Laboratório de Instrumentação e Física Experimental de Partículas, Portugal.

[3]The time trace obtained from HAWCsim simulation is shifted by −8 ns. This time shift corresponds to the time shift needed to align the start time of the signal in both simulations when the uniform distribution of muons is used. This time offset is caused by a predefined start time in the HAWCsim code and has no physical meaning.

the first direct light collected by the PMTs, followed by a smaller peak appearing about 15 ns later, due to the light reflected upwards at the bottom and then downwards from the top surface, thus travelling at least 340 cm. The width of the peak is wider in HAWCSIM than in LATTESSIM. At late times, the signal decreases exponentially. The output from HAWCSIM shows a slightly weaker signal at late times, however, the signal in the first and second peak is a bit stronger compared to LATTESSIM.

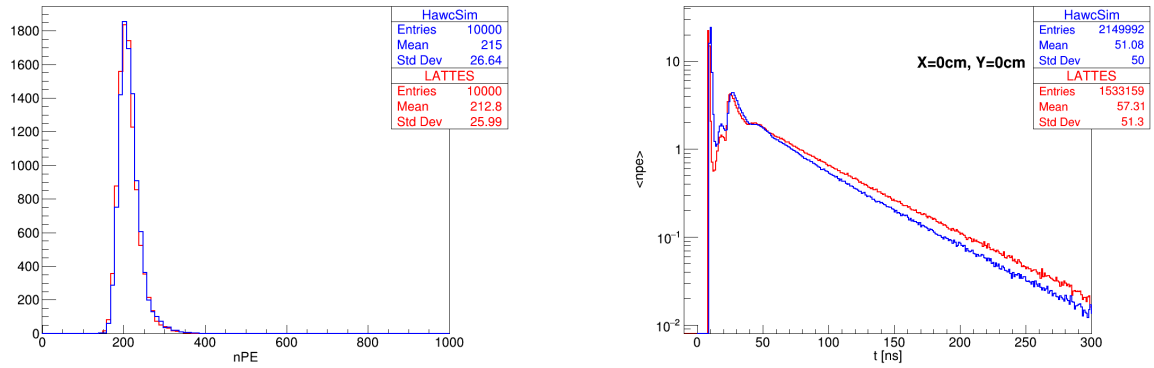

(a) Signal strength distribution.

(b) Average time trace.

Figure 7.7: Signal strength distribution (left) and average time trace (right) obtained from simulations performed in HAWCSIM and LATTESSIM using vertical centred 2 GeV muons. Figures taken from my internal publication [163].

Uniformly distributed vertical muons

In the second mode, the vertical 2 GeV muons are injected uniformly over the detector surface. We simulate 10,000 muons with HAWCSIM and 100,000 muons with LATTESSIM.

Signal strength and timing: We compare the signal strength and the average time-trace as in the previous mode for central muons. The distribution of the signal generated by the detector simulated with HAWCSIM and LATTESSIM is shown in the left panel of Figure 7.8. We can see, that the mean of the distribution of the signal strength obtained from LATTESSIM is smaller by $\sim 15\,\%$ compared to the output from HAWCSIM, which could be caused by different implementation of PMTs in the two codes.

The right panel of Figure 7.8 shows the average time trace of detected photoelectrons from individual simulations. The time trace obtained from HAWCSIM is again shifted by $-8\,\text{ns}$ in order to align the start times of the signals from both simulations. Even though LATTESSIM produces more photo-electrons at late times, the deficit of photo-electrons in the first and second peak compared to HAWCSIM explains the on average 15% weaker signal that is seen in the left panel of Figure 7.8.

Spatial distribution of the signal: Another comparison of the results obtained from HAWCSIM and LATTESSIM softwares can be done by looking into the spatial

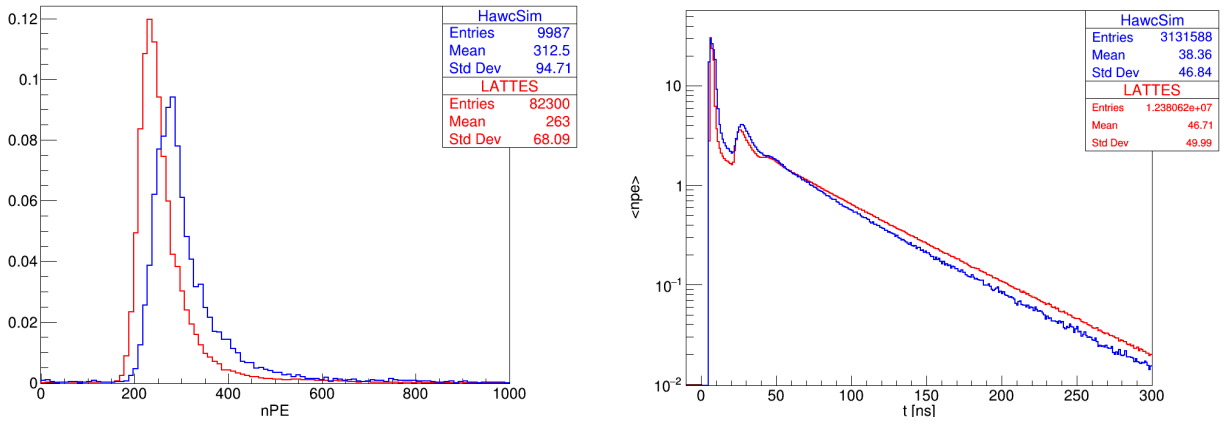

Figure 7.8: *Left*: Distribution of detected photoelectrons for uniformly distributed vertical 2 GeV muons for simulations performed in HAWCSIM and LATTESSIM code. *Right*:Time trace seen by the detector of uniformly distributed vertical 2 GeV muons for simulations performed in HAWCSIM and LATTESSIM. Figures taken from my internal publication [163].

distribution of the signal. The average signal strength generated by a 2 GeV vertical muon hitting the tank in a given (x, y) location is shown in Figure 7.9 for both HAWCSIM and LATTESSIM. No time cut for detected photoelectrons is applied in this plot. The strongest signal is obtained for a muon in a close vicinity of one of the PMTs, while in other locations of the incident muon the generated signal is weaker but quite uniform.

To see the discrepancies between the two outputs, we plot the ratio of the signal seen by LATTESSIM and HAWCSIM, shown in the left panel of Figure 7.10. The distribution of the ratios in individual (x, y) bins is plotted in the right panel of Figure 7.10. Both direct and reflected light from the Tyvek lining of the WCD is taken into account in these plots. Generally, LATTESSIM generates slightly weaker signal when compared to HAWCSIM.

Dividing the signal into multiple time windows a sufficient distinction of the direct and diffused light can be achieved. We divided the signal into three different time windows; $t < t_0 + 5\,\text{ns}$, $t < t_0 + 10\,\text{ns}$ and $t \in (t_0 + 10\,\text{ns}, t_0 + 40\,\text{ns})$, where $t_0 = 5\,\text{ns}$ represents the start time of the signal. The illustration of the individual time windows and the signal within them is visualised in Figure 7.11.

The ratio of the signal detected by LATTESSIM and HAWCSIM in the earliest time window of $t < t_0 + 5\,\text{ns}$ is depicted in Figure 7.12 together with the distribution of the ratios in individual spatial bins. The mean ratio of the signals obtained by the two simulation software shows that LATTESSIM gives about 30% weaker signal compared to HAWCSIM. However, there is a visible structure where the signal obtained from LATTESSIM is stronger, with the biggest difference in the centre of the WCD having twice the signal compared to HAWCSIM. This large difference between the signals obtained in the centre of the tank is caused by taking into account different parts of the first peak in the signal for centred muons. The time shift applied here fixes the start times in the overall time trace for uniformly distributed muons. However, taking into account only centred muons,

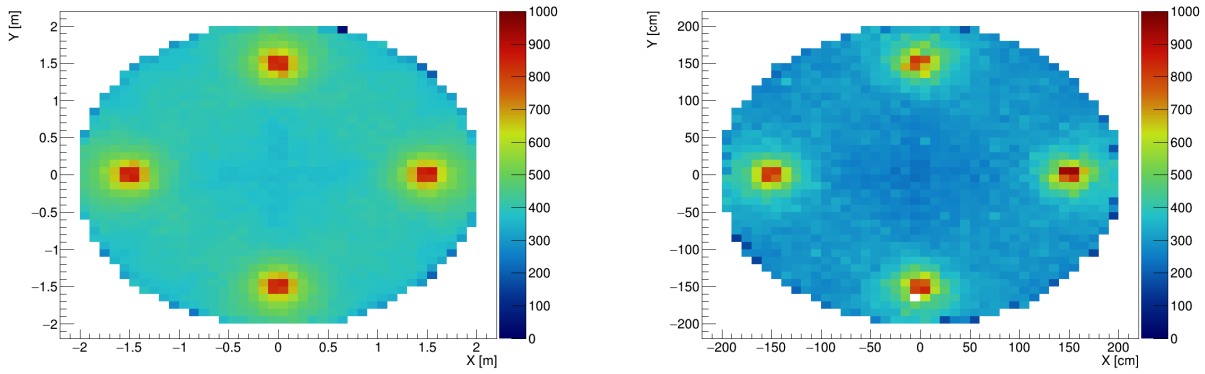

(a) LATTESSIM (b) HAWCSIM

Figure 7.9: Average number of photoelectrons seen by the detector for vertical 2 GeV muon injected at given coordinates. Figures taken from my internal publication [163].

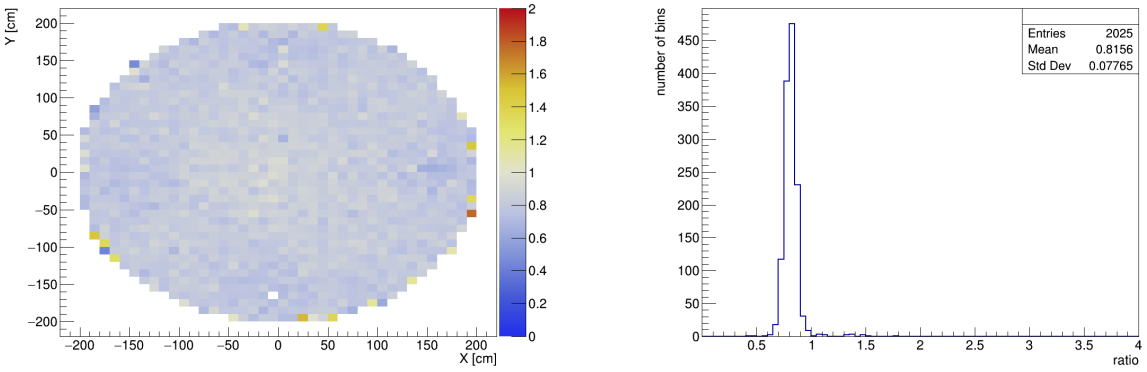

Figure 7.10: *Left:* Ratio of the average signal generated by a 2 GeV vertical muon injected at given coordinates of the output from LATTESSIM and HAWCSIM. *Right:* The distribution of the ratios in individual spatial bins. Figures taken from my internal publication [163].

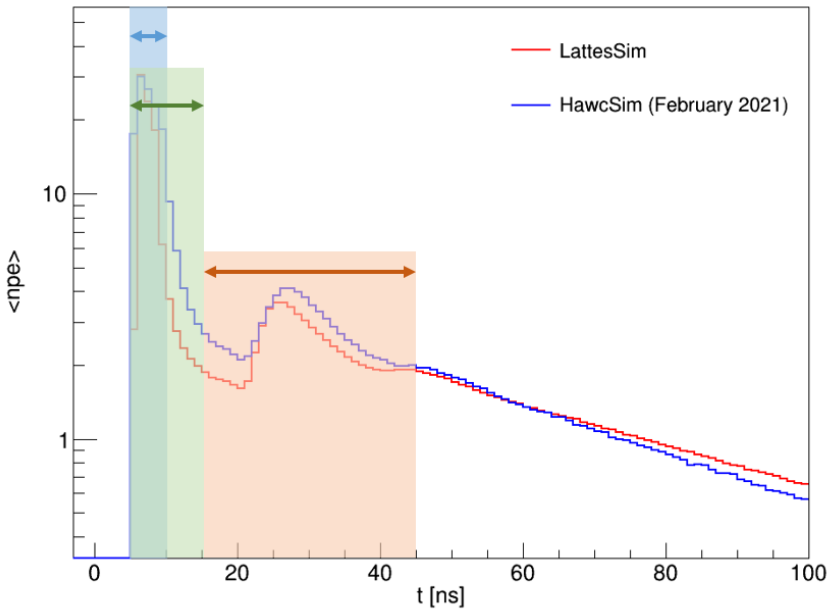

Figure 7.11: Illustration of the different selected time windows of the signal by coloured boxes for both simulation softwares. The $t < t_0 + 5\,\text{ns}$ window is shown in blue box, the $t < t_0 + 10\,\text{ns}$ window is represented in green box and the $t \in (t_0 + 10\,\text{ns}, t_0 + 40\,\text{ns})$ time window is shown in orange box. Figure taken from my internal publication [163].

this $-8\,\text{ns}$ shift in the time trace does not align the start times and the time trace from HAWCsim is delayed by $\sim 1\,\text{ns}$ compared to LATTESsim, which subsequently leads to this high ratio of the signal obtained from LATTESsim and HAWCsim.

Nevertheless, this structure disappears when taking the signal from a larger time window. In the case of the signal collected from a time window of $t < t_0 + 10\,\text{ns}$, the spatial distribution of the detected signal ratios gets more uniform over the tank surface as can be seen in the left panel of Figure 7.13. Accordingly, the distribution of the ratios of the two signals obtained in individual spatial bins gets narrower, and it is centred around ratio of ~ 0.66, see the right panel of Figure 7.13.

Finally, comparing the signal from a time window $t \in (t_0 + 10\,\text{ns}, t_0 + 40\,\text{ns})$, that represents mostly the diffused light on the WCD Tyvek, shows a good agreement between the two simulations. The distribution of the ratio of spatial signal obtained by LATTESsim and HAWCsim and the distribution of these ratios in individual XY bins is depicted in Figure 7.14. In this time window of diffuse light, the signal generated by LATTESsim is slightly weaker with the mean ratio of approximately 90%.

Overall, these two simulation software outputs are in good agreement and the described discrepancies can be explained by different implementation of PMTs in the two software codes and slightly different material properties settings. HAWCsim software generates a wider first peak in the time trace leading to a higher total number of generated photoelectrons by a single particle. Moreover, the left panel of Figure 7.10 shows a high level of

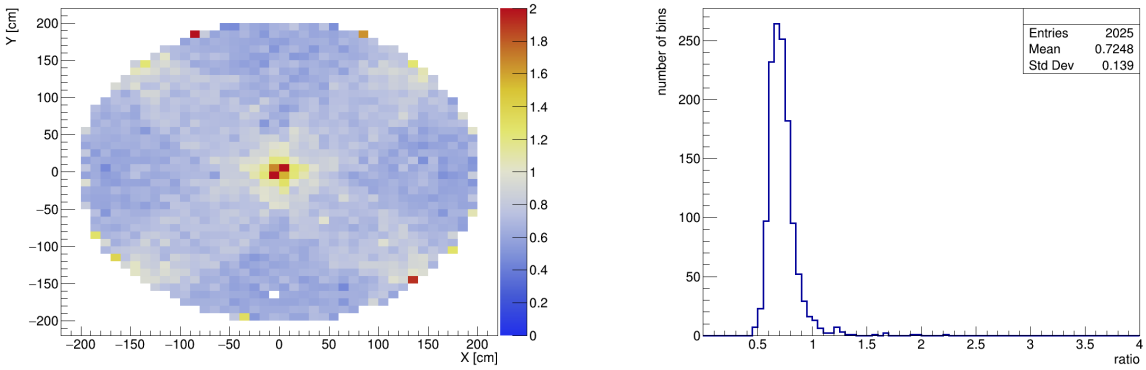

Figure 7.12: *Left:* Ratio of the average signal generated by a 2 GeV vertical muon injected at given coordinates of the output from LATTESSIM and HAWCSIM for photo-electrons detected within time window $t < t_0 + 5\,\text{ns}$. *Right:* The distribution of the ratios in individual spatial bins for signal detected within $t < t_0 + 5\,\text{ns}$. Figures taken from my internal publication [163].

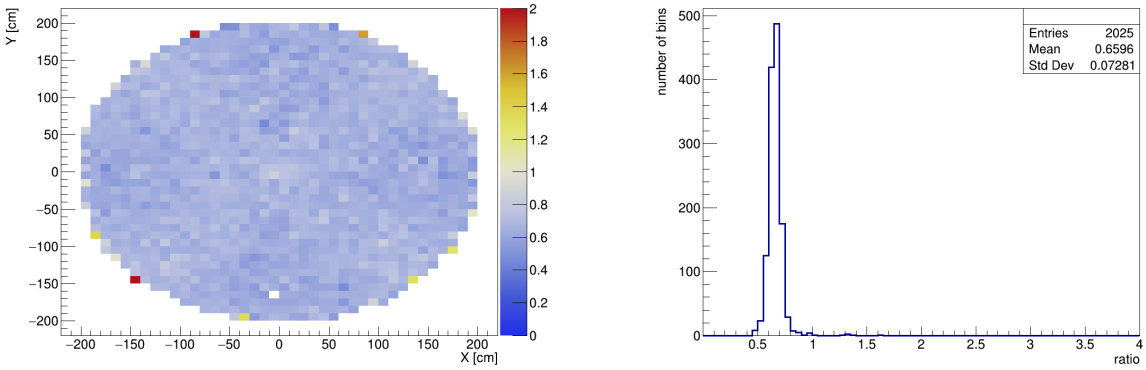

Figure 7.13: Same as Figure 7.12 but for $t < t_0 + 10\,\text{ns}$. Figures taken from my internal publication [163].

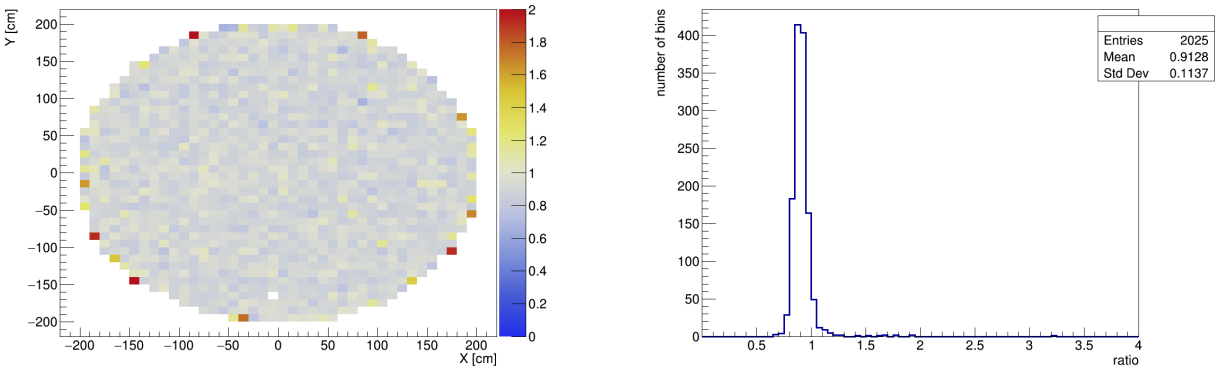

Figure 7.14: Same as Figure 7.12 but for $t \in (t_0 + 10\,\text{ns}, t_0 + 40\,\text{ns})$. Figures taken from my internal publication [163].

uniformity of the ratio of the signal generated from HAWCSIM and LATTESSIM for vertically injected particles over the whole surface of the WCD. This work therefore verified the consistency between the two simulation software and the possibility to use the HAWCSIM software for the purposes of the SWGO experiment to study small-tank designs.

7.2.2 Mercedes water Cherenkov detector studies

A new concept of a small water Cherenkov detector for gamma-ray observations was proposed in [165, 169]. Modified concept of this detector, called *Mercedes* water Cherenkov detector, and its performance was presented in [164]. In a collaboration with the authors of [165, 169], I performed simulations of the single detector response of the *Mercedes* WCD using the simulation software HAWCSIM in a similar manner as was presented in the previous section.

The *Mercedes* water Cherenkov detector is a cylindrical single-layer detector with radius of 2 m and water height of 1.7 m. Three 8" PMTs are placed on the bottom of the tank with a 120° star configuration [164] as shown in Figure 7.15. The placement of the three PMTs is chosen in such a way that the distance between two PMTs is equal to twice the radius of the Cherenkov cone of vertical muons. The inner surface of the WCD is made of reflective material for light diffusion. Note, that this concept, including the dimensions of the tank, is not yet optimised.

Induced photo-electrons with respect to energy: To investigate the response of the *Mercedes* WCD to photons of different energy, I simulated response of the *Mercedes* WCD for single photons of energies from 1 MeV up to 10^5 MeV in discrete steps in energy. For each energy, 10,000 vertical photons were simulated and injected uniformly over the WCD surface. The evolution of the number of induced photo-electrons with energy of the incident photon is depicted in Figure 7.16. The signal is the sum of the signals collected from all three PMTs and no cut on the timing of the photo-electrons is performed. Due to the small dimensions and the number of PMTs the *Mercedes* WCD is sensitive even to

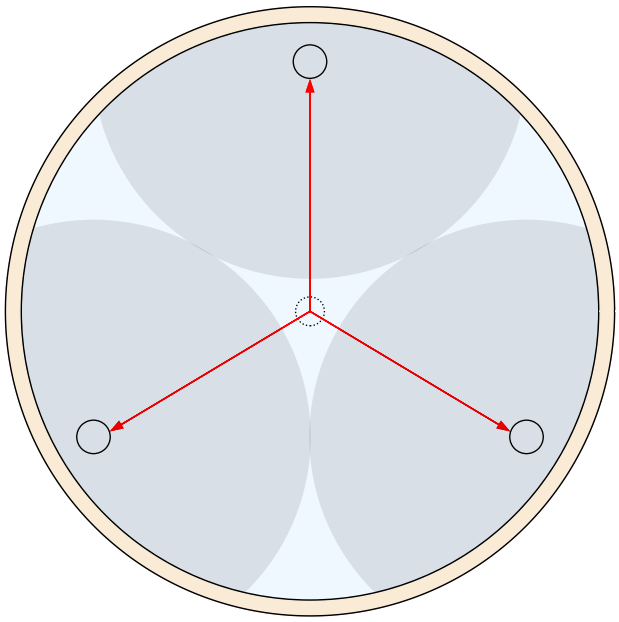

Figure 7.15: Top view of the *Mercedes* water Cherenkov detector with the placement of the PMTs. Taken from my publication [164].

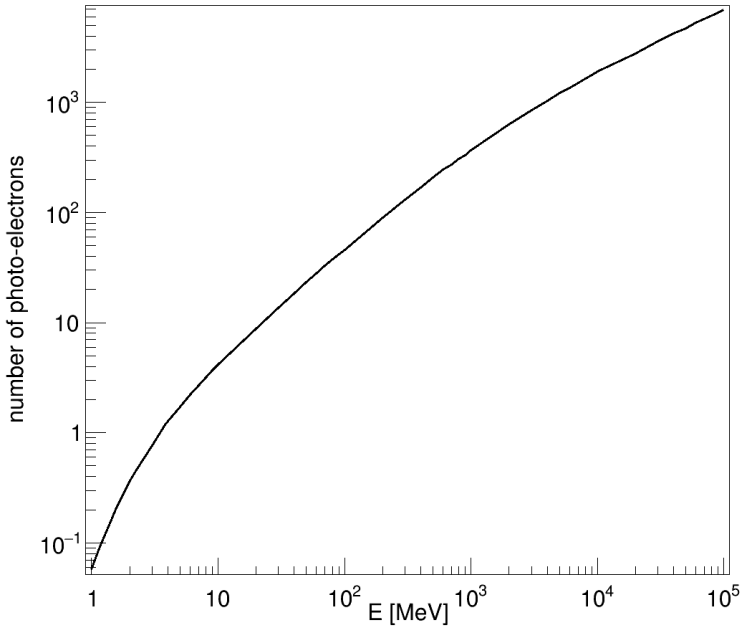

Figure 7.16: Average number of photo-electrons induced in the *Mercedes* WCD as a function of the energy of the incident photon.

low-energy photons. The induced signal increases with the energy of the incident photon up to the highest energies. However, no saturation of the signal is taken into account here.

Response to vertical and inclined muons: The response of the WCD to muons was studied for 2 GeV vertical and inclined ($\theta = 20°$) muons that were injected uniformly over the WCD surface. The distribution of the signal (number of photo-electrons) for vertical and inclined muons is shown in Figure 7.17. The plateau that can be seen for the case of inclined muons with small signal is caused by the clipping muons, that have a shorter path inside the detector and therefore the induced signal from such particles is rather small.

The average time trace of the induced PMT signal for vertical and inclined 2 GeV muons and vertical 100 MeV photons is shown in Figure 7.18. For both types of particles, a strong first peak of the direct light is well defined, having the width of few ns. Moreover, the time trace of the signal for vertical and inclined muons are almost identical, which enables a good shower geometry reconstruction [162].

The results seen in Figure 7.16, Figure 7.17 and Figure 7.18 support that the *Mercedes* WCD should be sensitive to photons and electrons from low-energy air showers and has an absolute signal for muons that is stronger than the induced signal from electromagnetic particles. Such properties of the detector are crucial for future gamma/hadron separation.

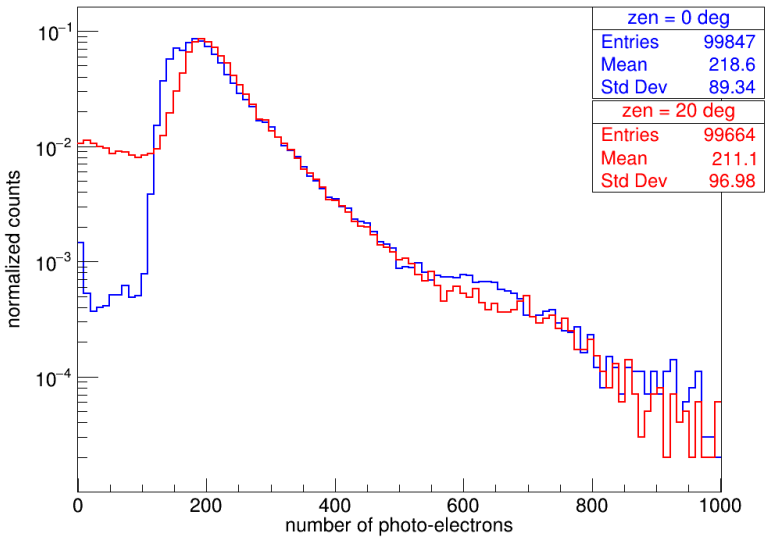

Figure 7.17: Distribution of the total signal induced in the *Mercedes* WCD for 2 GeV single vertical (blue) and inclined (red) muons.

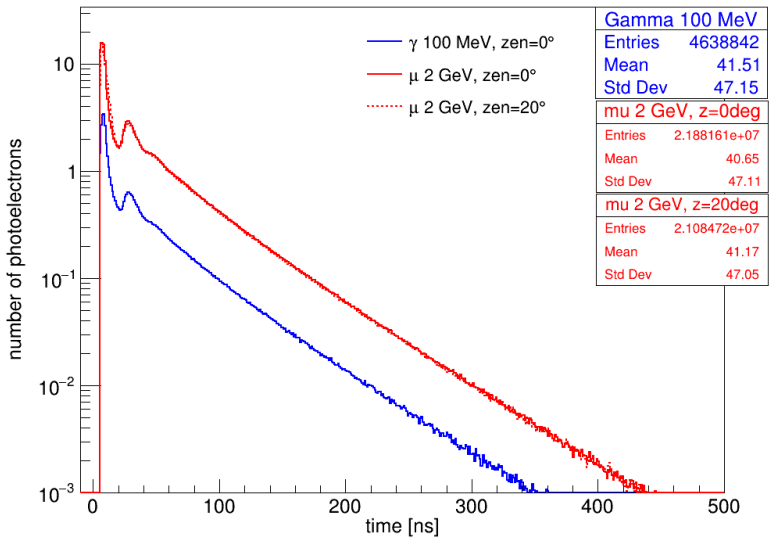

Figure 7.18: Average time trace of the signal in *Mercedes* WCD for vertical 100 MeV gammas (blue) and 2 GeV vertical (full red line) and inclined (dashed red line) muons.

7.3 Amplification of the photon intensity of sources in binary systems

During my doctoral studies I also participated in a research concerning the amplification regimes of intensity of sources in the vicinity of compact objects. This can be, in principal, applied for the amplification of the gamma-ray flux for sources in a close vicinity of a compact object. Binary systems are also one of the astrophysical systems that will be explored by the SWGO as part of the Science case goals (see Section 7.1.2). This work [170] introduces the exact fully relativistic solutions of the extreme amplification regime of point-like and small-sized sources located in a close vicinity of the caustic line[4] at a short distance from a Schwarzschild black hole gravitational lens. My part of the research was the proposal of approximate relations to these fully general relativistic calculations of the amplification of the primary and secondary amplification peaks of the lensed source and the time delay between the first two images in primary and secondary amplification peaks, that can be used as an alternative to the usual full numerical integration approach, which is very time consuming.

Let us assume a binary system with a compact object of mass M and a source located at a small radius R to the compact object and a close angular distance ψ from the caustic line, either behind or in front of the compact object. Such constellation of the system with $R < 200M$ leads to the extreme lensing regime, where the weak deflection limit (WDL) calculations [171] fail to describe it properly and a fully general relativistic (FGR)

[4]The caustic line is the line of sight connecting the observer and the centre of the lens (compact object).

description of such systems is needed.

The amplification of the intensity of radiation coming from a point source and propagating through a gravitational field can be written as [170]

$$I = \mu g^4 I_0, \tag{7.1}$$

where I_0 is the intensity, μ is the magnification factor and g is the frequency shift factor. The amplification of the intensity is therefore $\mathcal{M} = \mu g^4$, consisting of the geometrical amplification given by the magnification factor μ and the energy amplification g^4.

The geometry of the lensing of photons from a source in the vicinity of a compact object is depicted in Figure 7.19, showing the trajectories of a non-lensed and lensed rays. In case of the Schwarzschild space time, there is an infinite number of photon trajectories connecting the observer and the source, thus an infinite number of images of the source is created [172]. In case of very small angular separation of the source from the caustic line ψ and in a close vicinity to the lens, the amplification reaches extremely high values, for details see [170].

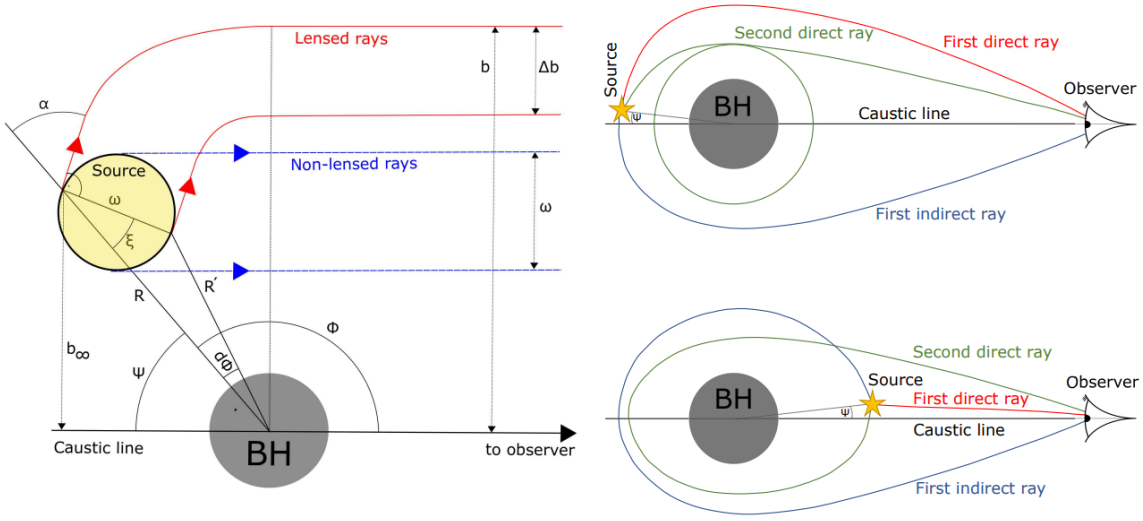

Figure 7.19: *Left:* The geometry of the lensing of the source in the vicinity of a compact object. *Right:* Illustration of the first three rays lensed from a source with a small angular separation from the caustic line ψ behind the lens (top) and in front of the lens (bottom). Taken from my publication [170].

The magnification factor μ depends on the distance of the source R and the change of the angular coordinate with respect to the non-lensed ray $\Delta\phi$, see Figure 7.19. The amplification can be calculated using the WDL when large distances of the source and the lens and small angular coordinate $\beta = \psi R/D_s$, where D_s is the distance to the observer, are assumed. However, for close sources in the regime of extreme amplifications, the WDL approximation needs to be replaced by the FGR numerical integration of the trajectories.

The primary amplification peak appears for a source located close to the caustic line behind the lens and the main contribution to the resulting total intensity comes from the first two images, first direct and first indirect image. The amplification of the primary peak of a static source located behind the Schwarzschild lens, under the assumption of small distances and small angular separation $\psi \leq 0.01$, can be described by a simple correction factor to the WDL approximation formula as

$$\mathcal{M}_{a\pm} = C_1(R, M)\mu_{s\pm}, \tag{7.2}$$

where $\mu_{s\pm}$ is the magnification factor of the first two images under the WDL approximation and

$$C_1(R, M) = \left(1 - \left(\frac{2M}{R}\right)^{0.85}\right)^{1.35} \tag{7.3}$$

is the newly introduced correction factor that describes the FGR numerical calculations with accuracy better than 1.6% for $R > 6M$ and better than 6% for $R > 3M$. For $R \to \infty$ the correction factor approaches one and the amplification is then described solely by the WDL approximation.

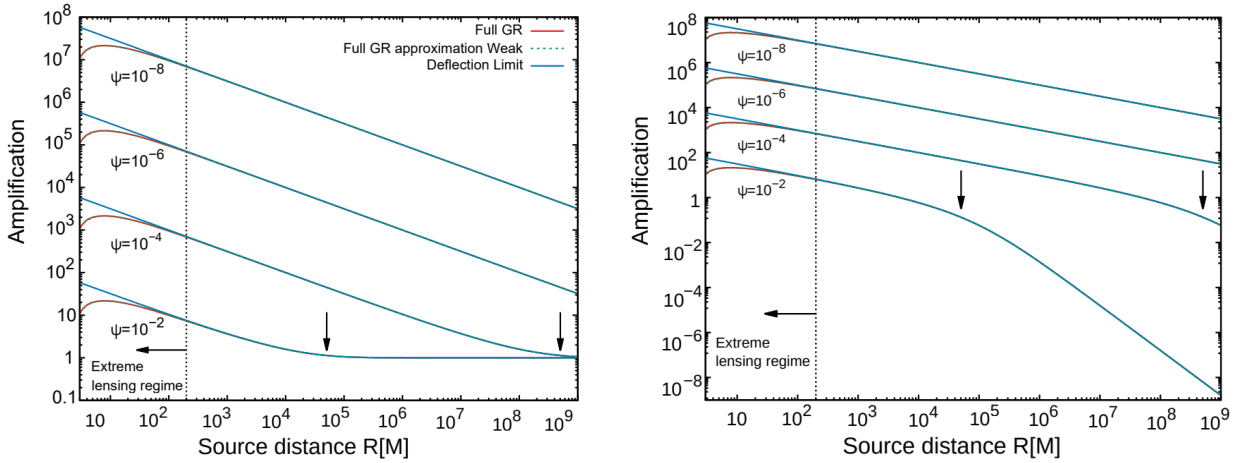

Figure 7.20: Primary amplification peak. Amplification of the first direct (left) and first indirect (right) image with respect to the distance of the source to the lens for multiple separation angles from the caustic line ψ for the exact FGR, FGR approximation (Equation (7.2)) and the WDL approximation (deflection limit). Taken from my publication [170].

The primary amplification peak for the first direct and first indirect image with respect to the distance of the source and lens for multiple separation angles is shown in Figure 7.20 for the exact FGR approach, FGR approximation (Equation (7.2)) WDL approximation and the WDL approximation. In the regime of the extreme amplification ($R < 200M$), the FGR approximation largely outperforms the WDL approximation.

The differential time delay between the first two images forming the primary amplification peak for small angular separation $\psi < 0.01$ can be approximated with relation

$$\Delta t = \left(4\sqrt{R/M} + 3\right) M\psi \tag{7.4}$$

and the accuracy with respect to the exact FGR approach is better than 1% and 3% for $R > 6M$ and $R > 3M$, respectively. The exact FGR and FGR approximation of the time delay is depicted in the left panel of Figure 7.21.

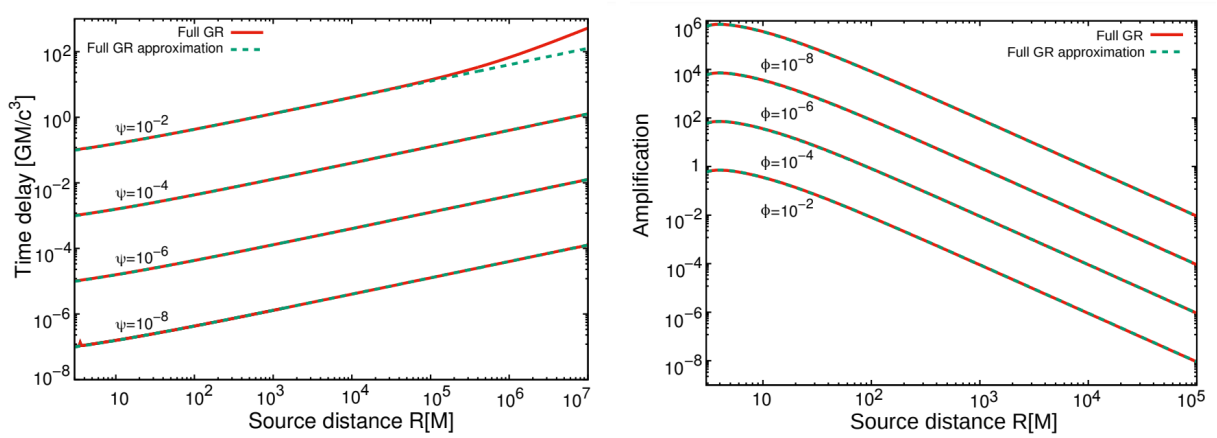

Figure 7.21: *Left:* Time delay between the first two images from the primary amplification peak for exact FGR (red) and the FGR approximation from Equation (7.4) (green) with respect to the distance of the source to the compact object. *Right:* Secondary amplification peak. The amplification for the secondary amplification peak with respect to the distance of the source to the lens for multiple angular separations from the caustic line ψ for the exact FGR and FGR approximation using Equation 7.5. Taken from my publication [170].

The secondary amplification peak is created for a source close to the caustic line in front of the lens and the contribution comes mainly from the first indirect and the second direct images (see the right panel of Figure 7.21). The amplification of the secondary peak can be approximated by

$$\mathcal{M}_{2a} = C_2(R, M)\frac{M^2}{\psi R^2} \tag{7.5}$$

where the correction factor is defined as

$$C_2(R, M) = 0.913\left(1 - \frac{12}{9.74 + R/M}\right). \tag{7.6}$$

The amplification of the secondary peak with respect to the distance of the source and lens for multiple separation angles is shown in the right panel of Figure 7.21 for the exact FGR and FGR approximation, using Equation (7.5). In the case of the secondary amplification

peak, the differential time delay between the images is independent of the source distance and can be approximated with a simple relation

$$\Delta t = 10.5M/\psi. \tag{7.7}$$

These simple analytical formulae can be used as an alternative approach to the exact FGR calculations of the amplification and time delay for the primary and secondary peak for a small sized source in the regime of extreme amplification. Moreover, the correction factors introduced in Equation (7.3) and Equation (7.6) can be also applied for calculation of the amplification in case of a finite-sized source with uniform brightness, see [170] for more detail.

Chapter 8

Conclusions

This dissertation thesis primarily explores the properties of ultra-high-energy cosmic rays (UHECRs), with a specific focus on investigation of the impact of cosmic-ray propagation in the universe. Two phenomenological research topics are presented, one addressing the modification of the dipole anisotropy in arrival directions of cosmic rays due to the Galactic magnetic field, and the second topic discussing features of a single-source scenario describing the shape of the energy spectrum of cosmic rays above $10^{19.5}$ eV as observed by the Pierre Auger Observatory. The final chapter of this thesis is devoted to the work performed for the preparation of the SWGO experiment focusing on Monte Carlo simulations of the responses of water Cherenkov detectors to gamma-ray showers. Additionally, the research concerning the amplification of photon intensity of a source located close to a compact object is presented.

The research topic presented in Chapter 5 is following up on the observation of a large-scale dipole anisotropy in arrival directions of cosmic rays above 8 EeV by the Pierre Auger Observatory proving the extragalactic origin of the highest-energy cosmic rays. This work was previously presented on international conferences [117, 118] and the final results were published in [84]. The focus of this research is the investigation of how the Galactic magnetic field (GMF) influences this large-scale anisotropy and to determine the potential direction of this anisotropy before cosmic rays enter the Milky Way. Two models of the GMF, namely the JF12Planck and three variations of the TF17 model of the GMF, were employed to propagate cosmic rays within the Galaxy. The dipole direction and amplitude on Earth after propagation in the GMF was reconstructed and compared with the properties of the dipole measured by the Pierre Auger Observatory at the 1σ and 2σ level. The extragalactic directions of the dipole compatible with the observation were identified for all the possible mass-composition mixes of p, He, N and Fe with step of 5%.

In case of the *pure-proton scenario*, the allowed directions of an extragalactic dipole are located in a close vicinity of the observed dipole, namely within $\sim 25^\circ$ and $\sim 35^\circ$ from the measured direction of the dipole on Earth at the 1σ level for the JF12Planck and TF17 model of the GMF, respectively. The extragalactic amplitude of the dipole has to be $\leq 10\%$ for both considered models of the GMF. For *pure-helium scenario*, the allowed directions of the extragalactic dipole at the 1σ level are within $\sim 35^\circ$ and $\sim 60^\circ$

for the JF12Planck and TF17, respectively. Increasing the mass of particles, the allowed directions of the extragalactic dipole are allowed further from the observed dipole direction on Earth. In case of *pure-nitrogen scenario*, the allowed directions of the extragalactic dipole are located in a small area located from $\sim 80^\circ$ to 105° from the measured dipole for the JF12Planck model of the GMF. Identified allowed directions for the TF17 model of the GMF are located in an extended band of latitudes between the longitudes 210° and 240°. No allowed directions of the extragalactic dipole were identified at the 1σ level for the JF12Planck model of the GMF in the case of the *pure-iron scenario*, while two areas of allowed directions were identified for the TF17 model; one in a close vicinity of the measured direction of the dipole on Earth and the second area close to the direction of the Galactic center.

Considering all possible mass-composition mixes of cosmic rays above 8 EeV, the allowed directions of the extragalactic dipole at the 1σ level are found in two separated areas for both models of the GMF (see Figure 5.11). The first group of solutions at the 1σ level for the JF12Planck model of the GMF is located within $\sim 45^\circ$ from the measured direction of the dipole on Earth and is dominated by low-mass mixes, while the second area corresponds to the nitrogen-dominated cosmic-ray flux and extends up to $\sim 105^\circ$ from the measured direction on Earth. In case of the TF17 model of the GMF, the first area of solutions is extending over a large range of latitudes and a small range in longitudes and is within $\sim 80^\circ$ from the measured dipole direction. The second group of allowed directions is the aforementioned area close to the Galactic center for pure-iron scenario. Note, that this result does not suggest a Galactic origin of this dipole anisotropy as the simulated flux is of an extragalactic origin. The allowed directions of the extragalactic dipole identified at the 2σ level include interesting astrophysical systems like the Centaurus A, which is the nearest radio galaxy to Earth. Furthermore, the 2MRS dipole is also located in the 2σ regions of allowed extragalactic directions of the dipole.

A single-source scenario at the highest energies is studied in Chapter 6. This topic is based on the discrepancies in the energy spectrum of cosmic rays at the highest energies measured by the Pierre Auger Observatory in the Southern hemisphere and by the Telescope Array in the Northern hemisphere. This work was presented on international conferences [131, 132]. This discrepancy might be caused by different sources that these two experiments are able to see. In this work, it is assumed that the flux of cosmic rays above $10^{19.5}$ eV observed by the Pierre Auger Observatory might be caused by a single (dominant) source. For various distances of the source from Earth, I explored the features of such a source using simulations in CRPropa 3, including the mass composition, spectral index and rigidity cutoff. The energy losses of cosmic rays with background photons during propagation are taken into account. The resulting spectrum on Earth is compared with the energy spectrum measured by the Pierre Auger Observatory. The features of such a single source that create an energy spectrum compatible with the measured one are identified. When including additional cuts on the mass composition on Earth, corresponding approximately to the measurements of the Pierre Auger Observatory, the set of possible features of a single source is largely reduced. In order to describe both the energy spectrum and the mass composition well, the single source should be within 20 Mpc from Earth with the

spectral index $\gamma \sim 3$. Moreover, the cutoff rigidity at the source is limited to the values $\log(R_{\rm cut}/V) \leq 19.2$ (see Figure 6.6).

Although it is possible to describe the shape of the energy spectrum and the mean mass composition on Earth by a single source with such features, it is also shown that this single source scenario would create clustering of events and create anisotropies that are not seen in the current data. Therefore, a more realistic scenario to explain the discrepancies in the energy spectra measured by the Pierre Auger Observatory and Telescope Array could be a strongly dominant (not single) source or multiple strong sources contributing to the energy spectrum at the highest energies. This scenario, together with more detailed modeling of the energy spectrum of such sources is an interesting topic for future research.

The topic presented in Section 7.2 deals with the detailed Monte Carlo simulations of responses of water Cherenkov detectors for the planned Southern Wide-field Gamma-ray Observatory (SWGO). This experiment is currently in the R&D phase and I joined the Analysis and simulation working group studying responses of various detector concepts to gamma-ray and cosmic-ray showers. Part of the work presented in this thesis is related to verification of the suitability of the simulation software, HAWCsim, used by the SWGO collaboration. This software is based on the framework developed for the HAWC experiment that consists of large-volume water Cherenkov detector stations. I compared the responses of a single detector unit to muons injected into the volume of the WCD in two different simulation softwares and verified the suitability of HAWCsim for the purposes of SWGO for simulations of small tanks. This work was presented as an internal note for the Collaboration [163]. The second part of the work for the SWGO presented in this thesis is dealing with simulations of the responses of *Mercedes* water Cherenkov detector [164] and its main properties, as was published in [164]. The single detector unit response was studied for photons with energies from 1 MeV to 10^5 MeV showing the station sensitivity to photons at a wide range of energies and appropriate scaling of the signal induced in the station with the energy of the incident particle, see Figure 7.16. It was also shown that the absolute signal induced in the *Mercedes* station for muons is stronger than the signal induced for electromagnetic particles, which is a crucial property of a water Cherenkov detector for any gamma/hadron separation analysis. My current follow-up work for the SWGO experiment includes simulations of the responses of the whole detector array at the PeV energies.

Additionally, Section 7.3 presents a topic of amplification of photon intensity of sources in binary systems with compact objects. In this research topic, I proposed approximate formulae for the amplification (Equations (7.2), (7.5)) and time delay (Equations (7.4),(7.7)) of the first two lensing images in the regime of extreme amplification of point-like and small-sized sources located in a close vicinity of the caustic line at a short distance from a Schwarzschild black hole gravitational lens. The new approximate formulae can describe the fully relativistic numerical calculations of the primary and secondary amplification peak in the extreme lensing regime with an accuracy level of few percent. The suggested formulae for the amplification contain correction factors, Equations (7.3), (7.6), that can be also used in the calculations of amplification in the case of finite-sized sources. These analytical approximations now serve as a valuable alternative to the computationally intensive fully

relativistic numerical calculations traditionally employed in such analyses. These formulae were published in [170].

The current understanding of the properties of ultra-high-energy cosmic rays should soon improve with the upgrade of the Pierre Auger Observatory, AugerPrime, and the extension of the Telescope Array. AugerPrime's enhancements will enable a more precise differentiation between individual primary particles, offering an improved characterization of the mass composition of UHECRs. This will allow the separation of the detected events by rigidity, allowing targeted searches for mass-dependent anisotropies that could provide valuable insights about the sources. New experiments are also planned to be build, such as the Global Cosmic Ray Observatory (GCOS) [173], aiming to greatly increase the detection area and consequently greatly increase the statistics at the highest energies which is crucial for unraveling the lasting mysteries surrounding UHECRs. In addition to the experimental upgrades, new and improved models of the GMF are being proposed, such as [174]. These models offer more accurate predictions regarding the deflections of the UHECRs and allow for a more reliable tracing of these particles back to their sources.

Bibliography

[1] K.-H. Kampert and A.A. Watson, *Extensive air showers and ultra high-energy cosmic rays: a historical review*, *European Physical Journal H* **37** (2012) 359 [1207.4827].

[2] Pierre Auger collaboration, *Observation of a large-scale anisotropy in the arrival directions of cosmic rays above 8 × 10^{18} eV*, *Science* **357** (2017) 1266–1270 [1709.07321].

[3] M. Bertolotti, *Celestial Messengers: Cosmic Rays: The Story of a Scientific Adventure*, Springer-Verlag Berlin Heidelberg (2013), 10.1007/978-3-642-28371-0.

[4] J.R. Hörandel, *Early Cosmic-Ray Work Published in German*, *AIP Conf. Proc.* **1516** (2013) 52 [1212.0706].

[5] D. Pacini, *La radiazione penetrante alla superficie ed in seno alle acque*, *Il Nuovo Cimento* **3** (1912) 93 [1002.1810].

[6] V.F. Hess, *Über Beobachtungen der durchdringenden Strahlung bei sieben Freiballonfahrten*, *Phys. Z.* **13** (1912) 1084.

[7] P. Auger, P. Ehrenfest, R. Maze, J. Daudin and R.A. Fréon, *Extensive Cosmic-Ray Showers*, *Reviews of Modern Physics* **11** (1939) 288.

[8] J. Linsley, *Evidence for a Primary Cosmic-Ray Particle with Energy* 10^{20} *eV*, *Physical Review Letters* **10** (1963) 146.

[9] Pierre Auger collaboration, *The Pierre Auger Cosmic Ray Observatory*, *Nuclear Instruments and Methods in Physics Research* **798** (2015) 172 [1502.01323].

[10] Telescope Array collaboration, *Surface detectors of the TAx4 experiment*, *Nuclear Instruments and Methods in Physics Research A* **1019** (2021) 165726 [2103.01086].

[11] W. Heitler, *The Quantum Theory of Radiation, Third edition*, Oxford university press (1954).

[12] J. Matthews, *A Heitler model of extensive air showers*, *Astroparticle Physics* **22** (2005) 387.

[13] P. Lipari, *Concepts of "age" and "universality" in cosmic ray showers*, *Physical Review D* **79** (2009) 063001 [0809.0190].

[14] M. Giller, A. Kacperczyk, J. Malinowski, W. Tkaczyk and G. Wieczorek, *Similarity of extensive air showers with respect to the shower age*, *Journal of Physics G Nuclear Physics* **31** (2005) 947.

[15] F. Nerling, J. Blümer, R. Engel and M. Risse, *Universality of electron distributions in high-energy air showers—Description of Cherenkov light production*, *Astroparticle Physics* **24** (2006) 421 [astro-ph/0506729].

[16] M. Stadelmaier, *On Air-Shower Universality and the Mass Composition of Ultra-High-Energy Cosmic Rays*, Ph.D. thesis, Karlsruher Institut für Technologie (KIT), 2022.

[17] T. Bergmann, R. Engel, D. Heck, N.N. Kalmykov, S. Ostapchenko, T. Pierog et al., *One-dimensional hybrid approach to extensive air shower simulation*, *Astroparticle Physics* **26** (2007) 420 [astro-ph/0606564].

[18] D. Heck, J. Knapp, J.N. Capdevielle, G. Schatz and T. Thouw, *CORSIKA: a Monte Carlo code to simulate extensive air showers.* (1998).

[19] S.J. Sciutto, *AIRES: A system for air shower simulations*, *arXiv e-prints* (1999) arXiv:astro ph/9911331 [astro-ph/9911331].

[20] K. Greisen, *Cosmic ray showers*, *Annual Review of Nuclear Science* **10** (1960) 63 [https://doi.org/10.1146/annurev.ns.10.120160.000431].

[21] A.M. Hillas, *Two Interesting Techniques for Monte-Carlo Simulation of Very High Energy Hadron Cascades*, in *International Cosmic Ray Conference*, vol. 8, p. 193, Jan., 1981.

[22] T. Pierog and K. Werner, *EPOS Model and Ultra High Energy Cosmic Rays*, *Nuclear Physics B Proceedings Supplements* **196** (2009) 102 [0905.1198].

[23] T. Pierog, I. Karpenko, J.M. Katzy, E. Yatsenko and K. Werner, *EPOS LHC : test of collective hadronization with LHC data*, *arXiv e-prints* (2013) arXiv:1306.0121 [1306.0121].

[24] S. Ostapchenko, *Monte Carlo treatment of hadronic interactions in enhanced Pomeron scheme: QGSJET-II model*, *Physical Review D* **83** (2011) 014018 [1010.1869].

[25] S. Ostapchenko, *LHC data on inelastic diffraction and uncertainties in the predictions for longitudinal extensive air shower development*, *Physical Review D* **89** (2014) 074009 [1402.5084].

[26] R.S. Fletcher, T.K. Gaisser, P. Lipari and T. Stanev, *SIBYLL: An event generator for simulation of high energy cosmic ray cascades*, *Physical Review D* **50** (1994) 5710.

[27] F. Riehn, R. Engel, A. Fedynitch, T.K. Gaisser and T. Stanev, *Hadronic interaction model SIBYLL 2.3d and extensive air showers*, *Physical Review D* **102** (2020) 063002 [1912.03300].

[28] A. Ferrari, P.R. Sala, A. Fasso and J. Ranft, *FLUKA: A multi-particle transport code (Program version 2005)* (10, 2005), 10.2172/877507.

[29] H. Fesefeldt, *Report PITHA-85/02*, Tech. Rep. RWTH Aachen (1985).

[30] S.A. Bass, M. Belkacem, M. Bleicher, M. Brandstetter, L. Bravina, C. Ernst et al., *Microscopic models for ultrarelativistic heavy ion collisions*, *Progress in Particle and Nuclear Physics* **41** (1998) 255 [nucl-th/9803035].

[31] J. Albrecht et al., *The Muon Puzzle in cosmic-ray induced air showers and its connection to the Large Hadron Collider*, *Astrophysics and Space Science* **367** (2022) 27 [2105.06148].

[32] Pierre Auger collaboration, *Direct measurement of the muonic content of extensive air showers between 2 $\times 10^{17}$ and 2 $\times 10^{18}$ eV at the Pierre Auger Observatory*, *European Physical Journal C* **80** (2020) 751.

[33] Pierre Auger collaboration, *Measurement of the Fluctuations in the Number of Muons in Extensive Air Showers with the Pierre Auger Observatory*, *Physical Review Letters* **126** (2021) 152002 [2102.07797].

[34] L. Cazon *for the EAS-MSU, IceCube, KASCADE Grande, NEVOD-DECOR, Pierre Auger, SUGAR, Telescope Array and Yakutsk EAS Array collaborations*, *Working Group Report on the Combined Analysis of Muon Density Measurements from Eight Air Shower Experiments*, in *Proceedings of 36th International Cosmic Ray Conference — PoS(ICRC2019)*, vol. 358, p. 214, 2019, DOI.

[35] V. Novotný, *Measurement of the energy spectrum of cosmic rays using Cherenkov-dominated data at the Pierre Auger Observatory*, Ph.D. thesis, Charles University, Faculty of Mathematics and Physics, Prague, Czech Republic, 2021.

[36] Pierre Auger collaboration, *Spectral calibration of the fluorescence telescopes of the Pierre Auger Observatory*, *Astroparticle Physics* **95** (2017) 44 [1709.01537].

[37] M. Unger, *Mass sensitive observables of the Pierre Auger Observatory*, in *European Physical Journal Web of Conferences*, vol. 53, p. 04009, June, 2013, DOI.

[38] A.A. Watson, *The Pierre Auger Observatory: why and how* (2006), 10.5170/CERN-2006-015.191.

[39] Pierre Auger collaboration, *The rapid atmospheric monitoring system of the Pierre Auger Observatory*, *Journal of Instrumentation* **7** (2012) 9001 [1208.1675].

[40] Pierre Auger collaboration, *Features of the Energy Spectrum of Cosmic Rays above 2.5×10^{18} eV Using the Pierre Auger Observatory*, *Physical Review Letters* **125** (2020) [2008.06488].

[41] X. Bertou, P.S. Allison, C. Bonifazi, P. Bauleo, C.M. Grunfeld, M. Aglietta et al., *Calibration of the surface array of the Pierre Auger Observatory*, *Nuclear Instruments and Methods in Physics Research A* **568** (2006) 839 [2102.01656].

[42] A. Castellina *for the Pierre Auger collaboration*, *AugerPrime: the Pierre Auger Observatory Upgrade*, in *European Physical Journal Web of Conferences*, vol. 210, p. 06002, Oct., 2019, DOI [1905.04472].

[43] Pierre Auger collaboration, *The Pierre Auger Observatory Upgrade - Preliminary Design Report*, *arXiv e-prints* (2016) arXiv:1604.03637 [1604.03637].

[44] Pierre Auger collaboration, *The fluorescence detector of the Pierre Auger Observatory*, *Nuclear Instruments and Methods in Physics Research A* **620** (2010) 227.

[45] M. Ave, M. Bohacova, B. Buonomo, N. Busca, L. Cazon, S.D. Chemerisov et al., *Measurement of the pressure dependence of air fluorescence emission induced by electrons*, *Astroparticle Physics* **28** (2007) 41 [astro-ph/0703132].

[46] M. Ave, M. Bohacova, E. Curry, P. Di Carlo, C. Di Giulio, P. Facal San Luis et al., *Precise measurement of the absolute fluorescence yield of the 337 nm band in atmospheric gases*, *Astroparticle Physics* **42** (2013) 90 [1210.6734].

[47] T.K. Gaisser and A.M. Hillas, *Reliability of the Method of Constant Intensity Cuts for Reconstructing the Average Development of Vertical Showers*, in *International Cosmic Ray Conference*, vol. 8, p. 353, Jan., 1977.

[48] Pierre Auger Collaboration collaboration, *Data-driven estimation of the invisible energy of cosmic ray showers with the Pierre Auger Observatory*, *Physical Review D* **100** (2019) 082003 [1901.08040].

[49] Pierre Auger collaboration, *Depth of maximum of air-shower profiles at the Pierre Auger Observatory. I. Measurements at energies above 10$^{17.8}$ eV*, *Physical Review D* **90** (2014) 122005 [1409.4809].

[50] Pierre Auger collaboration, *Reconstruction of inclined air showers detected with the Pierre Auger Observatory*, *Journal of Cosmology and Astroparticle Physics* **2014** (2014) 019 [1407.3214].

[51] D. Newton, J. Knapp and A.A. Watson, *The optimum distance at which to determine the size of a giant air shower*, *Astroparticle Physics* **26** (2007) 414 [astro-ph/0608118].

[52] Pierre Auger collaboration, *Measurement of the cosmic-ray energy spectrum above 2.5×10^{18} eV using the Pierre Auger Observatory*, *Physical Review D* **102** (2020) 062005 [2008.06486].

[53] K. Kamata and J. Nishimura, *The Lateral and the Angular Structure Functions of Electron Showers*, *Progress of Theoretical Physics Supplement* **6** (1958) 93.

[54] R. Alves Batista and A. Saveliev, *The Gamma-Ray Window to Intergalactic Magnetism*, *Universe* **7** (2021) 223 [2105.12020].

[55] R.A. Batista, D. Boncioli, A. di Matteo, A. van Vliet and D. Walz, *Effects of uncertainties in simulations of extragalactic UHECR propagation, using CRPropa and SimProp*, *Journal of Cosmology and Astroparticle Physics* **2015** (2015) 063.

[56] T.M. Kneiske, T. Bretz, K. Mannheim and D.H. Hartmann, *Implications of cosmological gamma-ray absorption. II. Modification of gamma-ray spectra*, *Astronomy and Astrophysics* **413** (2004) 807 [astro-ph/0309141].

[57] F.W. Stecker, M.A. Malkan and S.T. Scully, *Intergalactic Photon Spectra from the Far-IR to the UV Lyman Limit for $0 < z < 6$ and the Optical Depth of the Universe to High-Energy Gamma Rays*, *The Astrophysical Journal* **648** (2006) 774 [astro-ph/0510449].

[58] A. Franceschini, G. Rodighiero and M. Vaccari, *Extragalactic optical-infrared background radiation, its time evolution and the cosmic photon-photon opacity*, *Astronomy and Astrophysics* **487** (2008) 837 [0805.1841].

[59] J.D. Finke, S. Razzaque and C.D. Dermer, *Modeling the Extragalactic Background Light from Stars and Dust*, *The Astrophysical Journal* **712** (2010) 238 [0905.1115].

[60] A. Domínguez, J.R. Primack, D.J. Rosario, F. Prada, R.C. Gilmore, S.M. Faber et al., *Extragalactic background light inferred from AEGIS galaxy-SED-type fractions*, *Monthly Notices of the Royal Astronomical Society* **410** (2011) 2556 [1007.1459].

[61] R.C. Gilmore, R.S. Somerville, J.R. Primack and A. Domínguez, *Semi-analytic modelling of the extragalactic background light and consequences for extragalactic gamma-ray spectra*, *Monthly Notices of the Royal Astronomical Society* **422** (2012) 3189 [1104.0671].

[62] D. Kuempel, *Extragalactic Propagation of Ultra-High Energy Cosmic Rays*, *arXiv e-prints* (2014) arXiv:1409.3129 [1409.3129].

[63] R. Ruffini, G.V. Vereshchagin and S.S. Xue, *Cosmic absorption of ultra high energy particles*, *Astrophysics and Space Science* **361** (2016) 82 [1503.07749].

[64] K. Greisen, *End to the Cosmic-Ray Spectrum?*, *Physical Review Letters* **16** (1966) 748.

[65] G.T. Zatsepin and V.A. Kuzmin, *Upper Limit of the Spectrum of Cosmic Rays*, *Soviet Journal of Experimental and Theoretical Physics Letters* **4** (1966) 78.

[66] D. Allard, *Propagation of extragalactic ultra-high energy cosmic-ray nuclei : implications for the observed spectrum and composition*, *arXiv e-prints* (2009) arXiv:0906.3156 [0906.3156].

[67] R. Aloisio, *Acceleration and propagation of ultra-high energy cosmic rays*, *Progress of Theoretical and Experimental Physics* **2017** (2017) 12A102 [1707.08471].

[68] D. Ryu, D.R.G. Schleicher, R.A. Treumann, C.G. Tsagas and L.M. Widrow, *Magnetic Fields in the Large-Scale Structure of the Universe*, *Space Science Reviews* **166** (2012) 1 [1109.4055].

[69] S. Mollerach and E. Roulet, *Ultrahigh energy cosmic rays from a nearby extragalactic source in the diffusive regime*, *Physical Review D* **99** (2019) 103010 [1903.05722].

[70] S. Hackstein, F. Vazza, M. Brüggen, G. Sigl and A. Dundovic, *Propagation of ultrahigh energy cosmic rays in extragalactic magnetic fields: a view from cosmological simulations*, *Monthly Notices of the Royal Astronomical Society* **462** (2016) 3660 [1607.08872].

[71] L.M. Widrow, *Origin of galactic and extragalactic magnetic fields*, *Reviews of Modern Physics* **74** (2002) 775 [astro-ph/0207240].

[72] T.R. Jaffe, *Practical Modeling of Large-Scale Galactic Magnetic Fields: Status and Prospects*, *Galaxies* **7** (2019) 52 [1904.12689].

[73] J.L. Han, R.N. Manchester, W. van Straten and P. Demorest, *Pulsar Rotation Measures and Large-scale Magnetic Field Reversals in the Galactic Disk*, *The Astrophysical Journal Supplement* **234** (2018) 11 [1712.01997].

[74] R. Beck, *Magnetic fields in the Milky Way and other spiral galaxies*, *arXiv e-prints* (2003) 0310287 [astro-ph/0310287].

[75] R. Jansson and G.R. Farrar, *A new model of the Galactic magnetic field*, *The Astrophysical Journal* **757** (2012) 14 [1204.3662].

[76] M. Prouza and R. Šmída, *The Galactic magnetic field and propagation of ultra-high energy cosmic rays*, *Astronomy and Astrophysics* **410** (2003) 1 [astro-ph/0307165].

[77] M.S. Pshirkov, P.G. Tinyakov, P.P. Kronberg and K.J. Newton-McGee, *Deriving the global structure of the galactic magnetic field from faraday rotation measures of extragalactic sources*, *The Astrophysical Journal* **738** (2011) 192 [1103.0814].

[78] P. Terral and K. Ferrière, *Constraints from Faraday rotation on the magnetic field structure in the galactic halo*, *Astronomy and Astrophysics* **600** (2017) A29.

[79] T.R. Jaffe, K.M. Ferrière, A.J. Banday, A.W. Strong, E. Orlando, J.F. Macías-Pérez et al., *Comparing polarized synchrotron and thermal dust emission in the Galactic plane*, *Monthly Notices of the Royal Astronomical Society* **431** (2013) 683 [1302.0143].

[80] R. Jansson and G.R. Farrar, *The Galactic Magnetic Field*, *The Astrophysical Journal Letters* **761** (2012) L11 [1210.7820].

[81] C.L. Bennett, R.S. Hill, G. Hinshaw, M.R. Nolta, N. Odegard, L. Page et al., *First-Year Wilkinson Microwave Anisotropy Probe (WMAP) Observations: Foreground Emission*, *The Astrophysical Journal Supplement* **148** (2003) 97 [astro-ph/0302208].

[82] Planck collaboration, *Planck intermediate results. XLII. Large-scale Galactic magnetic fields*, *Astronomy and Astrophysics* **596** (2016) A103 [1601.00546].

[83] R. Alves Batista, A. Dundovic, M. Erdmann et al., *CRPropa 3 - A public astrophysical simulation framework for propagating extraterrestrial ultra-high energy particles*, *Journal of Cosmology and Astroparticle Physics* **2016** (2016) 038 [1603.07142].

[84] A. Bakalová, J. Vícha and P. Trávníček, *Modification of the dipole in arrival directions of ultra-high-energy cosmic rays due to the Galactic magnetic field*, *Journal of Cosmology and Astroparticle Physics* **2023** (2023) 016 [2303.08766].

[85] F. Vazza, G. Brunetti, M. Brüggen and A. Bonafede, *Resolved magnetic dynamo action in the simulated intracluster medium*, *Monthly Notices of the Royal Astronomical Society* **474** (2018) 1672 [1711.02673].

[86] K. Jedamzik and A. Saveliev, *Stringent Limit on Primordial Magnetic Fields from the Cosmic Microwave Background Radiation*, *Physical Review Letters* **123** (2019) 021301 [1804.06115].

[87] E. Waxman and J. Miralda-Escudé, *Images of bursting sources of high-energy cosmic rays: Effects of magnetic fields*, *The Astrophysical Journal* **472** (1996) L89–L92 [astro-ph/9607059].

[88] G.R. Farrar, R. Jansson, I.J. Feain and B.M. Gaensler, *Galactic magnetic deflections and Centaurus A as a UHECR source*, *Journal of Cosmology and Astroparticle Physics* **2013** (2013) 023 [1211.7086].

[89] J. Blümer, R. Engel and J.R. Hörandel, *Cosmic rays from the knee to the highest energies*, *Progress in Particle and Nuclear Physics* **63** (2009) 293 [0904.0725].

[90] G. V. Kulikov and G. B. Khristiansen, *On the Size Spectrum of Extensive Air Showers*, *Journal of Experimental and Theoretical Physics* **35** (1958) 635.

[91] KASCADE-Grande collaboration, *KASCADE-Grande measurements of energy spectra for elemental groups of cosmic rays*, *arXiv e-prints* (2013) arXiv:1306.6283 [1306.6283].

[92] B. Peters, *Primary cosmic radiation and extensive air showers*, *Il Nuovo Cimento* **22** (1961) 800.

[93] A. Coleman, J. Eser, E. Mayotte, F. Sarazin, F.G. Schröder, D. Soldin et al., *Ultra high energy cosmic rays The intersection of the Cosmic and Energy Frontiers*, *Astroparticle Physics* **149** (2023) 102819 [2205.05845].

[94] A.A. Penzias and R.W. Wilson, *A Measurement of Excess Antenna Temperature at 4080 Mc/s.*, *The Astrophysical Journal* **142** (1965) 419.

[95] Y. Tsunesada *for the Pierre Auger and the Telescope Array collaborations* , *Joint analysis of the energy spectrum of ultra-high-energy cosmic rays as measured at the Pierre Auger Observatory and the Telescope Array*, in *Proceedings of 37th International Cosmic Ray Conference — PoS(ICRC2021)*, vol. 395, p. 337, 2021, DOI.

[96] O. Deligny *for the Pierre Auger and the Telescope Array collaborations*, *The energy spectrum of ultra-high energy cosmic rays measured at the Pierre Auger Observatory and at the Telescope Array*, in *Proceedings of 36th International Cosmic Ray Conference — PoS(ICRC2019)*, vol. 358, p. 234, 2019, DOI.

[97] J. Glombitza *for the Pierre Auger collaboration*, *Mass Composition from 3 EeV to 100 EeV using the Depth of the Maximum of Air-Shower Profiles Estimated with Deep Learning using Surface Detector Data of the Pierre Auger Observatory*, in *Proceedings of 38th International Cosmic Ray Conference — PoS(ICRC2023)*, vol. 444, p. 278, 2023, DOI.

[98] Pierre Auger collaboration, *Radio measurements of the depth of air-shower maximum at the Pierre Auger Observatory*, *Physical Review D* **109** (2024) 022002 [2310.19966].

[99] Pierre Auger collaboration, *Demonstrating Agreement between Radio and Fluorescence Measurements of the Depth of Maximum of Extensive Air Showers at the Pierre Auger Observatory*, *Physical Review Letters* **132** (2024) 021001 [2310.19963].

[100] A. Yushkov *for the Pierre Auger collaboration*, *Mass Composition of Cosmic Rays with Energies above $10^{17.2}$ eV from the Hybrid Data of the Pierre Auger Observatory*, in *Proceedings of 36th International Cosmic Ray Conference — PoS(ICRC2019)*, vol. 358, p. 482, 2019, DOI.

[101] Pierre Auger collaboration, *Evidence for a mixed mass composition at the 'ankle' in the cosmic-ray spectrum*, *Physics Letters B* **762** (2016) 288 [1609.08567].

[102] R.A. Gideon and R.A. Hollister, *A Rank Correlation Coefficient Resistant to Outliers*, *Journal of the American Statistical Association* **82** (1987) 656.

[103] S. Blaess, J.A. Bellido and B.R. Dawson, *Extracting a less model dependent cosmic ray composition from $X_{\max}$ distributions*, *arXiv e-prints* (2018) arXiv:1803.02520 [1803.02520].

[104] Pierre Auger collaboration, *Testing Hadronic-Model Predictions of Depth of Maximum of Air-Shower Profiles and Ground-Particle Signals using Hybrid Data of the Pierre Auger Observatory*, *arXiv e-prints* (2024) arXiv:2401.10740 [2401.10740].

[105] J. Glombitza *for the Pierre Auger collaboration*, *Event-by-event reconstruction of the shower maximum $X_{\max}$ with the Surface Detector of the Pierre Auger Observatory using deep learning*, in *Proceedings of 37th International Cosmic Ray Conference — PoS(ICRC2021)*, vol. 395, p. 359, 2021, DOI.

[106] Pierre Auger collaboration, *Inferences on mass composition and tests of hadronic interactions from 0.3 to 100 EeV using the water-Cherenkov detectors of the Pierre Auger Observatory*, *Physical Review D* **96** (2017) 122003 [1710.07249].

[107] Pierre Auger collaboration, *Deep-learning based reconstruction of the shower maximum X_{max} using the water-Cherenkov detectors of the Pierre Auger Observatory*, *Journal of Instrumentation* **16** (2021) P07019 [2101.02946].

[108] Pierre Auger collaboration, *Large-scale cosmic-ray anisotropies above 4 EeV measured by the Pierre Auger Observatory*, *Astrophysical Jornal* **868** (2018) 4 [1808.03579].

[109] Pierre Auger collaboration, *Cosmic-Ray Anisotropies in Right Ascension Measured by the Pierre Auger Observatory*, *The Astrophysical Journal* **891** (2020) 142 [2002.06172].

[110] Pierre Auger collaboration, *An Indication of Anisotropy in Arrival Directions of Ultra-high-energy Cosmic Rays through Comparison to the Flux Pattern of Extragalactic Gamma-Ray Sources*, *The Astrophysical Journal Letters* **853** (2018) L29 [1801.06160].

[111] Pierre Auger collaboration, *Searches for Anisotropies in the Arrival Directions of the Highest Energy Cosmic Rays Detected by the Pierre Auger Observatory*, *The Astrophysical Journal* **804** (2015) 15 [1411.6111].

[112] Pierre Auger collaboration, *Arrival Directions of Cosmic Rays above 32 EeV from Phase One of the Pierre Auger Observatory*, *The Astrophysical Journal* **935** (2022) 170 [2206.13492].

[113] T. Fujii *for the Telescope Array collaboration*, *Telescope Array anisotropy summary*, in *Proceedings of 37th International Cosmic Ray Conference — PoS(ICRC2021)*, vol. 395, p. 392, 2021, DOI.

[114] R.M. de Almeida *for the Pierre Auger and the Telescope Array collaborations*, *Large-scale and multipolar anisotropies of cosmic rays detected at the Pierre Auger Observatory with energies above 4 EeV*, in *Proceedings of the 37th International Cosmic Ray Conference — PoS(ICRC2021)*, vol. 395, p. 335, 2021, DOI.

[115] T. Fujii, *Rapporteur Talk: CRI*, in *Proceedings of 38th International Cosmic Ray Conference — PoS(ICRC2023)*, vol. 444, p. 031, 2024, DOI.

[116] J. Liouville, *Note sur la théorie de la variation des constantes arbitraires.*, *Journal de Mathématiques Pures et Appliquées* (1838) 342.

[117] A. Bakalová, P. Trávníček and J. Vícha, *Influence of Galactic magnetic field on large scale anisotropies of ultra-high energy cosmic rays*, in *Proceedings of 36th International Cosmic Ray Conference — PoS(ICRC2019)*, vol. 358, p. 183, 2019, DOI.

[118] A. Bakalová, P. Trávníček and J. Vícha, *Constraints on the origin of the UHECR dipole anisotropy outside the Galaxy*, in *40th International Conference on High Energy Physics*, p. 618, Apr., 2021, DOI.

[119] A. Kääpä, K.-H. Kampert and J. Becker Tjus, *Flux predictions in the transition region incorporating the effects from propagation of cosmic rays in the Galactic magnetic field*, in *European Physical Journal Web of Conferences*, vol. 283, p. 03006, Oct., 2023, DOI.

[120] C. Ding, N. Globus and G.R. Farrar, *The Imprint of Large Scale Structure on the Ultra-High-Energy Cosmic Ray Sky*, *Astrophysical Journal Letters* **913** (2021) L13 [2101.04564].

[121] M. Guenduez, J. Becker Tjus, K. Ferrière and R.-J. Dettmar, *A novel analytical model of the magnetic field configuration in the Galactic Center*, *Astronomy and Astrophysics* **644** (2020) A71 [1906.05211].

[122] R. Alves Batista, J. Becker Tjus, J. Dörner et al., *CRPropa 3.2 - an advanced framework for high-energy particle propagation in extragalactic and galactic spaces*, *Journal of Cosmology and Astroparticle Physics* **2022** (2022) 035 [2208.00107].

[123] J. Aublin and E. Parizot, *Generalised 3D-reconstruction method of a dipole anisotropy in cosmic-ray distributions*, *Astronomy and Astrophysics* **441** (2005) 407–415 [astro-ph/0504575].

[124] B. Eichmann and T. Winchen, *Galactic magnetic field bias on inferences from UHECR data*, *Journal of Cosmology and Astroparticle Physics* **2020** (2020) 047 [2001.01530].

[125] P. Erdoğdu, J.P. Huchra, O. Lahav et al., *The dipole anisotropy of the 2 Micron All-Sky Redshift Survey*, *Monthly Notices of the Royal Astronomical Society* **368** (2006) 1515 [astro-ph/0507166].

[126] D. Ivanov *for the Telescope Array collaboration*, *Energy Spectrum Measured by the Telescope Array*, in *Proceedings of 36th International Cosmic Ray Conference — PoS(ICRC2019)*, vol. 358, p. 298, 2019, DOI.

[127] J. Vícha *for the Pierre Auger collaboration*, *Adjustments to model predictions of depth of shower maximum and signals at ground level using hybrid events of the Pierre Auger Observatory*, in *Proceedings of the 37th International Cosmic Ray Conference — PoS(ICRC2021)*, vol. 395, Mar., 2021, DOI.

[128] H. Kawai, S. Yoshida, H. Yoshii, K. Tanaka, F. Cohen, M. Fukushima et al., *Telescope Array Experiment*, *Nuclear Physics B Proceedings Supplements* **175** (2008) 221.

[129] A. Bakalová, *Connection between Energy Spectrum, Mass Composition and Distribution of Sources of Extragalactic Cosmic Rays*, Master's thesis, Faculty of Nuclear Sciences and Physical Engineering, Czech Technical University, Prague, Czech Republic, 2018.

[130] C. J. Todero Peixoto *for the Pierre Auger collaboration*, *Estimating the Depth of Shower Maximum using the Surface Detectors of the Pierre Auger Observatory*, in *Proceedings of 36th International Cosmic Ray Conference — PoS(ICRC2019)*, vol. 358, p. 440, 2019, DOI.

[131] A. Bakalová, J. Vícha and P. Trávníček, *Features of a single source describing the very end of the energy spectrum of cosmic rays*, in *Proceedings of 37th International Cosmic Ray Conference — PoS(ICRC2021)*, vol. 395, p. 363, 2021, DOI.

[132] A. Bakalová, J. Vícha and P. Trávníček, *Single source scenario describing the very end of the cosmic ray energy spectrum*, in *European Physical Journal Web of Conferences*, vol. 283, p. 02016, Oct., 2023, DOI.

[133] A.J. Koning, S. Hilaire and M.C. Duijvestijn, *TALYS: Comprehensive Nuclear Reaction Modeling*, in *International Conference on Nuclear Data for Science and Technology*, R.C. Haight, M.B. Chadwick, T. Kawano and P. Talou, eds., vol. 769 of *American Institute of Physics Conference Series*, pp. 1154–1159, May, 2005, DOI.

[134] Pierre Auger collaboration, *Combined fit of spectrum and composition data as measured by the Pierre Auger Observatory*, *Journal of Cosmology and Astroparticle Physics* **2017** (2017) 038 [1612.07155].

[135] E. Guido *for the Pierre Auger collaboration*, *Combined fit of the energy spectrum and mass composition across the ankle with the data measured at the Pierre Auger Observatory*, in *Proceedings of 37th International Cosmic Ray Conference — PoS(ICRC2021)*, vol. 395, p. 311, 2021, DOI.

[136] E. Mayotte *for the Pierre Auger collaboration*, *Measurement of the mass composition of ultra-high-energy cosmic rays at the Pierre Auger Observatory*, in *Proceedings of 38th International Cosmic Ray Conference — PoS(ICRC2023)*, vol. 444, p. 365, 2023, DOI.

[137] HESS collaboration, *The status of the HESS project*, *New Astronomy Review* **48** (2004) 331 [astro-ph/0403052].

[138] MAGIC collaboration, *Status and First Results of the Magic Telescope*, *Astrophysics and Space Science* **297** (2005) 245 [astro-ph/0407475].

[139] T.C. Weekes et al., *VERITAS: the Very Energetic Radiation Imaging Telescope Array System*, *Astroparticle Physics* **17** (2002) 221 [astro-ph/0108478].

[140] CTA collaboration, *Introducing the CTA concept*, *Astroparticle Physics* **43** (2013) 3.

[141] CTA collaboration, *Monte Carlo studies for the optimisation of the Cherenkov Telescope Array layout*, *Astroparticle Physics* **111** (2019) 35 [1904.01426].

[142] H. Schoorlemmer *for the SWGO collaboration*, *A next-generation ground-based wide field-of-view gamma-ray observatory in the southern hemisphere*, in *Proceedings of 36th International Cosmic Ray Conference — PoS(ICRC2019)*, vol. 358, p. 785, 2019, DOI.

[143] A.U. Abeysekara et al., *Observation of the Crab Nebula with the HAWC Gamma-Ray Observatory*, *Astrophysical Jornal* **843** (2017) 39 [1701.01778].

[144] Z. Cao et al., *The Large High Altitude Air Shower Observatory (LHAASO) Science Book (2021 Edition)*, *arXiv e-prints* (2019) arXiv:1905.02773 [1905.02773].

[145] R. Alfaro et al., *Gamma/hadron separation with the HAWC observatory*, *Nuclear Instruments and Methods in Physics Research A* **1039** (2022) 166984 [2205.12188].

[146] A. Albert, R. Alfaro, H. Ashkar, C. Alvarez, J. Álvarez, J.C. Arteaga-Velázquez et al., *Science Case for a Wide Field-of-View Very-High-Energy Gamma-Ray Observatory in the Southern Hemisphere*, *arXiv e-prints* (2019) arXiv:1902.08429 [1902.08429].

[147] Huentemeyer P. and others, *The Southern Wide-Field Gamma-Ray Observatory (SWGO): A Next-Generation Ground-Based Survey Instrument for VHE Gamma-Ray Astronomy*, *arXiv e-prints* (2019) arXiv:1907.07737 [1907.07737].

[148] J. Hinton *for the SWGO collaboration*, *The Southern Wide-field Gamma-ray Observatory: Status and Prospects*, in *Proceedings of 37th International Cosmic Ray Conference — PoS(ICRC2021)*, vol. 395, p. 023, 2021, DOI.

[149] S. Kunwar *for the SWGO collaboration*, *Double-layered Water Cherenkov Detector for SWGO*, in *Proceedings of 37th International Cosmic Ray Conference — PoS(ICRC2021)*, vol. 395, p. 902, 2021, DOI.

[150] P. Assis et al., *From many tens of GeV to many tens of PeV: a layout for SWGO*, *HAP-2021-003* (2021) Internal note.

[151] R. Conceição, P.J. Costa, L. Gibilisco, M. Pimenta and B. Tomé, *P^{α}_{tail}: a high resolution gamma/hadron and composition discriminant variable for Water-Cherenkov Detector cosmic-ray observatories*, *arXiv e-prints* (2023) arXiv:2309.17217 [2309.17217].

[152] M. Amenomori, Y.W. Bao, X.J. Bi, D. Chen, T.L. Chen, W.Y. Chen et al., *First Detection of sub-PeV Diffuse Gamma Rays from the Galactic Disk: Evidence for Ubiquitous Galactic Cosmic Rays beyond PeV Energies*, *Physical Review Letters* **126** (2021) 141101 [2104.05181].

[153] LHAASO collaboration, *Ultrahigh-energy photons up to 1.4 petaelectronvolts from 12 γ-ray Galactic sources*, *Nature* **594** (2021) 33.

[154] MAGIC collaboration, *Detection of very high energy gamma-ray emission from the gravitationally-lensed blazar QSO B0218+357 with the MAGIC telescopes*, *Astronomy and Astrophysics* **595** (2016) A98 [1609.01095].

[155] MAGIC collaboration, *Teraelectronvolt emission from the γ-ray burst GRB 190114C*, *Nature* **575** (2019) 455 [2006.07249].

[156] H.E.S.S. collaboration, *Revealing x-ray and gamma ray temporal and spectral similarities in the GRB 190829A afterglow*, *Science* **372** (2021) 1081 [2106.02510].

[157] G. Principe, L. Di Venere, M. Negro, N. Di Lalla, N. Omodei, R. Di Tria et al., *Hunting for gamma-ray emission from fast radio bursts*, *Astronomy and Astrophysics* **675** (2023) A99 [2305.09428].

[158] T. Cohen, K. Murase, N.L. Rodd, B.R. Safdi and Y. Soreq, *γ-ray constraints on decaying dark matter and implications for icecube*, *Physical Review Letters* **119** (2017) 021102.

[159] A. Berlin, D. Hooper and G. Krnjaic, *PeV-scale dark matter as a thermal relic of a decoupled sector*, *Physics Letters B* **760** (2016) 106.

[160] A. Taylor *for the SWGO collaboration*, *Composition Sensitivity for the Cosmic Ray Anisotropy with SWGO*, in *Proceedings of 37th International Cosmic Ray Conference — PoS(ICRC2021)*, vol. 395, p. 198, 2021, DOI.

[161] R. G. Lang *for the SWGO collaboration*, *Estimating the potential of SWGO to measure the composition-dependent behaviour of the CR anisotropy*, in *Proceedings of 38th International Cosmic Ray Conference — PoS(ICRC2023)*, vol. 444, p. 486, 2023, DOI.

[162] P. Assis, U. Barres de Almeida, A. Blanco, R. Conceição, B. D'Ettorre Piazzoli, A. De Angelis et al., *Design and expected performance of a novel hybrid detector for very-high-energy gamma-ray astrophysics*, *Astroparticle Physics* **99** (2018) 34 [1607.03051].

[163] A. Bakalová, R. Conceição, B. Tomé and J. Vícha, *Tests of the SWGO simulation framework*, *HAP-21-004* (2021) Internal note.

[164] P. Assis, A. Bakalová, U. Barres de Almeida, P. Brogueira, R. Conceição, A. De Angelis et al., *The Mercedes water Cherenkov detector*, *European Physical Journal C* **82** (2022) 899 [2203.08782].

[165] R. Conceição, P. Assis, F. Assunção, A. Bakalová, U. Barres de Almeida, C. Roque Bom et al., *Gamma/hadron discrimination using a small-WCD with four PMTs*, in *Proceedings of 37th International Cosmic Ray Conference — PoS(ICRC2021)*, vol. 395, p. 707, 2021, DOI.

[166] S. Agostinelli et al., *Geant4—a simulation toolkit*, *Nuclear Instruments and Methods in Physics Research* **506** (2003) 250.

[167] J. Allison et al., *Geant4 developments and applications*, *Transactions on Nuclear Science* **53** (2006) 270.

[168] J. Allison et al., *Recent developments in Geant4*, *Nuclear Instruments and Methods in Physics Research* **835** (2016) 186.

[169] R. Conceição, B.S. González, A. Guillén, M. Pimenta and B. Tomé, *Muon identification in a compact single-layered water Cherenkov detector and gamma/hadron discrimination using machine learning techniques*, *European Physical Journal C* **81** (2021) 542 [2101.10109].

[170] P. Bakala, A. Bakalová, R. La Placa, M. Falanga and L. Stella, *Extreme amplification regimes of the Schwarzschild gravitational lens*, *Astronomy and Astrophysics* **673** (2023) A164.

[171] V. Perlick, *Gravitational Lensing from a Spacetime Perspective*, *arXiv e-prints* (2010) arXiv:1010.3416 [1010.3416].

[172] C. Darwin, *The Gravity Field of a Particle*, *Proceedings of the Royal Society of London Series A* **249** (1959) 180.

[173] J.R. Hörandel *for the GCOS collaboration*, *GCOS - The Global Cosmic Ray Observatory*, in *Proceedings of 37th International Cosmic Ray Conference — PoS(ICRC2021)*, vol. 395, p. 027, 2021, DOI.

[174] M. Unger and G. Farrar, *The Coherent Magnetic Field of the Milky Way*, *arXiv e-prints* (2023) arXiv:2311.12120 [2311.12120].

Appendix A

Calculation of dipole amplitude for mixed mass composition

In Chapter 5, the direction and amplitude of the dipole for mixed composition is obtained from features of the dipoles of single elements. While the direction of the dipole can be obtained from Equation (5.4), the amplitude needs to be calculated in different manner. In case of dipole distribution, the flux in direction $\mathbf{u}$ can be written as

$$\phi(\mathbf{u}) = \frac{\phi_0}{4\pi}(1 + \alpha \mathbf{D} \cdot \mathbf{u}), \tag{A.1}$$

composed of an isotropic component $\phi_0/4\pi$ and a dipole component with amplitude α, relative to the isotropic flux, and the direction of the dipole given by a unit vector $\mathbf{D}$.

Lets assume a mixed composition dipole flux that is created as a sum of two single element dipole fluxes. We can write, that the flux in the direction of the dipole $\mathbf{D}$ is equal to

$$\phi(\mathbf{D}) = \frac{\phi_0}{4\pi}(1 + \alpha \mathbf{D} \cdot \mathbf{D}) = \frac{\phi_0}{4\pi}(1 + \alpha). \tag{A.2}$$

This can be written as the direction of the dipole is a unit vector. For the simplification of the following procedure, let us use a rescaled flux defined as $\phi_0' = \phi_0/4\pi$.

At the same time, the flux can be also written as a sum of the two single element dipole fluxes in direction $\mathbf{D}$ as

$$\phi(\mathbf{D}) = \phi_A(\mathbf{D}) + \phi_B(\mathbf{D}), \tag{A.3}$$

where $\phi_A(\mathbf{D})$ and $\phi_A(\mathbf{D})$ are the fluxes of the single elements fluxes in the direction of the combined dipole $\mathbf{D}$. We can expand this using the Equation (A.3) and Equation (A.2) for the single particle fluxes as

$$\phi_0'(1 + \alpha) = \phi_1(1 + \alpha_1 \mathbf{D}_1 \cdot \mathbf{D}) + \phi_2(1 + \alpha_2 \mathbf{D}_2 \cdot \mathbf{D}), \tag{A.4}$$

where α_1 and α_2 are the single element amplitudes and $\mathbf{D}_1$ and $\mathbf{D}_2$ are the directions of the single element dipoles. Then

$$\phi_0'(1+\alpha) = \phi_1 + \phi_1\alpha_1 \cos\delta_1 + \phi_2 + \phi_2\alpha_2 \cos\delta_2, \tag{A.5}$$

where δ_1 and δ_2 is the angle between the direction of the single element dipole and the direction of the mixed composition dipole. This can be further rewritten in the form of

$$\phi_0'(1+\alpha) = (\phi_1+\phi_2)(1 + \frac{\phi_1}{\phi_1+\phi_2}\alpha_1 \cos\delta_1 + \frac{\phi_2}{\phi_1+\phi_2}\alpha_2 \cos\delta_2). \tag{A.6}$$

The total flux is given as a sum of the two single element fluxes, therefore

$$\phi_0' = \phi_1 + \phi_2 \tag{A.7}$$

and the fraction of the single element in the composition mix can be expressed as

$$f_1 = \frac{\phi_1}{\phi_1+\phi_2} = \frac{\phi_1}{\phi_0'} \tag{A.8}$$

and

$$f_2 = \frac{\phi_2}{\phi_1+\phi_2} = \frac{\phi_2}{\phi_0'} \tag{A.9}$$

for the two single elements. Equation (A.6) can be now written as

$$\phi_0'(1+\alpha) = \phi_0'(1 + f_1\alpha_1 \cos\delta_1 + f_2\alpha_2 \cos\delta_2). \tag{A.10}$$

Comparing the left and right side of Equation A.10, we can see that the amplitude of the mixed composition dipole is equal to

$$\alpha = f_1\alpha_1 \cos\delta_1 + f_2\alpha_2 \cos\delta_2. \tag{A.11}$$

Similarly, the amplitude of a dipole composed by n single-element dipole fluxes is then calculated as

$$\alpha = \sum_{i=1}^{n} f_i\alpha_i \cos\delta_i. \tag{A.12}$$

Appendix B

Selected publications

B.1 Journal articles

- A. Bakalová, P. Trávníček, J. Vícha, *Modification of the dipole in the arrival directions of ultra-high energy cosmic rays*, Journal of Cosmology and Astroparticle Physics **2023** (2023) 016

- P. Assis, A. Bakalová, U. Barres de Almeida et al., *The Mercedes water Cherenkov detector*, The European Physical Journal C **82** (2022) 899.

- P. Bakala, A. Bakalová, R. La Placa et al., *Extreme amplification regimes of the Schwarzschild gravitational lens*, Astronomy&Astrophysics **673** (2023) A164.

B.2 Conference proceedings

- A. Bakalová, P. Trávníček, J. Vícha, *Single source scenario describing the very end of the cosmic ray energy spectrum*, European Physical Journal Web of Conferences (UHECR2022) **283** (2023) 02016.

- A. Bakalová, P. Trávníček, J. Vícha, *Features of a single source describing the very end of the energy spectrum of cosmic rays*, Proceedings of 37th International Cosmic Ray Conference — PoS(ICRC2021), **395** (2022) 363.

- A. Bakalová, P. Trávníček, J. Vícha, *Constraints on the origin of the UHECR dipole anisotropy outside the Galaxy*, Proceedings of 40th International Conference on High Energy physics — PoS(ICHEP2020), **390** (2021) 618.

- A. Bakalová, P. Trávníček, J. Vícha, *Influence of the Galactic magnetic field on the large-scale anisotropies of ultra-high energy cosmic rays*,Proceedings of 36th International Cosmic Ray Conference — PoS(ICRC2019) **358** (2019) 183.